Développement et optimization des performances d'un accéléromètre convective triaxial CMOS micro-usiné

Sonia Abdellatif

▶ **To cite this version:**

Sonia Abdellatif. Développement et optimization des performances d'un accéléromètre convective triaxial CMOS micro-usiné. Electronique. Université de Montpellier; École nationale d'ingénieurs de Sfax (Tunisie), 2022. Français. NNT : 2022UMONS035 . tel-04056932

HAL Id: tel-04056932

https://theses.hal.science/tel-04056932

Submitted on 3 Apr 2023

HAL is a multi-disciplinary open access archive for the deposit and dissemination of scientific research documents, whether they are published or not. The documents may come from teaching and research institutions in France or abroad, or from public or private research centers.

L'archive ouverte pluridisciplinaire **HAL**, est destinée au dépôt et à la diffusion de documents scientifiques de niveau recherche, publiés ou non, émanant des établissements d'enseignement et de recherche français ou étrangers, des laboratoires publics ou privés.

THÈSE POUR OBTENIR LE GRADE DE DOCTEUR DE L'UNIVERSITÉ DE MONTPELLIER

En Systèmes Automatiques et Microélectroniques (SyAM)

École doctorale : Information, Structures, Systèmes (I2S)

Unité de recherche : Laboratoire d'Informatique, de Robotique et de Microélectronique de Montpellier – UMR 5506

En partenariat international avec ENIS, TUNISIE

Development and performance optimization of a 3-axis CMOS micromachined convective accelerometer

Présenté par Sonia ABDELLATIF
Le 8 Novembre 2022

Sous la direction de M. Pascal NOUET
et M. Brahim MEZGHANI

Devant le jury composé de

Hassene MNIF , Professeur, ENET'COM, Sfax	[Président]
Hélène TAP, Professeur des Universités, INP-ENSEEIHT, Toulouse	[Rapporteur]
Hatem SMAALI, Maître de conférences, EPT, Tunis	[Rapporteur]
Laurent LATORRE, Professeur des Universités, UM, Montpellier	[Examinateur]
Ahmed FAKHFAKH, Professeur, ENET'COM, Sfax	[Examinateur]
Aboubacar CHAEHOI, Technical Leader, TDK-Micronas	[Invité]
Pascal NOUET, Professeur des Universités, UM, Montpellier	[Directeur]
Brahim MEZGHANI, Professeur, ENIS, Sfax	[Directeur]
Frédérick MAILLY, Maître de conférences, UM, Montpellier	[Co-encadrant]

UNIVERSITÉ DE MONTPELLIER

Acknowledgment

I would like to sincerely thank the members of the jury, who gave me the great honor to review this work. I would also like to express my gratitude to my thesis director, Mr. Brahim MEZGHANI, for guiding and advising me throughout my PhD journey. His availability and his continuous support throughout the realization of this work made great difference. I address my sincere gratitude to my thesis director, Mr. Pascal NOUET, for his enthusiasm on the project, and for his thoughtful comments and recommendations. Great appreciation for my co-supervisor, Mr. Frederick MAILLY, for providing guidance and valuable feedback throughout this project. May they find in this work the expression of my sincere gratitude and my deep respect.

I thank my very dear parents, who have always been there for me. You gave me a magnificent model of hard work and perseverance. I owe you an education of which I am proud of. I thank my sisters Rim, Ines, Sihem, Oumaima for their valuable encouragement and support. I would like to express my gratitude to all my friends and colleagues, especially my colleague Awatef KHLIFI for her company and support throughout the journey.

I address my eternal love and gratitude for my husband, Wacef MEJRI, for believing in me and for being there from the beginning till the end. This project wouldn't be the same without his moral support and encouragement.

Table of Contents

List of Figures

List of tables

General Introduction

Since its first appearance in the mid-1980s, the field of Micro Electro-Mechanical Systems (MEMS) have gained a lot of research interest and was extensively studied. Commercial exploitation of MEMS was generalized for mass market with several drivers such as ink jet heads for printers and accelerometers for airbag triggers. Initially, MEMS technology was strongly inspired by manufacturing processes and materials from the silicon integrated circuits (ICs) industry. Therefore, it was not surprising that researchers have been trying to co-integrate MEMS devices with CMOS circuitry by combining post-CMOS micromachining techniques with a standard CMOS process. In fact, a lot of interest has been paid to the manufacturing process for the aim of monolithic integration of MEMS structures with control and processing circuits. Batch fabrication of a sensor and its conditioning electronics paves the way for sensors with reduced manufacturing costs in large volume production and reduced footprints.

Among the firstly CMOS integrated sensors are accelerometers (Sherman, Tsang et al. 1992), devices that measure the acceleration along one or multiple axis. Generally, acceleration measurement is performed by means of a proof-mass that moves under the effect of an acceleration. This detection principle is mostly employed in capacitive (Tez, Aykutlu et al. 2015), piezoelectric (Beeby, Ross et al. 2000), and piezoresistive (Partridge, Reynolds et al. 2000) accelerometers. However, a movable part inside the device induces reliability problems especially under large accelerations. Indeed, shock resistance of a proof-mass-based accelerometer is relatively low. To overcome the above-mentioned problem, a convection-based micromachined accelerometer has been proposed in the middle of the nineties (Leung, Jones et al. 1997). In this accelerometer, the proof-mass displacement is replaced by displacement in a hot bubble of gas or fluid that deforms under the effect of acceleration due to free convection. The absence of proof mass renders convective accelerometers more robust to high shocks (Garraud, Combette et al. 2011). Combining this robustness with general advantages of MEMS or CMOS-MEMS, micromachined accelerometers have been used in consumer applications such as low-cost navigation systems (Dong, Zwahlen et al. 2011), in military field including missile guidance (Hopkins, Borenstein et al. 1998), and in robotics and system automation (Yazdi, Ayazi et al. 1998).

Although CMOS MEMS is a good option for the fabrication of single and dual-axis convective accelerometers since they both use planar structures; the measurement of out-of-plane accelerations is more challenging. This is generally due to the fact that the third axis

measurement requires generally tridimensional structures and complicated fabrication processes (Hua, Jiang et al. 2008, Bahari and Leung 2011, Silva, Dias et al. 2012, Phan, Dinh et al. 2018). As for monolithic micromachined planar structures, only few solutions were reported. In 2013, MEMSIC^{TM} (Hua, Jiang et al. 2008, Zhao and Cai 2008) proposed a three-axis convective accelerometer, but the out-of-plane sensing principle was not scientifically discussed. A similar accelerometer was reported in (Nguyen, Mailly et al. 2015), where vertical sensing is based on the measurement of in-plane common-mode temperature in a non-symmetrical structure along z-axis.

Despite the simplicity of convective accelerometers, numerous design parameters have complex effects on sensor sensitivity due to their impact on physical phenomena such as heat conduction and convection. These parameters include heating (Milanovi, Bowen et al. 1998) and ambient temperature (Sherman, Tsang et al. 1992), geometrical parameters (Luo, Yang et al. 2001, Rekik, Azaïs et al. 2010, Park, Park et al. 2011, Rekik, Mezghani et al. 2011), fluid properties and pressure inside the micromachined cavity (Mailly, Martinez et al. 2003, Ishak, Sidek et al. 2011) and detectors' configuration and positioning inside the micromachined cavity (Milanovi, Bowen et al. 1998, Mailly, Martinez et al. 2003, Mezghani, Brahim et al. 2011).

The aim of this thesis is to improve out-of-plane sensitivity of a three-axis convective accelerometer manufactured in a CMOS standard process followed by a post-process, the Front Side Bulk Micromachining (FSBM). This post-process is based on substrate etching of a CMOS die through its front side and it have been used by LIRMM for many years for its affordable price. The thesis aims also to develop a simplified model that predicts the sensor's sensitivity in all three axis according to design parameters. This will help reduce the time and effort done on complicated and time-consuming numerical simulations.

The first chapter presents a general overview of MEMS technology and MEMS sensors. A particular attention is paid to MEMS accelerometers. Finally, advantages and limitations of CMOS and MEMS co-integration is discussed.

In the second chapter, two solutions for performance improvement of a triaxial monolithic convective accelerometer are investigated. The first solution is mechanical, where a new design of the heater bridges is proposed in order to allow turning the heater into a seismic mass and thus improving out-of-plane sensitivity. The second solution is based on proposing a new heater design for improving the sensitivity in all-three axis while reducing the power consumption.

We first identify the non-feasibility of the first solution in FSBM technology and we then study extensively the second solution.

The third chapter illustrates the optimization steps of the heater geometry and detector bridges to reduce heat losses, to maximize sensitivity, and to reduce power consumption. This chapter also details the design of a silicon prototypes as a proof of concept.

The last chapter details the derivation steps of both in-plane (i.e., x and y-axis) and out-of-plane (i.e., z-axis) overall sensitivity expressions of the developed accelerometer using finite element analysis to model the effects of key parameters on the sensitivity of the sensor, which include the height and width of bottom cavity and top cover in addition to the heater temperature. The obtained compact analytical models of the sensitivities are then validated for a large range of feasible design parameters through CMOS technology.

REFERENCES

Bahari J., and Albert ML., « Micromachined three-axis thermal accelerometer with a single composite heater », *Journal of Micromechanics and Microengineering,* vol. 21, n° 7, 2011, p. 075025.

Beeby SP., Ross JN., White NM., « Design and fabrication of a micromachined silicon accelerometer with thick-film printed PZT sensors », *Journal of Micromechanics and Microengineering*, vol. 10, n° 3, 2000, p. 322-328.

Dau VT., Dinh TX., Dang LB., Tran CD., Bui TT., Hoa PT., « Tri-axis convective accelerometer with closed-loop heat source », *J Sensors and Actuators A: Physical*, vol. 275, 2018, p. 51-59.

Dong Y., Zwahlen P., Nguyen AM., Frosio R., Rudolf F., « Ultra-high precision MEMS accelerometer », *16th International Solid-State Sensors, Actuators and Microsystems Conference*, 2011, p. 695-698.

Hopkins R., Borenstein J., Antkowiak B., Ward P., Elliott R., « The silicon oscillating accelerometer: a MEMS inertial instrument for strategic missile guidance », *The missile sciences conference*, 1998.

Hua Y., Jiang L., Cai Y., Leung A., Zhao Y., « Single chip tri-axis accelerometer », U.S. Patent 20070101813, Sep. 16, 2005.

Ishak MZ, Sidek O, Aziz JA, Mohd SKK, and Miskam MA, « Effect of working fluid, acceleration and heater power on temperature profile inside a thermal convective accelerometer », *IEEE Regional Symposium on Micro and Nano Electronics,* 2011, p. 334-338.

Leung AM., Jones J., Czyzewska E., Chen J., Pascal M., « Micromachined accelerometer with no proof mass », *International Electron Devices Meeting. IEDM Technical Digest*, 1997, p. 899-902.

Luo XB., Yang YJ., Zheng F., Li ZX., Guo ZY., « An optimized micromachined convective accelerometer with no proof mass », *Journal of Micromechanics and Microengineering*, vol. 11, n° 5, 2001, p. 504-508.

Mailly F., Martinez A., Giani A., Pascal-Delannoy F., Boyer A., « Effect of gas pressure on the sensitivity of a micromachined thermal accelerometer », *J Sensors and Actuators A: Physical*, vol. 109, n° 1-2, 2003, p. 88-94.

Mezghani B., Brahim A, Tounsi F., Masmoudi M., Rekik AA., Nouet P., « From 2D to 3D FEM simulations of a CMOS MEMS convective accelerometer », *IEEE International Conference on Microelectronics ICM Proceeding,* 2011.

Milanovi V., Bowen E., Tea N., Suehle J., Payne B., Zaghloul M., Gaitan M., « Convection-based accelerometer and tilt sensor implemented in standard CMOS », *International Mechanical Engineering Congress and Exposition*, 1998.

Nguyen HB., Mailly F., Latorre L., Nouet P., « A new monolithic 3-axis thermal convective accelerometer: principle, design, fabrication and characterization », *Microsystem Technologies*, vol. 21, n° 9, 2015, p. 1867-1877.

Park U., Park BK., Moon IK., Kim D., Kim J., « Development of a dual-axis micromachined convective accelerometer with an effective heater geometry », *J Microelectronic Engineering*, vol. 88, n° 3, 2011, p. 276-281.

Partridge A., Reynolds JK., Chui BW., Chow EM., Fitzgerald AM., Zhang L., Maluf NI., Kenny TW., « A high-performance planar piezoresistive accelerometer », *Journal of microelectromechanical systems,* vol. 9, n° 1, 2000, p. 58-66.

Rekik AA., Azaïs F., Dumas N., Masmoudi M., Mailly F., Nouet P., « A study of package effects on the behavior of MEMS convective accelerometers », *Symposium on Design Test Integration and Packaging of MEMS/MOEMS (DTIP),* 2010, p. 6-9.

Rekik AA., Mezghani B., Azaïs F., Dumas N., Masmoudi M., Mailly F., Nouet P., « Investigation on the effect of geometrical dimensions on the conductive behaviour of a MEMS convective accelerometer », *Symposium on Design, Test, Integration & Packaging of MEMS/MOEMS (DTIP),* 2011, p. 14-17.

Rocha LA., Silva CS., Cerqueira MF., Ribeiro JF., Gonçalves LM., Pontes AJ., Viana JC., « A microinjected 3-axis thermal accelerometer », *Procedia Engineering*, vol. 25, 2011, p. 607-610.

Sherman SJ., Tsang WK., Core TA., Quinn DE., « A low cost monolithic accelerometer », *Symposium on VLSI Circuits Digest of technical papers,* 1992, p. 34-35.

Tez S., Aykutlu U., Torunbalci MM., Akin T., « A bulk-micromachined three-axis capacitive MEMS accelerometer on a single die », *Journal of Microelectromechanical Systems*, vol. 24, n° 5, 2015, p. 1264-1274.

Yazdi N., Ayazi F., Najafi K., « Micromachined inertial sensors », *Proceedings of the IEEE*, vol. 86, n° 8, 1998, p. 1640-1659.

Zhao Y., Cai Y., « Z-axis thermal accelerometer », U.S. patent, 7392703, Jul. 01, 2008.

Chapter 1: MEMS accelerometers and specific limitations

Introduction

This chapter presents an overview of the MEMS field, including different fabrication technologies and materials in addition to the broad field of applications provided by MEMS. Attention will be focalized on MEMS accelerometers and different characterization parameters will be discussed in general and for each type of transduction type in order to be able to position the thermal accelerometer (also called as convective accelerometer) among other types of accelerometers. As its names indicates, the targeted accelerometer in this thesis which is thermal accelerometer, depends on heat exchanges. Therefore, thermal phenomena involved in the functioning of a thermal accelerometer will be discussed. Once thermal transfer theories will be reminded, we will concentrate on explaining the working principle of convective accelerometer. A state of art of convective accelerometers in literature in their uniaxial, dual axial and triaxial forms will be presented with the achieved performances especially in terms of sensitivity and power consumption. We will enter in more details with CMOS compatible convective accelerometers for the advantages presented by this integration. The limitation imposed by CMOS integration will be also discussed especially in terms of out-of-plane sensitivity, which is generally limited by the planar nature of the CMOS technology.

1.1 MEMS technology

1.1.1 MEMS Fabrication technologies

Microelectromechanical systems, abbreviated as MEMS, are small integrated systems that combine on the same chip both mechanical and electronical units. MEMS cannot be identified by a unique fabrication process or limited in few materials, it is an approach that takes advantage of microelectronics, multiple on-chip components and miniaturization. It can be defined as an innovative technology for the design of mechanical devices. MEMS gather sensors, actuators, miniaturized mechanical structures and microelectronics.

MEMS fabrication is a new technology. It is rapidly evolving to meet different requirements like involving a variety of materials, increasing the manufacturing yield and reducing the cost. Although MEMS technologies involve many processes that are common to the microelectronics industry, it incorporates specific process steps to provide the third dimension to mechanical parts. Major technological operations involved in a MEMS fabrication are additive process, subtractive process and patterning, each containing various techniques. As the diversity of

MEMS fabrication processes and their details are endless, we will present the most commonly used processes divided into two categories, monolithic approach and hybrid approach.

1.1.1.1 Monolithic fabrication approach

This approach of MEMS fabrication is based on integrating the mechanical part of the MEMS device with its conditioning electronics monolithically. From the perspective of the fabrication process, micromachining steps can be integrated in the fabrication process prior to, intermediate with, or following the fabrication of the electronic circuitry. The most common micromachining technique used with monolithic fabrication is bulk micromachining, which refers to removing (etching) pieces selectively from a bulk material, generally silicon. Two etching processes are possible: dry and wet etching

1.1.1.1.1 Dry etching

Dry etching is done by exposing the wafer to ions bombardment (called plasma) to remove the exposed portion of the material. Dry etching process is typically anisotropic, where high levels of directionality can be achieved. DRIE (Deep Reactive Ion Etching) is a dry etching technique that etches the exposed material surface in the perpendicular direction way much faster than the parallel direction to the surface. This technique is therefore used when nearly vertical sidewalls with high quality surface are required. In plasma etching, a reactive gas is excited by an RF (radiofrequency) electric field ranging generally from 10 to 15 MHz. The plasma, contained in a vacuum chamber, excites the chemical gas to provide to ions needed for wafer etching. Example of structures etched using DRIE process is presented in Figure 1.1.

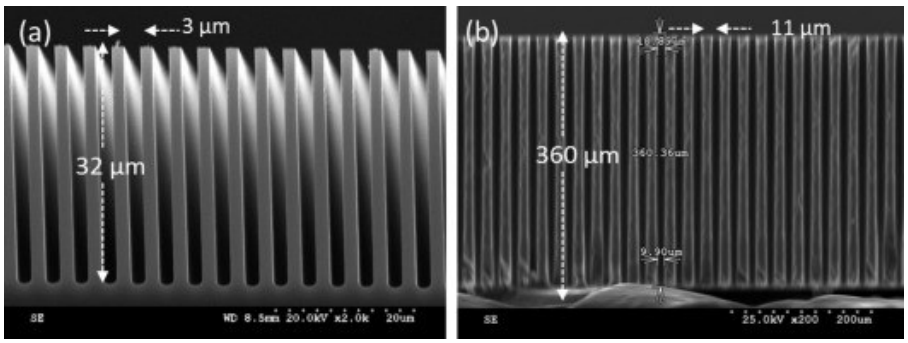

Figure 1.1. *A cross-sectional SEM image of trenches etched by Bosch-DRIE dry etching, (a) trench width 3 µm, etching depth is 32 µm (left) and (b) through-wafer etching, width 11 µm, depth 360 µm (Tilli, Paulasto-Kröckel et al. 2020).*

To control the etching depth, the exposure time of the material to the etchant should be calculated considering the etching rate, which is the amount of material removed per a unit of time.

Other more recent methods for material removal exists, such as laser ablation, micro-milling, ultrasonic machining and electro-discharge machining. These techniques are usually not oriented for batch fabrication, thus traditional etching processes are still the most used.

1.1.1.1.2 Wet etching

Wet etching consists in submerging a silicon wafer in an etching solution after applying a protective mask on the bulk material surfaces where etching should be avoided. Therefore, only the portions uncovered by protective material are removed. Wet etching is often isotropic, which means that the etching rate does not depend on the substrate orientation. However, anisotropic etchants also exist. In this case, the etching rate can be quite high along certain directions and negligible for others. Commonly used anisotropic silicon etching solutions are KOH (Potassium Hydroxide), EDP (Ethylenediamine Pyrocatechol) and TMAH (Tetramethylammonium hydroxide). Etching directions are defined with respect to crystalline orientation of monocrystalline silicon and the most common cavity shapes obtained with anisotropic etching techniques is an inverted pyramid. Each sidewall of the cavity makes a 54.7° angle with the wafer plane. Anisotropic etching is also commonly used to release suspended structures over etched cavities.

Wet micromachining process can be done either from the top-side of the wafer (i.e, Front-side Bulk Micromachining) or from the bottom (i.e. Back-Side Bulk Micromachining).

Front-Side Bulk Micromachining (FSBM)

FSBM is known for its compatibility with CMOS technology. This technique allows the monolithic integration of the mechanical part of MEMS sensor with its conditioning electronics on the same die. Using FSBM results in simpler and larger micro-machined structures compared to those obtained by surface micromachining. FSBM structures are then more shock resistant and particle contamination robust.

Back-Side Bulk Micromachining (BSBM)

BSBM post-processing can simplify significantly device fabrication. However, it can induce some limitations such as misalignments. Another issue is that the etching process may affect both sides of the wafer, so protecting the frontside from the etchant is needed.

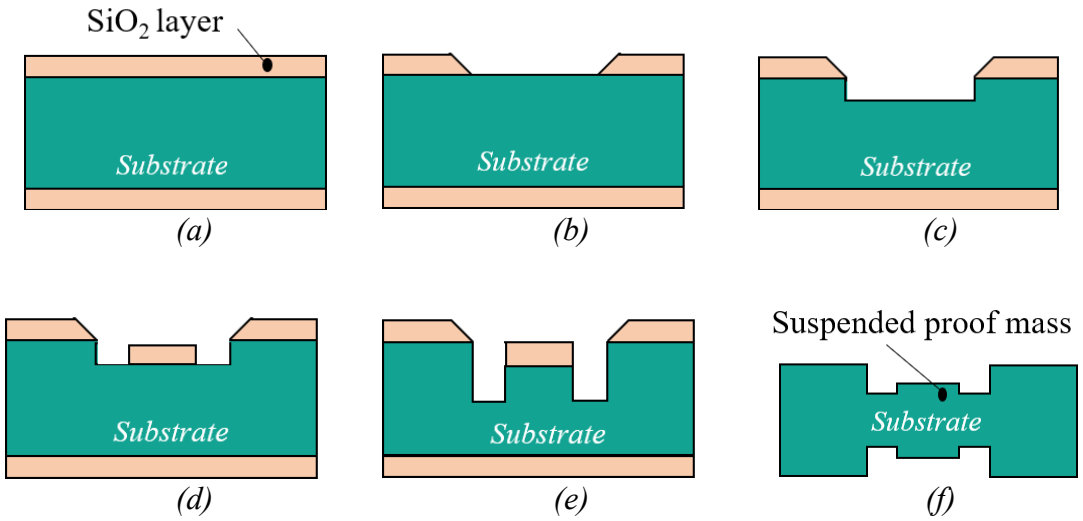

Figure 1.2. *Typical steps in Bulk micromachining process including (a) sacrificial layer deposition and (b)patterning (c) substrate etching (d) deposition of an additional protection layer of SiO2 (e) substrate etching (f) backside processing.*

Common steps of bulk micromachining, illustrated in Figure 1.2, are as follow:

a) Deposition of a silicon dioxide (SiO_2) thin layer with a typical thickness of 1-2µm using either Physical (PVD) or Chemical Vapor Deposition (CVD) or spin coating.

b) Patterning this sacrificial layer using photoresist resin deposition followed by an optical lithography and a selective etching.

c) Etching the substrate

d) Deposition and patterning of a new SiO_2 sacrificial layer on a selected area for protection

e) Substrate etching in order to create deeper cavities.

f) Repeating all the previous steps mentioned on the substrate backside to release the suspended structure (optional step).

1.1.1.2 Hybrid fabrication approach

Hybrid fabrication approach is used whenever the fabrication processes of mechanical and electronic parts of the MEMS are not compatible, therefore, both components are fabricated on two different substrates and then connected together.

When fabricating MEMS using hybrid solution, which involves generally complex mechanical parts of the system, surface micromachining is often used. This technique helps

creating mechanical structures by deposition and then etching of structural layers at the surface of a substrate.

To create a cantilever beam, the process described in Figure 1.3 starts generally by surface polishing. This technique aims to smooth the surface in order to prevent photolithography limitations and etching residues. Then, a sacrificial layer is deposed and later removed selectively to define the desired shape using photolithography and etching processes (Figure 1.3 (a)). An upper structural thin layer is then deposited above (Figure 1.3 (b)). Several techniques can be used for thin layers deposition, such as PVD, CVD, spin coating and electrodeposition. The thin layer is then patterned using photolithography and etching processes in order to define the desired structure. Finally, the cantilever beam is released by removing the sacrificial layer using a selective etching (Figure 1.3(c)). This set of procedures can be repeated as required depending on the complexity of the structure to be manufactured.

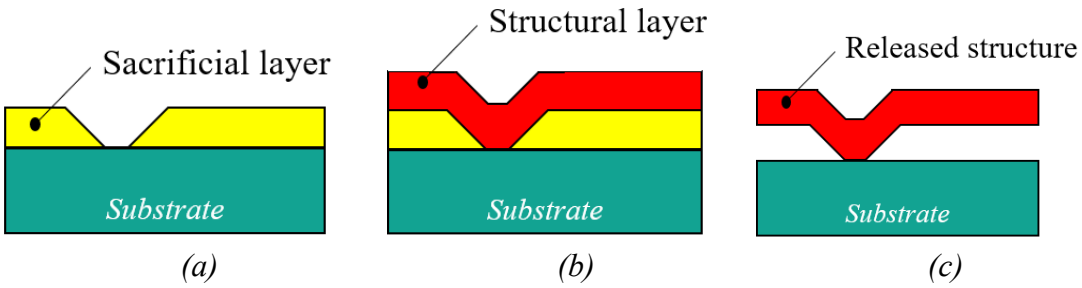

Figure 1.3. *Typical steps in surface micromachining process including (a) sacrificial layer deposition and patterning (b) deposition and patterning of the structural layer, (c) suspended structure release.*

1.1.2 Applications of MEMS

MEMS devices are found in numerous applications. Figure 1.4 shows worldwide MEMS market forecast per application worldwide from 2015 to 2021. It is clear that the MEMS market revenues have grown to reach a total amount of almost 20 billion U.S. dollars in 2021. The foremost revenues are coming from consumer applications, which have almost doubled in 7 years.

Smartphones are maybe the most well-known embedded systems that combine several MEMS, including MEMS motion sensors such as accelerometers and gyroscopes, pressure sensors, magnetometers and MEMS microphones. In personal computers, accelerometers are used to detect free-fall of hard disk head. Other day-to-day devices that include MEMS,

especially inertial sensors, are digital camera stabilizers, personal media players, toys, pedometers, game controllers and much more.

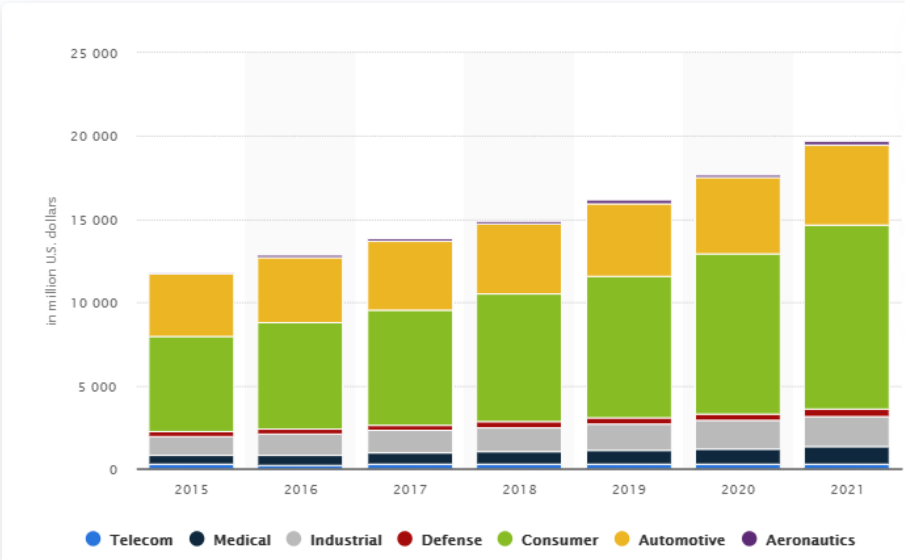

Figure 1.4 *MEMS worldwide market forecast per application worldwide from 2015 to 2021(in million U.S. dollars) (Department April 2016).*

In automotive industry, MEMS applications seems to be endless: safety improvement, driving and riding comfort as well as environmental monitoring. Some of the most known application in automotive concerns pressure sensors, since pressure measurement is a necessity in vehicles systems for air conditioning, fuel and air intake measurement and tires smart monitoring. Accelerometers are extensively used for airbags activation in collisions and vehicle stability control. Gyroscopes are also used in anti-roll-over systems in order to detect possible conditions for rollover and control the vehicle in dangerous conditions. Inclinometers may be also present to limit vehicle's sliding.

MEMS are also present in inkjet printers that use thermal bubble printheads or piezoelectric printheads in order to deposit ink drops on paper. Thermal bubble printheads use water vaporization in the ink in order to produce a pressure able to push a drop of ink on the paper. Piezoelectric printheads, however, use piezoelectric effect to force an ink drop to deposit on the paper.

In biomedical field, MEMS are often called Bio-MEMS. These devices are deployed in medical and health application. The progress of this field is slow compared to other fields due to the complexity of this kind of systems and to the need of long-term testing (Gilleo 2005). MEMS technology allows small size devices that can be injected in a human's body or can

implement Lab-on-Chip devices to reduce time and material required for analysis, selectively detect unhealthy cells or monitor human blood and release medication in case of need. Intelligent MEMS gave a new approach to microsurgery since they can allow minimally invasive surgery of human body.

A variety of Radio Frequency (RF) devices, such as capacitors, resonators and variable inductors, are manufactured with MEMS technology. The most known application of MEMS in RF field maybe RF MEMS switch. Despite some reliability issues, MEMS switches tend to replace traditional switches for their better electromagnetic and electromechanical performance and low power requirement (Zheng, Papapolymerou et al. 2004, Li, Yin et al. 2010, Goel and Gupta 2020).

Finally, MEMS technology may be helpful for high-end applications due to size, weight and cost reduction, in addition to low power requirements. Thus, MEMS technology is promising for fire control systems, missile guidance, aircraft and missile autopilot, RF seekers and multiple other applications. Currently, efforts are made at the United States Army Aviation and Missile Command (AMCOM) to develop MEMS-based inertial components such as high-rate range gyroscopes, wide dynamic range accelerometers and miniaturized three-axis inertial measurement unit (Hudson, McMillen et al. 1999).

1.2 MEMS Accelerometers

An accelerometer is a device used to measure the variation of velocity over time in m/s^2 in the International System of Units (SI). Acceleration is frequently expressed as a number of ‘g’, which is the earth gravitational acceleration ($1g= 9{,}81\ m/s^2$).

In this thesis, the sensitivity of an accelerometer, which is the ratio between sensor’s output and input signal, will be expressed in V/g whenever the accelerometer and its conditioning chain are considered. However, when the bare accelerometer is considered, sensitivity will be given in K/g for a thermal accelerometer.

1.2.1 Specifications of MEMS accelerometers

1.2.1.1 Sensitivity

Sensitivity is one of the most important characteristics of a sensor. It gives the amount of change in the output signal when input entity changes. Therefore, it is defined as the ratio between the accelerometer’s output signal (generally a voltage) and the measured acceleration.

The sensitivity of an accelerometer is then expressed in V/g. When a conditioning circuit, that includes an amplification stage, is used, it is important to distinguish the sensitivity before and after amplification.

1.2.1.2 Linearity

A linear sensor is a sensor whose output signal is proportional to the input, which is the case of most MEMS accelerometers. However, linearity range of an accelerometer is always limited. Applying high accelerations that exceed linearity range makes the sensor irresponsive and leads to an output saturation.

1.2.1.3 Offset

When no acceleration is applied, the output of an accelerometer should be equal to zero. However practically, an error exists and is called offset or bias.

1.2.1.4 Noise

Noise in accelerometers is a source of error that generally limits the minimum measurable signal (see Resolution below). The sensor itself can be a source of noise, in addition to the conditioning electronics, mechanical damping (if it exists) and every electrical resistance. Brownian noise, which comes from dynamic forces of molecules that moves small particles is very significant in a micromachined system due to its reduced size.

1.2.1.5 Bandwidth

The bandwidth BW, generally measured in hertz, is the frequency range in which an accelerometer can operate.

1.2.1.6 Resolution

Resolution of an accelerometer is the smallest variation of acceleration that can be measured. It depends directly from the noise floor and the considered bandwidth. Assuming an output white noise v_{noise} given in g/$\sqrt{Hz}$, the resolution of the sensor is $v_{noise}\sqrt{BW}$ and is given in g.

1.2.1.7 Shock resistance

The shock resistance of an accelerometer is its ability to survive high amplitude accelerations without permanent damages or degradations of the above properties.

1.2.2 Types of MEMS accelerometers

1.2.2.1 MEMS piezoresistive accelerometer

Piezoresistivity is a well-known physical phenomenon in which the application of a mechanical stress generates a proportional resistivity variation (Smith 1954). Therefore, a piezoresistive accelerometer is a sensor that detects acceleration via the resistivity variation caused by a mechanical deformation.

Figure 1.5 illustrates the working principle of a piezoresistive accelerometer. A suspended proof mass is attached to the bulk substrate through a beam in which a piezoresistive material is integrated at the anchor point where maximum stress is located. By applying an external acceleration on the system, the proof mass moves and induces the beam deflection. This deflection generates a mechanical stress, which provokes a resistivity variation of the piezoresistive resistance layered on top of the attachment beam. By implementing a Wheatstone bridge, this resistance variation can be therefore converted to a voltage.

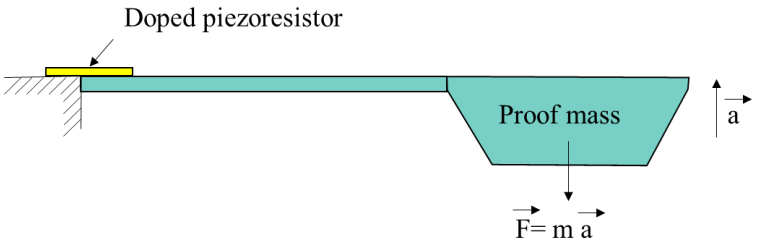

Figure 1.5. *Working principle of a piezoresistive accelerometer.*

Piezoelectric accelerometer can withstand accelerations up to 10000g (Ning, Loke et al. 1995, Huang, Li et al. 2005, Dong, Li et al. 2008, Zou, Wang et al. 2017), which makes them useful for high-g applications. Several multi-axis implementations of piezoresistive accelerometers have been reported (Chen, Bao et al. 1997, Dong, Li et al. 2008). A new approach that uses MEMS-NEMS technologies for 3D piezoresistive accelerometers fabrication was also proposed (Robert, Nguyen et al. 2009). Using diffused single-crystal silicon resistors or poly-silicon resistors as strain gauge allows CMOS integration of piezoresistive accelerometers since both materials are available in standard CMOS technologies (Latorre and Nouet 1999, Kal, Das et al. 2006). Complete structures of piezoresistive accelerometers with their readout circuitry on a standard CMOS chip were reported by (Warneke, Hoffman et al. 1995, Schröpfer, Elflein et al. 1998). A SEM image of a

monolithically integrated triaxial piezoresistive accelerometer with a shock resistance up to 1000g is presented in Figure 1.6.

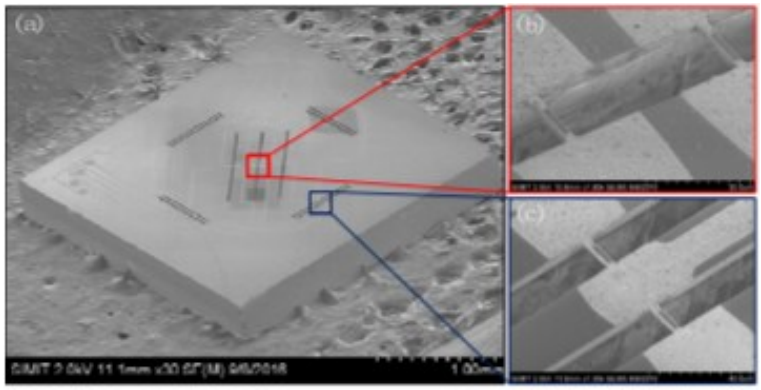

Figure 1.6. *(a) SEM image of the piezoresistive accelerometer. (b) Magnified central beams of the Z-axis sensor. (c) Magnified axial-beams of the X-axis sensor (Zou, Chen et al. 2017).*

Piezoresistive accelerometers are temperature dependent (Kim and Wise 1983) and they can be easily affected by self-heating (Doll, Corbin et al. 2011) since the resistivity of the piezoresistive materials presents a temperature coefficient. Decreasing piezoresistive accelerometer sensitivity and offset dependency on temperature have been the subject of multiple research efforts (Partridge, Reynolds et al. 2000). Low sensitivity is also an issue in piezoresistive accelerometers. In order to increase it, the design of the gauge, in addition to its value and implementing location can be optimized (Lim, Du et al. 1999, Kuells, Nau et al. 2012). The use of resistances in piezoresistive accelerometers requires additional current biasing, which increases the overall power consumption of the sensor compared to a capacitive one with the same performance.

1.2.2.2 MEMS piezoelectric accelerometer

The working principle of a piezoelectric accelerometer is presented in Figure 1.7; it is very similar to the piezoresistive one, where the piezoresistive material however is replaced by a piezoelectric layer generating an electric charge proportional to strain and thus to acceleration. Then, this charge can be converted using an appropriate readout circuitry, such as a charge amplifier.

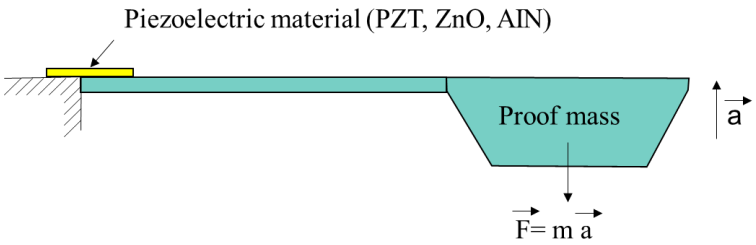

Figure 1.7. *Working principle of a piezoelectric accelerometer.*

Piezoelectric layer is generally made of lead-zirconate-titanate (PZT) (Wang, Wolf et al. 2003, Hewa-Kasakarage, Kim et al. 2013), zinc-oxide (ZnO) (DeVoe and Pisano 1997, Devoe and Pisano 2001) or aluminum nitride (A1N) (Wang, Ginsburg et al. 2006). For microfabrication technologies, both surface and bulk micromachining can be used as presented in Figure 1.8(a) and (b) respectively. Since it is necessary to deposit the piezoelectric material, fabrication using a standard CMOS process requires additional technological steps.

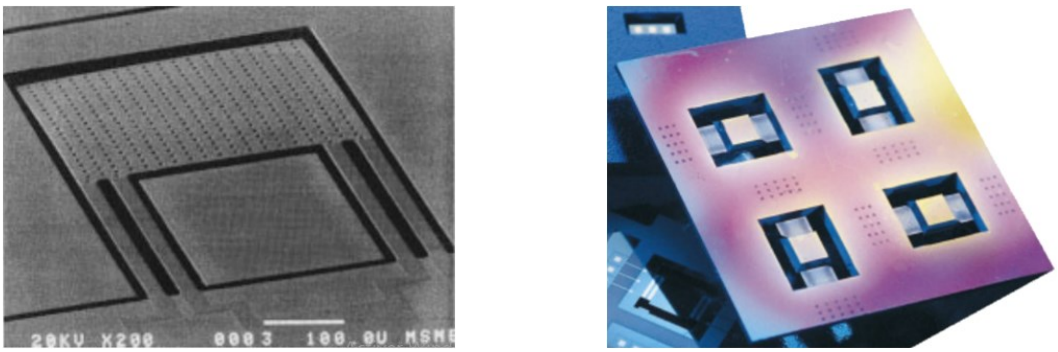

(a) (b)

Figure 1.8. *(a) surface micromachined ZnO piezoelectric accelerometer released using XeF2 (Devoe and Pisano 2001) and (b) Bulk micromachined ZnO piezoelectric accelerometer with KOH etched proof mass (De Reus, Gullov et al. 1999).*

The simple detection circuits needed for piezoelectric accelerometers give them the advantage of low power consumption and low noise floor. These sensors can operate in a large frequency range from 2Hz to about 25kHz and in a wide temperature range up to 120°C. High sensitivity values have been reached with piezoelectric accelerometers using PZT materials due to their high electromechanical coupling coefficients and piezoelectric constants (Wang, Wolf et al. 2003). Unfortunately, piezoelectric accelerometers are difficult to manufacture at low

cost. In addition, they are susceptible to drift as a result of harsh environmental conditions and mechanical shocks. Therefore, regular in-field calibration is often required.

1.2.2.3 MEMS capacitive accelerometer

Capacitive transduction is one of the most used methods for acceleration measurement. As previously, its principle relies on the measurement of a proof mass displacement. Initially, two conductive plates, one of them is attached to the proof mass and the other is fixed to the frame, form a capacitor with an initial value C given by:

$$C = \frac{S\,\varepsilon_0\,\varepsilon_r}{d} \qquad (1)$$

With:

- *S,* the in-sight surface of the capacitor (m^2)
- ε_0, is the permittivity of vacuum (ε_0=8,85418782.10^{-12} F.m^{-1})
- ε_r, is the relative permittivity of the medium between the electrodes
- *d*, is the distance between the plates (m)

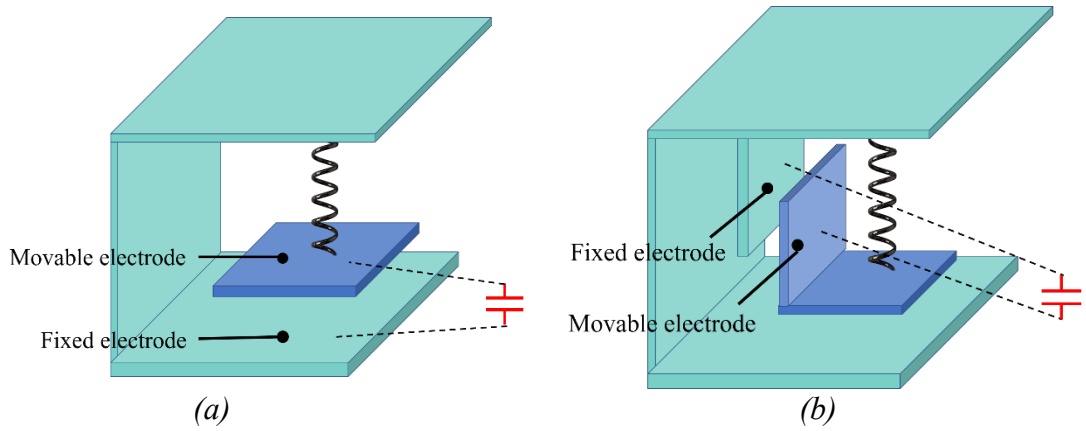

Figure 1.9. *Working principle of (a) variable distance based and (b) variable surface based capacitive accelerometer.*

Displacement of the proof mass may change capacitance by changing either the surface S of the in-sight electrodes or the distance d between them. As both sensing modes can be implemented in the same technology, they are used together to implement 3-axis accelerometers. Illustrations of capacitive accelerometers that depends on the distance change and electrode surface change are presented in Figure 1.9 (a) and (b) respectively. The conditioning circuit that converts the capacitance change into an electrical signal can be more or less complicated based on the applications and specifications requirements.

Capacitive accelerometers are best known for their low cost, low power requirements and relative insensitivity to temperature variations. This makes them a good option for embedded systems in harsh environments where important temperature variations are imposed (Stauffer 2006). However, due to their capacitive nature, these accelerometers are very sensitive to electromagnetic interferences. Capacitive accelerometers are not very shock resistant, since a high enough acceleration can cause breakage at the anchor points where mechanical constraints are concentrated.

The sensitivity of capacitive accelerometers is limited either by the distance *d* between the two plates or the in-sight surface *S*. To improve sensitivity, a "comb" shape structure is generally used to increase the in-sight surface *S* of the accelerometer and then the nominal capacitance. Figure 1.10. shows the structure of a commercialized combo-type capacitive accelerometer (Samuels 1996).

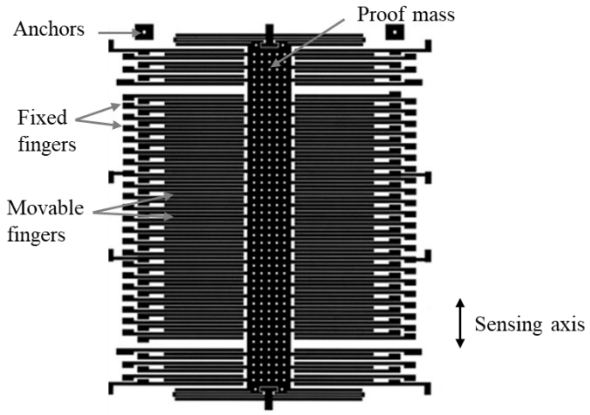

Figure 1.10. *Schematics of the commercial capacitive accelerometer ADXL150***.**

1.2.2.4 MEMS convective accelerometer

Convective accelerometers are based on a completely different transduction mode. It is distinguished by the absence of a solid proof mass which is replaced by a heated gas volume that moves under the effect of acceleration. Figure 1.11.(a) illustrates the structure of a convective accelerometer, which is composed of a suspended heater and surrounding equidistant detectors in a micromachined cavity. Without acceleration, the temperature is symmetrically distributed in the cavity and temperature detectors measure the same temperature as shown in Figure 1.11.(b). An acceleration applied along the sensitive axis modifies the

natural convection movements in fluid and induces a temperature variation proportional to the acceleration and measured by the thermal detectors.

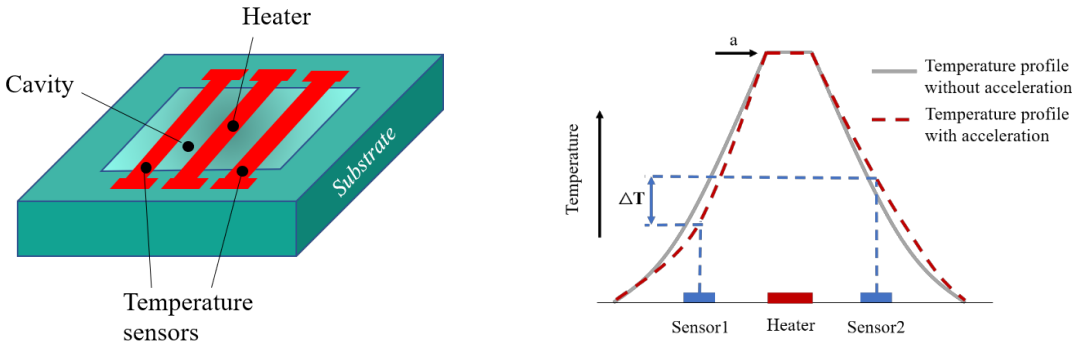

(a) *(b)*

Figure 1.11. *Working principle of a convective accelerometer: (a) accelerometer's structure and (b) corresponding temperature profile in the cavity.*

Different from other accelerometers, acceleration is not directly converted into an electrical signal, but rather converted into a temperature variation that is further converted into an electrical variation usually by means of other conversion detectors, usually thermistors (Luo, Li et al. 2003, Liao, Chen et al. 2006) or thermocouples (Lin and Jones 2005). An example of commercialized 3-axis convective accelerometer is presented in Figure 1.12.

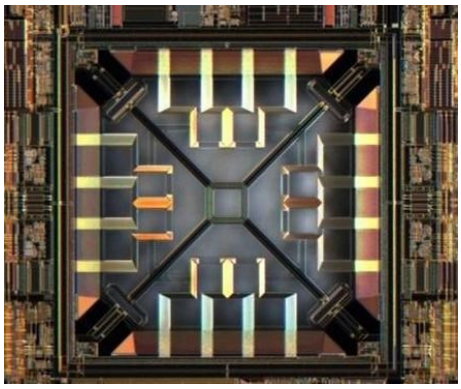

Figure 1.12. *3-axis convective accelerometer commercialized by MEMSIC.*

The simplicity of convective accelerometer makes it completely compatible with CMOS process using only FSBM post-processing, which reduces considerably fabrication costs. The absence of proof mass gives to the sensor a very high shock resistance up to 50000g. High-g

measurements up to 10000g can be achieved by optimizing geometrical parameters of the sensor (Garraud, Combette et al. 2011).

Unfortunately, the bandwidth of convective accelerometers compared to competitors is low. It was found that bandwidth can be improved by using lighter thermal detectors, smaller cavity and larger gas diffusivity, but this solution decreases the sensitivity as well. Some researchers have proposed closed-loop configurations to improve bandwidth. This solution aims to cancel the impact of the response time of the detectors by placing additional resistors close to the detectors to maintain their temperature constant. Using this configuration, the bandwidth was improved from 66Hz to 1025Hz using nitrogen at atmospheric pressure as a gas media (Garraud, Combette et al. 2011, Garraud, Combette et al. 2012). An alternative to this solution is based on self-heating modulation of the detectors to keep their temperature constant (Leman *et al*. 2009).

Sensitivity in convective accelerometers is challenging as it highly depends on power consumption for heat generation. Therefore, finding a trade trade-off between sensitivity and power consumption for convective accelerometer is important.

1.2.3 Comparison of MEMS accelerometers parameters

Accelerometer's transduction method must be chosen according to the targeted application and its requirements. As seen in previous section, different advantages and drawbacks are associated to each transduction principle (see Table 1.1).

Table 1.1. *Strengths and drawbacks of different MEMS accelerometers (Garraud 2011).*

Transduction	Advantages	Drawbacks
Piezoresistive	• No significant zero shift after a strong shock • Low sensitivity to external interferences	• Low sensitivity • Highly sensitive to temperature variations • Low resistance to shocks.
Piezoelectric	• High frequency response • Large measurement range	• High sensitivity to temperature variations

	• Low to no power required (self-powered)	• Limited DC response due to leakage current in piezoelectric material • Low output level
Capacitive	• Low sensitivity to temperature • High resolution • Low fabrication cost • Low power consumption	• Low resistance to shocks and vibrations • Susceptible to electromagnetic interference (EMI)
Convective	• Very high shock resistance due to the absence of moving parts • Continuous power supply • Low fabrication cost • Absence of proof mass	• High power consumption • Low frequency bandwidth • Sensitivity to temperature variations

1.3 MEMS convective accelerometers and their limitations

1.3.1 Theory of thermal transfer

The general principle of convective accelerometer relies on a micrometric-scale heating source that generates a temperature gradient in a closed chamber filled with a fluid (gas or liquid). To understand how convective accelerometer works, it is necessary to first understand heat transfer mechanisms. Heat transfer is an energy transfer that results from a temperature difference or gradient where heat flows from higher temperature areas to lower temperature ones. Main mechanisms are conduction, convection, and radiation. All these three mechanisms of thermal exchange take place within a convective accelerometer in different amounts.

1.3.1.1 Thermal conduction

Thermal conduction is a heat transfer by diffusion that tends to homogenize heat distribution between two objects in contact. These objects can be solid, liquid or gas, and can have different compositions or physical states. In thermal conduction, heat transfer takes place without macroscopic displacement of the matter, but rather happens on microscopic scale where kinetic energy is transferred between agitating particles through collisions. When two particles collide,

energy is transferred from the particle with the higher temperature to the one with lower temperature. The cumulation of all these collisions results in a heat flux that depends on temperature difference, material's thickness, size of contact surface and thermal properties of materials. Conductive heat flow through a solid between two surfaces at temperatures T_1 and T_2 with $T_1>T_2$ in steady-state conditions is illustrated in Figure 1.13. and given by Fourier law:

$$\Phi_{cd} = -\lambda S \frac{dT}{dx} \quad (2)$$

With

- Φ_{cd}, the conductive heat flux along x axis (W)
- S, the section, i.e., material surface perpendicular to the x axis (m^2)
- λ, the thermal conductivity of the material (W. m^{-1}. K^{-1})

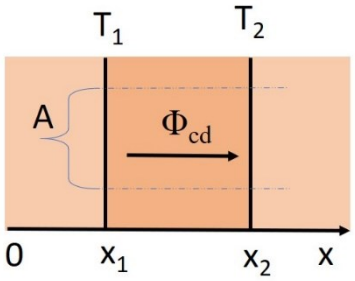

Figure 1.13. *Conductive heat flow in steady-state conditions.*

1.3.1.2 Thermal convection

Heat transfer by convection occurs between a hot surface and a fluid in motion by means of macroscopic movement of the fluid. Convection can be free or forced depending on the origin of the movement mechanism. Free convection is driven by buoyant forces and appears naturally once a gravitational field and a fluid density variation are present: fluid close to the solid and hot surface increases in temperature and its density becomes lower. Under the effect of Archimedes force, the heated air goes up leaving the place to a cold fluid that get heated itself. A fluid motion is therefore created naturally. If the fluid motion is induced by an external force, such as a fan, blower or pump, convection is called forced.

Heat exchange between solid and fluid at different temperatures is a problem that involves fluid motion. In fact, fluid motion and the heat flow are two superimposed phenomena that both interact to define the temperature distribution. Therefore, it is crucial to combine the equations of motion and energy conservation. Resolving these equations is mathematically difficult.

However, a practical solution for the majority of applications was proposed by Prandtl, where the viscosity influence is assumed to be restricted in a thin layer near the solid surface called thermal boundary layer. Within this layer, thermal transfer is a conductive flow from the solid to the gas. The boundary layer thickness depends on physical properties and velocity of the fluid and can be defined as the zone in which the temperature variations are the higher. Fluid flow in this layer is laminar, and the heat flow is perpendicular to the solid surface. Finally, the heat flow from a solid wall at a temperature T_s to a fluid at an average temperature T_f through the boundary layer, illustrated in Figure 1.14, is given by Fourier law:

$$\Phi_{cv} = \frac{\lambda}{\delta_T} S\,(T_s - T_f) \tag{3}$$

With:

- Φ_{cv}, the convective heat flow (W)
- S, the exchange surface (m^2)
- λ, the thermal conductivity of the fluid (W. m^{-1}. K^{-1})
- δ_T, the thickness of the thermal boundary layer (m)

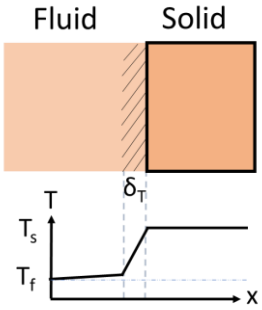

Figure 1.14. *Representation of convective thermal transfer between fluid and solid.*

Since it is hard to estimate the thickness of the thermal boundary layer, the convective heat transfer coefficient h is introduced, so the heat flow expression becomes:

$$\Phi_{cv} = h\,S\,(T_s - T_f) \tag{4}$$

With $h = \lambda/\delta_T$ *(W. m^{-2}.K^{-1}),* the convective heat transfer coefficient.

Inside cavity of convective accelerometers, it was found that heat transfer by conduction is much higher than convection one. Therefore, heat profile in the fluid is mostly governed by conduction. However, although heat convection mechanism is not dominant in heat transfer

from the heater to the surrounding fluid, the small amount of convective flow is responsible for the working principle of convective accelerometers. This convective flow deforms the temperature profile in the cavity by modifying the buoyancy forces applied to the fluid under the effect of acceleration. As this deformation is not symmetric, it induces a temperature difference between the detectors that can be later transformed into an output signal.

1.3.1.3 Thermal radiation

Thermal radiation refers to the electromagnetic waves emitted by a body at temperature T to transfer its internal energy. Thermal radiation is emitted from any solid and liquid, in addition to some gases (such as water vapor, carbon dioxide, methane, …), and the presence of a physical medium is not required to for heat transfer. On a macroscopic scale, heat transfer by thermal radiation can be calculated using the Stefan Boltzmann law that gives the emitted energy flux by a blackbody (ideal emitter):

$$M^0(T) = \sigma T^4 \tag{5}$$

With the constant of Stefan Boltzmann $= 5.67 \times 10^{-8}\, Wm^{-2}K^{-4}$.

In case of a convective accelerometer, the heater is at high temperature and thus, energy emission by radiation dominates. A heating resistance with an average temperature of 600K emit -ideally- around 7.3 mW.mm^{-2}. Since this value is the energy flux emitted by a blackbody, the real value is in fact lower. Therefore, the contribution of heat transfer by radiation in convective accelerometer operation can be generally neglected.

1.3.2 Working principle of MEMS convective accelerometers

1.3.2.1 Heat generation

The heat source, or heater, is an important element of a convective accelerometer. Generally, a resistor heats up the surrounding material, due to joule effect and conduction, once supplied by a DC current. Heating temperature ranges generally between 400K and 700K, and an initial temperature distribution is set in the cavity. Temperature raise is then a function of the power dissipation, and the heater's temperature (T_H) is given by:

$$T_H = T_A + R_{TH}\frac{U^2}{R} \tag{6}$$

With:

- T_A, the ambient temperature (K)
- R_{TH}, the absolute thermal resistance of the heater (K/W)
- U, the voltage across the resistor (V)
- R, the heating resistance (Ω)

Due to thermal sensitivity of resistive material, heating resistance changes with temperature as approximated by:

$$R(T) = R_0(1 + \alpha_1 \Delta T + \alpha_2 \Delta T^2) \quad (7)$$

With:

- $R(T)$, the heating resistance evaluated at a temperature T (Ω)
- R_0, the heating resistance at ambient temperature T_0 (Ω)
- α_1, the linear thermal coefficient of resistivity (K^{-1})
- α_2, the quadratic thermal coefficient of resistivity (K^{-2})
- ΔT, the temperature difference $T - T_0$ (K)

1.3.2.2 Heat distribution without acceleration (Fluid conduction)

As explained in section 1.3.1.2, the contact between the heater and the fluid creates a thermal layer trough which conductive heat transfer takes places.

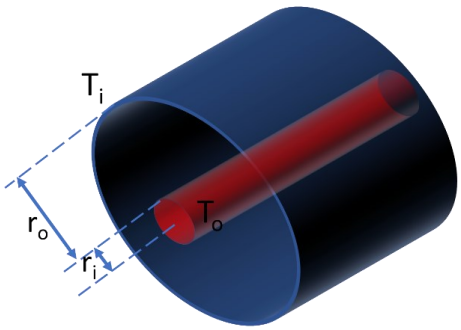

Figure 1.15. *Cylindrical modeling of convective accelerometer.*

Work was done (Mailly 2002) to estimate the initial temperature distribution in the cavity using the law of Fourier given in (2) on a simplified model of a single-axis convective accelerometer. This model is presented in Figure 1.15, where the heating source and the cavity are modeled as two concentric cylinders of r_i and r_o radius and T_i and T_o temperatures respectively. In addition, the effect of detectors on the temperature distribution is neglected and

the average temperature of the heating source is considered. Without acceleration, heat exchanges in the cavity are considered purely conductive. Using these assumptions, the radial temperature distribution in the cavity is given by:

$$T(r) = T_i - (T_i - T_o)\frac{\ln(r/r_i)}{\ln(r_o/r_i)} \quad (8)$$

1.3.2.3 Heat distribution in presence of an acceleration

The distribution of temperature as a function of acceleration was mathematically investigated (Garraud 2011) by resolving the Navier-Stokes equations assuming a negligible natural convective flow compared to the conductive one. This assumption is mathematically represented by a low Rayleigh number *Ra*, which is a dimensionless number that characterizes the fluid's flow regime. The expression of the Rayleigh number is given by:

$$Ra = \frac{\rho^2 \beta C_p}{\mu\lambda}\, a(T_i - T_o) r_i^3 \quad (9)$$

With:

- ρ, the density of the fluid (kg.m^{-3})
- β, the coefficient of thermal expansion (K^{-1})
- C_p, the specific heat (J.kg^{-1}.K^{-1})
- μ, the dynamic viscosity of the fluid (N.s.m^{-2})
- λ, the thermal conductivity (W.m^{-1}.K^{-1})
- a, the applied acceleration (g)
- $(T_i - T_o)$, the temperature difference between the heater and the bulk substrate (K)
- r_i, the characteristic length of the device.

It was found (Garraud 2011) that the temperature difference δT between two detectors, placed at a distance *r* in both sides of the heater, is proportional to the applied acceleration, to the Rayleigh number *Ra*, and to a function *T** that depends on *r*, r_o, r_i:

$$\delta T(r^*, R^*) = 2R_a \varepsilon^* T^*(r^*, R^*) \quad (10)$$

With:

- $r^* = r/r_i$

- $\varepsilon^* = (T_i - T_o)/T_o$
- $T^* = T/T_o$
- $R^* = r_o/r_i$

By dividing the temperature difference δT by the applied acceleration, the sensitivity of the sensor S (in K/g) is therefore (Garraud 2011):

$$S = 2\frac{\rho^2 \beta C_p}{\mu\lambda}(T_i - T_o)^2 r_i^3 T^*(r^*, R^*) \quad (11)$$

1.3.2.4 Temperature sensing

The role of temperature sensors, or detectors, in the convective accelerometer is to convert temperature variations into an electrical signal. This conversion can be done using either thermocouples (Lin and Jones 2005, Tsang, Ma et al. 2008) or thermistors (Luo, Li et al. 2003, Chaehoi, Mailly et al. 2006). Using thermocouples, usage of a biasing voltage can be avoided. Moreover, their sensitivity can be improved once they are connected in serial configuration to form a thermopile. In the case of thermistor, generally made of metal or polysilicon, the Temperature Coefficient of Resistance (TCR) is the main parameter that controls the detector's sensitivity to temperature variations (cf.Eq (7)

1.3.3 Development of MEMS convective accelerometers

1.3.3.1 One and two axis convective accelerometers

The working principle of a micromachined convective accelerometer is based on heat transfer by free convection in a fluid enclosed inside a sealed cavity. The general design of a single-axis accelerometer is illustrated in Figure 1.16(a). The structure of the device consists of a micromachined cavity in a silicon substrate. A bridge supporting a heating resistance is suspended above the cavity and located at its center. The heater is surrounded by two equidistant detectors (generally thermistors or thermocouples). The overall device is sealed with a cover package to prevent the external air flow from disturbing the system. Using the same working principle, a dual axis accelerometer consists of a planar central heater attached to the cavity edges with four attachment bridges as illustrated in Figure 1.16(b). Two pairs of detectors are placed orthogonally along both x and y axis and equidistantly from the heater. The use of four detectors makes the sensor able to measure acceleration in both x and y directions.

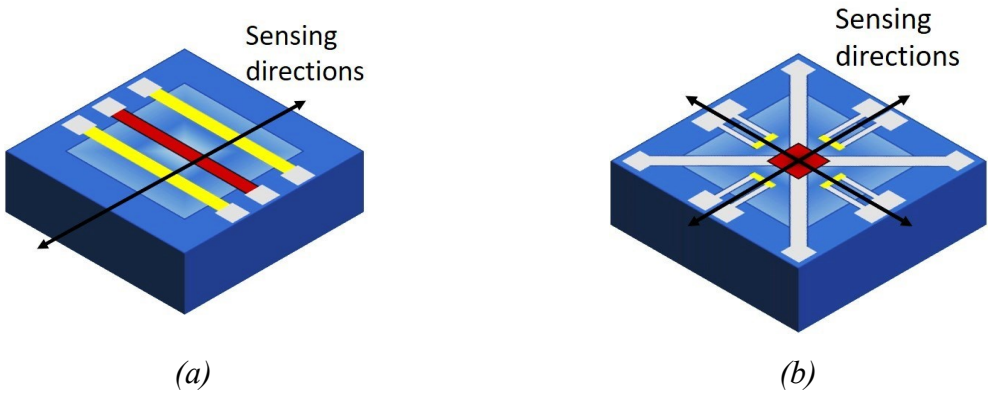

Figure 1.16. *Illustrations of (a) uniaxial and (b) dual-axis convective accelerometer structure.*

Once the heater is powered, the surrounding fluid (or liquid) heats up creating a symmetrical hot bubble. Temperature distribution around the heater is illustrated in Figure 1.17; without acceleration, all temperature sensors measure an equal temperature. The presence of a lateral acceleration tends to move the heat bubble in the direction of the acceleration due to natural convection forces. Therefore, temperature distribution in the cavity becomes asymmetrical and a temperature difference proportional to the applied acceleration is measured by detectors and conditioned by an appropriate circuit that transforms temperature variations into voltage.

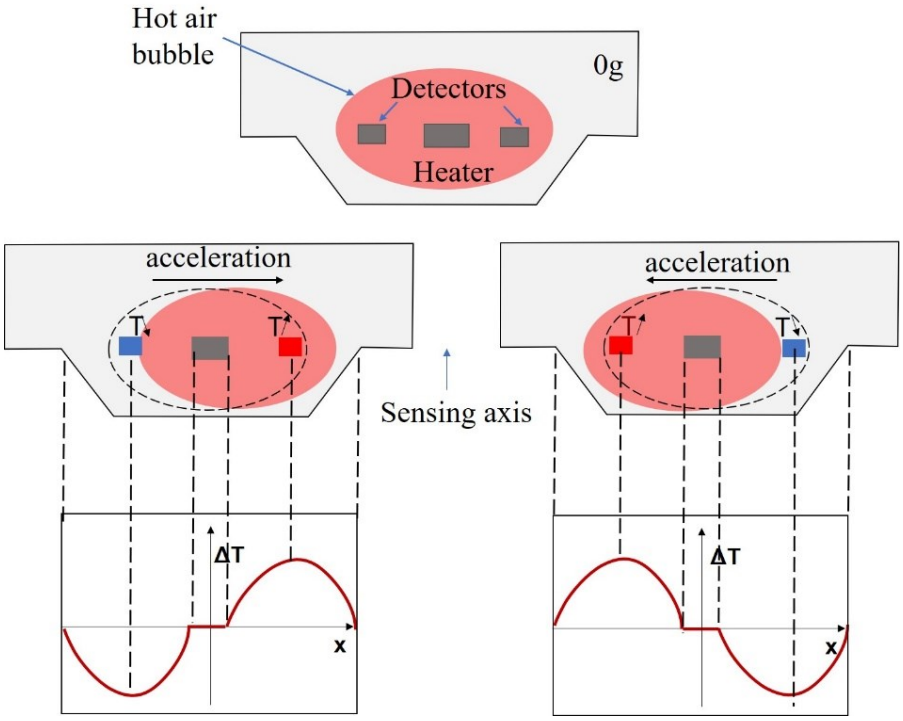

Figure 1.17. *Representation of the working principle of convective accelerometer due to lateral acceleration.*

Convective accelerometer was firstly patented in the 40s (Weber 1943, Zworykin 1945), but the first implementation of the concept on silicon substrate using microelectronics technologies to create a single axis sensor was reported in 1997 (Leung, Jones et al. 1997). In 2001 (Billat, Glosch et al. 2001, Billat, Glosch et al. 2002), a convection-based inclinometer that can be used as an accelerometer, was reported. This inclinometer, presented in Figure 1.18, was fabricated using silicon-on-insulator (SOI) technology, which is a more expensive alternative of silicon wafer.

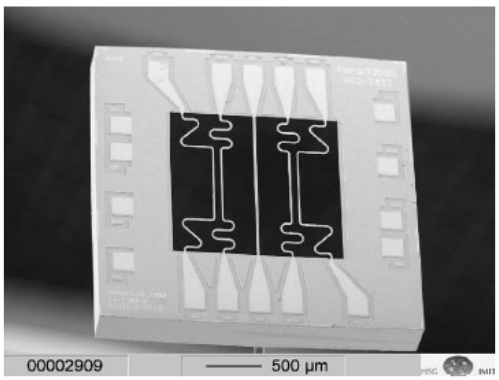

Figure 1.18. *SEM picture of a convective accelerometer fabricated using SOI technology (Billat, Glosch et al. 2002).*

For integrated electronics, SOI technology gives the advantage of superior process control and higher device performance. In (Billat, Glosch et al. 2001, Billat, Glosch et al. 2002), a lightly doped silicon is used for the heater and temperature detectors, and the overall device was sealed in a TO-8 metal package. Both air and SF6 were used as working fluid. With air, sensitivity and response time reached 132µV/K and 110ms respectively with a 45mW heating power. However, by replacing the air with a denser fluid (SF6), the sensitivity has improved to 6.6 mV/K while the response time increases up to 240ms.

Another innovative convective accelerometer was fabricated (Lin and Jones 2005), where the gas in the cavity was replaced by a high-density fluid (isopropanol). Compared to an air-filled accelerometer, the sensitivity increased about 700 times at the cost of an increasing response time by one order of magnitude. SOI technology was also used in a convective accelerometer reported in (Dao, Dau et al. 2006, Dao, Sugiyama et al. 2007). The reported dual-axis accelerometer consists of four thermistors that can deform freely with the temperature in order to reduce the thermally induced stress. The thermistors were arranged in a ring-shape around a central heater as illustrated in Figure 1.19. The sensor output was conditioned using

an off-chip circuit. The sensor demonstrated a sensitivity of 13mV/g in an operating range of ±5g, its resolution reached 0.12mg and its total noise was 0.33 µV.

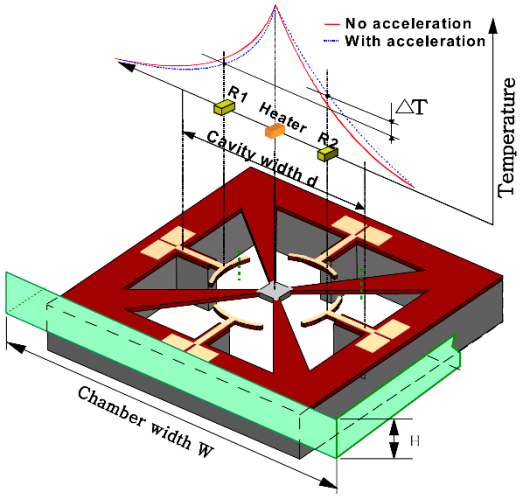

Figure 1.19. *Schematic view of a dual axis convective accelerometer with sensing elements arranged in a ring-shape (Dao, Sugiyama et al. 2007).*

More recently, a thermal accelerometer was implemented on an organic substrate (Petropoulos, Moschos et al. 2011). This technique ensured a high-level of thermal insulation. However, electrical insulation was ensured by adding an SU-8 layer between resistors and the operating fluid (water). A high sensitivity of about 59mV/g was reported.

The feasibility of a convective accelerometer with a bandwidth of 1025 Hz was demonstrated by a research group from University of Montpellier (Garraud, Combette et al. 2012). Nitrogen was used as a fluid medium while detectors were implemented in a closed-loop configuration to cancel their thermal response time. This research group also demonstrated high performances in term of measurement range that reached 10,000g by optimizing the cavity size and heating temperature (Garraud, Combette et al. 2011).

1.3.3.2 Three axis convective accelerometers

The development of a convective accelerometer able to detect acceleration along three axis is challenging since it requires generally a more complicated structure than the simple design of a single or dual axis accelerometer. Tsang et al. (Tsang, Ma et al. 2008) have developed two designs of tri-axial convective accelerometer by integrating polymeric materials in MEMS process in order to provide the needed mechanical flexibility. The first design, illustrated in Figure 1.20 (a) consists of a vertical plate for z-axis measurement assembled with an in-plane

sensitivity measurement platform. The buckled cantilever design presented in Figure 1.20(b) consists of two heaters placed at the centers of two separate sensing plates.

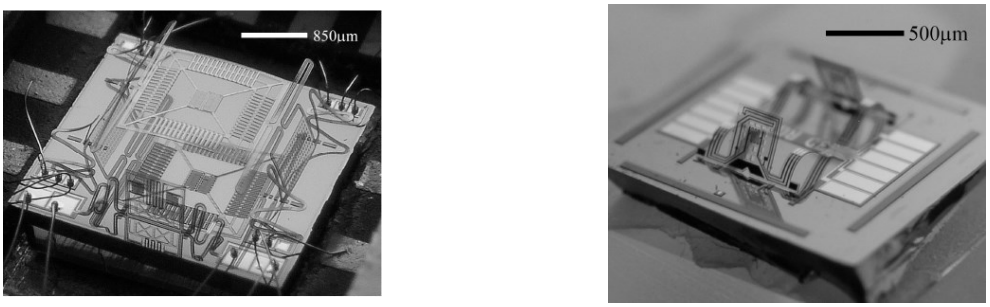

(a) *(b)*

Figure 1.20. *Photomicrograph of the (a) assembled elevated platform and (b) buckled cantilever triaxial convective accelerometers (Tsang, Ma et al. 2008).*

Both sensor's structures were fabricated with Polymide PI-2611 on a Si substrate. The out-of-plane assembly was realized by wire-bonding to provide z-axis sensitivity as well as thermal isolation. Using SF6 as a fluid medium, sensitivity of the first design reached 45µV/g, 60µV/g, and 35µV/g for X, Y, and Z axis respectively. The second design has shown a sensitivity of 17µV/g, 8.5µV/g, and 14µV/g respectively.

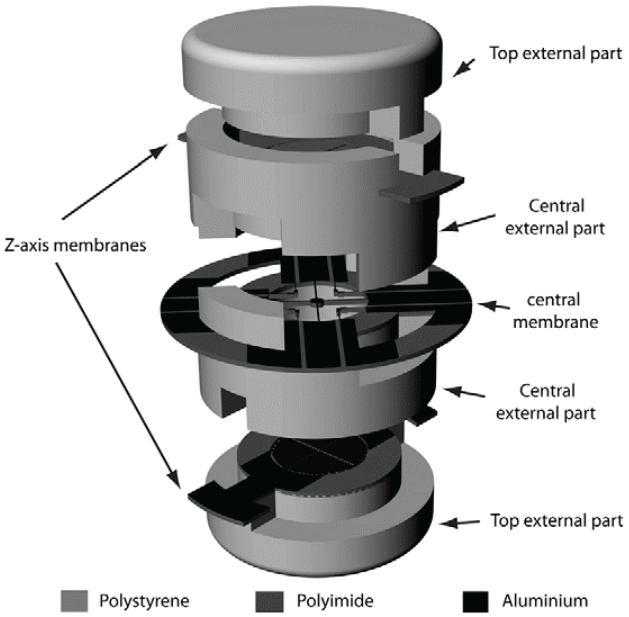

Figure 1.21. *Drawing of the polymeric 3-axis convective accelerometer with different parts used for the device assembling (Rocha, Silva et al. 2011).*

The buckled cantilever accelerometer was later improved. The structure consists of two sensor plates attached to a cantilever in order to create the out-of-plane structure. The sensor then reached sensitivities of 66, 64, and 25 µV/g respectively (Bahari, Leung et al. 2011). Later, Rocha et al. (Rocha, Silva et al. 2011) proposed a three-axis convective accelerometer fabricated by combining MEMS technology with microinjection molding to bring flexibility to the design. As shown in Figure 1.21, the design consists of three flexible polyimide membranes. Central membrane hosts the heater and in-plane temperature sensors while the upper and lower ones include z-axis temperature sensors. Poor performances were obtained with sensitivities limited to 8 mV/g for in-plane axis and 2.2 mV/g for z-axis for a power consumption of 45 mW (Silva, Noh et al. 2015). Using two five-wire structures, another triaxial convective accelerometer was fabricated (Li, Chang et al. 2019). Reported in-plane and out-of-plane sensitivities reached 16.1mV/g and 18.4mV/g respectively with a linearity range of 0-6g for accelerations at 20Hz.

1.3.4 CMOS MEMS convective accelerometers

1.3.4.1 CMOS MEMS convective accelerometers

The first reported CMOS convective accelerometer was a single axis sensor fabricated using a 2µm CMOS process (Milanovi, Bowen et al. 1998, Milanović, Bowen et al. 2000). With thermopiles as temperature detectors, a sensitivity of 136µV/g was achieved for a power consumption of 81mW. A better sensitivity of 146µV/g was obtained using a thermistor with higher power consumption of about 430mW. Linear range from 0 to 7g was reported for both devices. The thermopile-based sensor is presented in Figure 1.22.

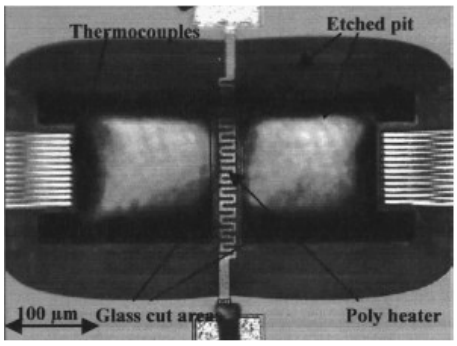

Figure 1.22. *Microphotograph of the CMOS compatible convective accelerometer from (Milanović, Bowen et al. 2000) with thermopile configuration.*

In 2001, Luo et al. improved the sensitivity up to 600µV/g while decreasing the power consumption to 87mW by optimizing geometrical parameters and replacing air by a more efficient gas (Luo, Yang et al. 2001). The use of a porous silicon layer for thermal isolation allowed Goustouridis group to further improve the sensitivity of a single axis convective accelerometer to reach 13mV/g for a power of 166mW (Goustouridis, Kaltsas et al. 2004). This sensor is presented in Figure 1.23.

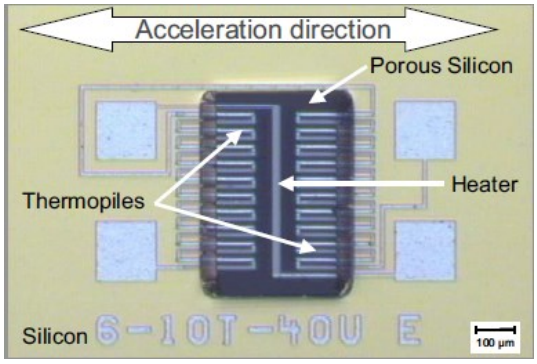

Figure 1.23. *CMOS compatible convective accelerometer based on porous silicon thermal isolation (Goustouridis, Kaltsas et al. 2004).*

Another single axis convective accelerometer, presented in Figure 1.24 was fabricated using the AMS 0.8µm CMOS process and demonstrated a sensitivity of about 375mV/g with a heating power and temperature of 35mW and 438°C (Chaehoi, Mailly et al. 2006). The cavity of 740×740µm^2 was etched using a FSBM process. Poly-Si resistors were implemented as heating source and thermistors as temperature detectors (Chaehoi, Mailly et al. 2006, Leman, Mailly et al. 2008). These detectors were arranged in an on-chip Wheatstone bridge. The chip also hosts a CMOS amplifier with programable gain for signal conditioning. The device presented a good linearity up to 10g, a resolution of 30mg and a -3dB-bandwidth of 14.5Hz.

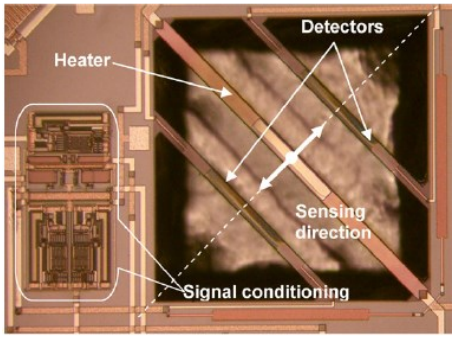

Figure 1.24. *SEM picture of convective accelerometer fabricated in CMOS process with on-chip signal conditioner (Chaehoi, Mailly et al. 2006).*

The first CMOS compatible dual axis convective accelerometer was proposed by Chen. The sensor was realized using the TSMC 0.35µm CMOS process. Achieved sensitivity was 22µV/g for both x and y axis for a power consumption of about 9mW (Chen and Shen 2008). The sensor consisted of two pairs of thermopiles used as temperature detectors and connected with the micro heater in a net structure to ensure mechanical rigidity as illustrated in Figure 1.25.

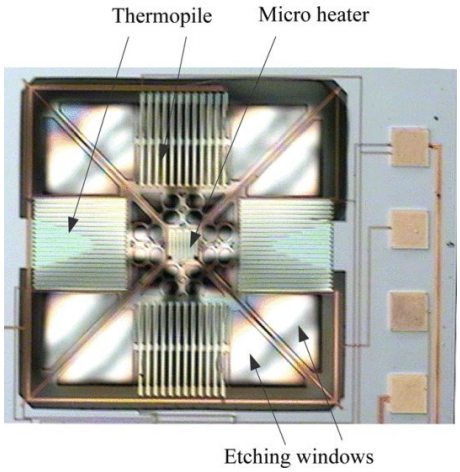

Figure 1.25. *Dual axis convective accelerometer fabricated using TSMC 0.35 µm 2P4M CMOS process (Chen, Shen et al. 2008).*

Another two-axis convective accelerometer was reported in (Garraud, Giani et al. 2010, Garraud, Giani et al. 2011, Garraud, Giani et al. 2011). This device, presented in Figure 1.26, was fabricated using 0.35µm CMOS process from AMS. The sensor consists of a 100×100µm^2 heater in a meander shape implemented in a 600×600µm^2 cavity. Using Al/poly-Si thermopiles for temperature sensing, a sensitivity of about 0.024K/g was demonstrated. This low sensitivity is caused by the low Seebeck coefficient of the thermopiles which is 6.54µV/K, and also by the low heating temperature of 200°C. However, a high linearity was demonstrated up to 150g.

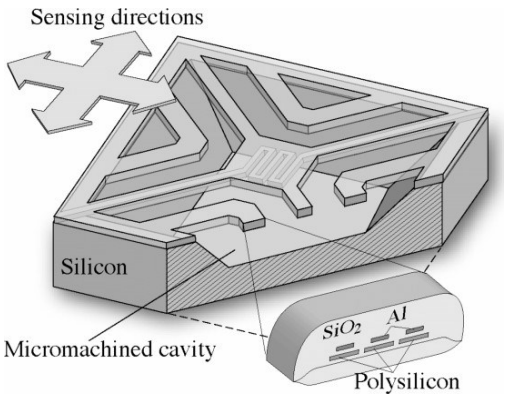

Figure 1.26. *Cross-sectional view of a two axis convective accelerometer fabricated using a 0.35 µm CMOS technology (Garraud, Giani et al. 2011).*

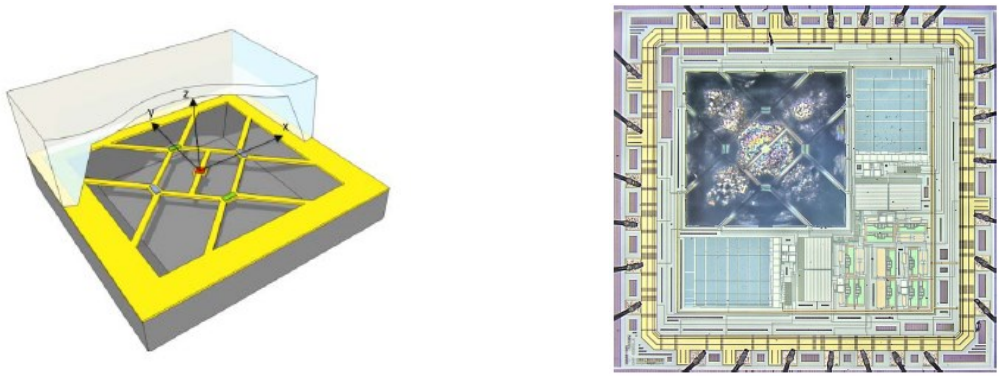

(a) *(b)*

Figure 1.27. *(a) 3D structure illustration and (b) SEM picture of a CMOS monolithic 3-axis convective accelerometer (Mailly, Nguyen et al. 2014, Nguyen, Mailly et al. 2015).*

A fully-integrated 3-axis convective accelerometer was reported by Mailly et al. This sensor was fabricated using a standard AMS 0.35µm CMOS technology followed by a FSBM etching process (Mailly, Nguyen et al. 2014, Nguyen, Mailly et al. 2015). It did not involve a tridimensional complicated structure therefore; no complex assembly operations were required. Thus, the proposed structure is similar to that of Figure 1.26 but out-of-plane acceleration is deduced from common-mode temperature of in-plane detectors. An illustration of the sensor's structure and a micro-photograph of the fabricated device are presented in Figure 1.27(a) and Figure 1.27(b), respectively. Measurement principle in the out-of-plane axis is based on asymmetry along the z-axis due to a larger top cavity than the bottom etched cavity. As a result, isotherms were found to be stretched upward in case of positive out-of-plane acceleration and flattened downwards in case of a negative one with a limited but existing linear range. In-plane detectors (placed along x- and y-axis) were used to measure differential temperature variations due to in-plane accelerations, or common mode temperature variations due to out-of-plane accelerations. Measurement principle will be extensively presented later in this document.

A fabricated sensor was tested and sensitivities of 8.8mV/g, 12.6mV/g and 0.45 mV/g were reported for x, y and z axis respectively for a heating power of 8.3mW. The low out-of-plane sensitivity compared to in-plane ones was explained to a lack of optimization in terms of both geometry and position of temperature detectors.

Last but not least, a three-axis convective accelerometer, based on a similar sensing principle, is commercialized for years by MEMSIC™ (Jiang, Cai et al. 2013).

1.3.4.2 Advantages and limitations of CMOS-MEMS convective accelerometers

A monolithic CMOS-MEMS convective accelerometer combines both the mechanical part, i.e., the sensor, and signal processing circuit on the same die. Both mechanical and electrical components are fabricated by combining a CMOS process with MEMS specific post-process for etching some material and releasing suspended elements (e.g., Front-Side Bulk Micromachining FSBM). This integration leads to significant cost reduction for large volume production due to batch fabrication. Accelerometers fabricated using non-traditional technologies generally demonstrate a higher level of performance but at the price of a very high cost per part.

Also, noise is a major parameter for sensors as it defines the minimum level of useful signal. Despite their small size and thus their limited sensitivity, CMOS-MEMS allows compact systems, with conditioning circuits closer to sensor, with reduced noise levels and therefore with higher sensor's resolution. Additional advantage of CMOS-MEMS is the strong reduction of stray capacitance, inductance, and resistance due to package and interconnects between sensor part and conditioning circuit.

However, limitations are faced due to a limited number of layers and materials of the CMOS manufacturing process, for the realization of the mechanical parts. Optimization during design of sensor is minimal and must cope with CMOS fabrication sequence, CMOS material properties and thicknesses, minimum widths and spacings.

Another limitation of CMOS MEMS is the etched-cavity size. This important parameter has a significant impact on the convective accelerometer's sensitivity (Luo, Li et al. 2002) and is limited since the fabrication cost relates to the size of the die. The depth of the cavity, that affects the sensitivity as well (Rekik, Mezghani et al. 2011), is limited by the substrate thickness and the etching rate of the FSBM post-process. This etching rate is typically 1µm/min, but exposing the sensor to the etching solution for more than four hours can damage the passivation layer of the electronic circuit. Therefore, the cavity of a CMOS convective accelerometer is typically no more than 300µm deep.

A real challenge facing CMOS convective accelerometers is the integration of the third axis since it requires classically a tridimensional structure which is not compatible with a standard CMOS technology that is strictly planar.

On the other hand, the micromachining technology progresses allowed to create three-dimensional structures. Therefore, one of the major problems of a monolithic CMOS

convective accelerometer is its comparatively lower sensitivity, especially the out-of-plane one, regarding the accelerometers fabricated using customized fabrication processes.

Conclusion

This chapter has presented a broad overview on MEMS technology and its different fields of applications. In the case of accelerometers, micromachining have led to miniaturization and performance improvement. For convective accelerometers, the combination of MEMS and CMOS technologies have led to many advantages such as cost and size reduction. However, the use of CMOS technology implies some limitations in terms of optimization of geometry and constrained design space and thus in the so-obtainable performances. In this thesis, our work will be particularly focused on improving the low out-of-plane sensitivity that results from planarity of CMOS technology in CMOS-MEMS convective accelerometers.

REFERENCES

Bahari J, Leung AM., « Micromachined three-axis thermal accelerometer with a single composite heater », *Journal of Micromechanics and Microengineering*, vol. 21, n° 7, 2011, p. 075025.

Becker EW., Ehrfeld W., Hagmann P., Maner A., Münchmeyer D., « Fabrication of microstructures with high aspect ratios and great structural heights by synchrotron radiation lithography, galvanoforming, and plastic moulding (LIGA process) », *Microelectronic engineering*, vol. 4, n° 1, 1986, p. 35-56.

Billat S., Glosch H., Kunze M., Hedrich F., Frech J., Auber J., Lang W., Sandmaier H., Wimmer W., « Convection-based micromachined inclinometer using SOI technology », *Technical Digest. MEMS 2001. 14th IEEE International Conference on Micro Electro Mechanical Systems (Cat. No. 01CH37090)*, 2001, p. 159-161.

Billat S., Glosch H., Kunze M., Hedrich F., Frech J., Auber J., Sandmaier H., Wimmer W., Lang W., « Micromachined inclinometer with high sensitivity and very good stability », *Sensors and Actuators A: Physical*, vol. 97, 2002, p. 125-130.

Chaehoi A., Mailly F., Latorre L., Nouet P., « Experimental and finite-element study of convective accelerometer on CMOS », *Sensors and Actuators A: Physical*, vol. 132, n° 1, 2006a, p. 78-84.

Chaehoi A., Mailly F., Latorre L., Nouet P., « Experimental and finite-element study of convective accelerometer on CMOS », *Sensors and Actuators A: Physical*, vol. 132, n° 1, 2006b, p. 78-84.

Chen H., Bao M., Zhu H., Shen S., « A piezoresistive accelerometer with a novel vertical beam structure », *Sensors and Actuators A: Physical*, vol. 63, n° 1, 1997, p. 19-25.

Chen S., Shen C., « A novel two-axis CMOS accelerometer based on thermal convection », *IEEE Transactions on Instrumentation and Measurement*, vol. 57, n° 8, 2008a, p. 1572-1577.

Dao DV., Dau VT., Hayashida M., Dinh TX., Shiozawa T., Sugiyama S., « Fabrication and characterization of 2-dof micro convective accelerometer », *SENSORS*, 2006, p. 1353-1356.

Dao R., Morgan DE., Kries HH., Bachelder DM., « Convective accelerometer and inclinometer », U.S. patent, 5581034A, 1996.

Dau VT., Dao DV., Sugiyama S., « A 2-DOF convective micro accelerometer with a low thermal stress sensing element », *Smart materials and structures*, vol. 16, n° 6, 2007, p. 2308.

De RR., Gulløv JO., Scheeper PR., « Fabrication and characterization of a piezoelectric accelerometer », *Journal of Micromechanics and Microengineering*, vol. 9, n° 2, 1999, p. 123.

Department, Statistica Research. April 2016, « Global forecast by application for MEMS market 2015-2021 », accessed 18 May. 2021. https://www.statista.com/statistics/797003/worldwide-mems-market-forecast-application/.

DeVoe DL., Pisano AP., « A fully surface-micromachined piezoelectric accelerometer », *Proceedings of International Solid State Sensors and Actuators Conference (Transducers' 97)*, 1997, p. 1205-1208.

DeVoe DL., Pisano AP., « Surface micromachined piezoelectric accelerometers (PiXLs) », *Journal of Microelectromechanical Systems*, vol. 10, n° 2, 2001, p. 180-186.

Doll JC., Corbin EA., King WP., Pruitt BL., « Self-heating in piezoresistive cantilevers », *Applied physics letters,* vol. 98, n° 22, 2011, p. 223103.

Dong P., Li X., Yang H., Bao H., Zhou W., Li S., Feng S., « High-performance monolithic triaxial piezoresistive shock accelerometers », *Sensors and Actuators A: Physical*, vol. 141, n° 2, 2008, p. 339-346.

Garraud A., Amélioration des performances et nouveau concept de détecteurs de capteurs inertiels à détection thermique, Thèse de doctorat, Université Montpellier II-Sciences et Techniques du Languedoc, 2011.

Garraud A., Combette P., Deblonde A., Loisel P., Giani A., « Closed-loop micromachined accelerometer based on thermal convection », *Micro and Nano Letters*, vol. 7, n° 11, 2012, p. 1092-1093.

Garraud A., Combette P., Gosalbes JM., Charlot B., Giani A, « First high-g measurement by thermal accelerometers », *16th International Solid-State Sensors, Actuators and Microsystems Conference*, 2011.

Garraud A., Combette P., Pichot F., Courteaud J., Charlot B., Giani A., « Frequency response analysis of an accelerometer based on thermal convection », *Journal of Micromechanics and Microengineering*, vol. 21, n° 3, 2011a, p. 035017.

Garraud A., Giani A., Combette P., Charlot B., Richard M., « A Dual Axis CMOS frontside bulk micromachined thermal accelerometer », *Symposium on Design Test Integration and Packaging of MEMS/MOEMS (DTIP)*, 2010.

Garraud A., Giani A., Combette P., Charlot B., Richard M., « A dual axis CMOS micromachined convective thermal accelerometer », *Sensors and Actuators A: Physical,* vol. 170, n °1-2, 2011c, p. 44-50.

Garraud A., Giani A., Combette P., Charlot B., Richard M., « A dual axis CMOS micromachined convective thermal accelerometer », *Sensors and Actuators A: Physical*, vol. 170, n° 1-2, 2011d, p. 44-50.

Gilleo K., *MEMS/MOEMS Packaging*, In McGraw-Hill Companies, Inc., 220, 2005.

Goel S., Gupta N., « Design, optimization and analysis of reconfigurable antenna using RF MEMS switch », *Microsystem Technologies*, vol. 26, n° 9, 2020, p. 2829-2837.

Goustouridis D., Kaltsas G., Nassiopoulou AG., « A CMOS compatible thermal accelerometer without solid proof mass, based on porous silicon thermal isolation », *SENSORS*, 2004, p. 848-851.

Hewa-Kasakarage NN., Kim D., Kuntzman ML., Hall NA., « Micromachined piezoelectric accelerometers via epitaxial silicon cantilevers and bulk silicon proof masses », *Journal of microelectromechanical systems*, vol. 22, n° 6, 2013, p. 1438-1446.

Hua Y., Jiang L., Cai Y., Leung A., Zhao Y., « Single chip tri-axis accelerometer », U.S. Patent 20070101813, Sep. 16, 2005.

Huang S., Li X., Song Z., Wang Y., Yang H., Che L., Jiao J., « A high-performance micromachined piezoresistive accelerometer with axially stressed tiny beams », *Journal of Micromechanics and Microengineering*, vol. 15, n° 5, 2005, p. 993.

Hudson TD., McMillen DK., Ashley PR, Ruffin PB., Baeder J., « Micro-electro-mechanical system (MEMS) component research and development for army missile applications », *Acquisition, Tracking, and Pointing XIII*, 1999.

Jiang L., Cai Y., Liu H., Zhao Y., « A micromachined monolithic 3 axis accelerometer based on convection heat transfer », *The 8th Annual IEEE International Conference on Nano/Micro Engineered and Molecular Systems*, 2013, p. 248-251.

Kal S., Das S., Maurya DK., Biswas K., Ravi Sankar A., Lahiri SK., « CMOS compatible bulk micromachined silicon piezoresistive accelerometer with low off-axis sensitivity », *Microelectronics Journal,* vol. 37, n° 1, 2006, p. 22-30.

Kim SC., Wise KD., « Temperature sensitivity in silicon piezoresistive pressure transducers », *IEEE Transactions on Electron Devices*, vol. 30, n° 7, 1983, p. 802-810.

Kuells R., Nau S., Salk M., Thoma K., « Novel piezoresistive high-g accelerometer geometry with very high sensitivity-bandwidth product », *Sensors and Actuators A: Physical*, vol. 182, 2012, p. 41-48.

Latorre L., Nouet P., « A complete methodology for electro-mechanical characterization of a CMOS compatible MEMS technology », *IEICE transactions on electronics*, vol. 82, n° 4, 1999, p. 582-588.

Leman O., Mailly F., Latorre L., Nouet P. « A wide bandwidth, wide dynamic range thermal architecture for convective accelerometers », *Proceedings of IEEE Sensors (Proc. IEEE Sens)*, 2009, p. 1828-1831.

Leman O., Mailly F., Latorre L., Nouet P., « HDL modeling of convective accelerometers for system design and optimization », *Sensors and Actuators A: Physical*, vol. 142, n° 1, 2008, p. 178-184.

Leung AM., Jones J., Czyzewska E., Chen J., and Pascal M., « Micromachined accelerometer with no proof mass », *International Electron Devices Meeting. IEDM Technical Digest*, 1997, p. 899-902.

Li X., Yin L., Hu J., Lang L., Liu J., Xia Y., Fang D., Zhang H., « Electro-thermally actuated RF MEMS switch for wireless communication », *IEEE 5th International Conference on Nano/Micro Engineered and Molecular Systems*, 2010, p. 497-500.

Li Z., Chang W., Sun S., Gao C., Hao Y., «A novel MEMS 3-axis thermal accelerometer with 5-wire structure using planar stacking method», *20th International Conference on Solid-State Sensors, Actuators and Microsystems & Eurosensors XXXII*, 2019, p. 1819-1822.

Liao KM., Chen R., Chou BCS., « A novel thermal-bubble-based micromachined accelerometer », *Sensors and Actuators A: Physical*, vol. 130, 2006, p. 282-289.

Lim MK., Du H., Su C., Jin WL., « A micromachined piezoresistive accelerometer with high sensitivity: design and modelling », *Microelectronic Engineering*, vol. 49, n° 3-4, 1999, p. 263-272.

Lin L., Jones J., « A liquid-filled buoyancy-driven convective micromachined accelerometer », *Journal of microelectromechanical systems*, vol. 14, n° 5, 2005, p. 1061-1069.

Luo XB., Li Z. X., Guo Z. Y., Yang Y. J., «Thermal optimization on micromachined convective accelerometer», *Heat and mass transfer*, vol. 38, 2002, p. 705-712.

Luo XB., Li ZX., Guo ZY., Yang YJ., « Study on linearity of a micromachined convective accelerometer », *Microelectronic Engineering*, vol. 65, n° 1-2, 2003, p. 87-101.

Luo XB., Yang YJ., Zheng F., Li ZX., Guo ZY., « An optimized micromachined convective accelerometer with no proof mass », *Journal of Micromechanics and Microengineering,* vol. 11, n° 5, 2001, p. 504-508.

Mailly F., « Etude et réalisation de microcapteurs thermiques : anémomètre et accéléromètre thermique » Thèse de doctorat, Montpellier 2, 2002.

Mailly F., Nguyen HB., Latorre L., Nouet P., « CMOS implementation of a 3-axis thermal convective accelerometer », *SENSORS*, *2014 IEEE*, 2014, p. 1471-1474.

Milanovi V., Bowen E., Tea N., Suehle J., Payne B., Zaghloul M., Gaitan M., « Convection-based accelerometer and tilt sensor implemented in standard CMOS », 1998.

Milanović, V., Bowen E., Zaghloul M., Tea N., Suehl JS., Payne B., Gaitan M., « Micromachined convective accelerometers in standard integrated circuits technology », *Applied Physics Letters*, vol. 76, n° 4, 2000, p. 508-510.

Nguyen HB., Mailly F., Latorre L., Nouet P., « A new monolithic 3-axis thermal convective accelerometer: principle, design, fabrication and characterization », *Microsystem Technologies*, vol. 21, n° 9, 2015, p. 1867-1877.

Ning Y., Loke Y., McKinnon G., « Fabrication and characterization of high g-force, silicon piezoresistive accelerometers », *Sensors and Actuators A: Physical*, vol. 48, n° 1, 1995, p. 55-61.

Partridge A., Reynolds JK., Chui BW., Chow EM., Fitzgerald AM., Zhang L., Maluf NI., Kenny TW., « A high-performance planar piezoresistive accelerometer », *Journal of microelectromechanical systems*, vol. 9, n° 1, 2000, p. 58-66.

Peckerar MC., Maldonado JR., « X-ray lithography-an overview », *Proceedings of the IEEE*, vol. 81, n° 9, 1993, p. 1249-1274.

Petropoulos A., Moschos A., Athineos S., Kaltsas G., « A thermal accelerometer directly integrated on organic substrate », *Procedia Engineering*, vol. 25, 2011, p. 643-646.

Robert Ph., Nguyen V., Hentz S., Duraffourg L., Jourdan G., Arcamone J., Harrisson S, « M&NEMS: A new approach for ultra-low cost 3D inertial sensor », *SENSORS, 2009 IEEE*, 2009, p. 963-966.

Rocha LA., Silva CS., Cerqueira MF., Ribeiro JF., Goncalves LM., Pontes AJ., Viana JC., « A microinjected 3-axis thermal accelerometer », *Procedia Engineering*, vol. 25, 2011, p. 607-610.

Samuels H., « Single-and Dual-axis Complete Micromachined Accelerometers », *Analog Dialogue*, vol. 30, n° 4, 1996, p. 3-5.

Schröpfer G., Elflein W., Labachelerie MD., Porte H., Ballandras S., « Lateral optical accelerometer micromachined in (100) silicon with remote readout based on coherence modulation », *Sensors and Actuators A: Physical*, vol. 68, n° 1-3, 1998, p. 344-349.

Silva C., Noh J., Fonseca H., Pontes A., Gaspar J., Rocha LA., « Fabrication and characterization of polymeric three-axis thermal accelerometers », *Journal of Micromechanics and Microengineering,* vol. 25, n° 8, 2015, p. 085005.

Smith CS., « Piezoresistance effect in germanium and silicon », *Physical review*, vol. 94, n° 1, 1954, p. 42.

Stauffer JM., « Current capabilities of MEMS capacitive accelerometers in harsh environment », *Proceedings of IEEE/ION PLANS*, vol. 21, no° 11, 2006, p. 29-32.

Tilli M., Paulasto-Kröckel M., Petzold M., Theuss H., Motooka T., and Lindroos V., *Handbook of silicon based MEMS materials and technologies*, Elsevier, 2020.

Tsang SH., Ma AH., Karim SK., Parameswaran A., Leung AM., « Monolithically fabricated polymermems 3-axis thermal accelerometers designed for automated wirebonder assembly », *IEEE 21st International Conference on Micro Electro Mechanical Systems*, 2008, p. 880-883.

Wang LP., Ginsburg E., Gerfers F., Samara-Rubio D., Weinfeld B., Ma Q., Rao V., He MY., « Sputtered A1N Thin Films for Piezoelectric MEMS Devices », *SENSORS, 2006 IEEE*, 2006, p. 10-13.

Wang LP., Wolf RA., Wang Y., Deng KK., Zou L., Davis RJ., Trolier-McKinstry S., « Design, fabrication, and measurement of high-sensitivity piezoelectric microelectromechanical systems accelerometers », *Journal of microelectromechanical systems*, vol. 12, n° 4, 2003, p. 433-439.

Warneke B., Hoffman EG., Pister KSJ., « Monolithic multiple axis accelerometer design in standard CMOS », *Micromachined Devices and Components*, 1995.

Weber H.E., « Accelerometer», U.S. patent, 2455394, Jun.,1943.

Zheng G., Papapolymerou J., « Monolithic reconfigurable bandstop filter using RF MEMS switches », *International Journal of RF, Microwave Computer-Aided Engineering,* vol. 14, n° 4, 2004, p. 373-382.

Zou H., Chen F., Wang J., Bao H., Li X., « MEMS monolithic tri-axis high-shock accelerometers with MHz-level ultra-high resonant frequency », *IEEE 30th International Conference on Micro Electro Mechanical Systems (MEMS)*, 2017, pp. 327-330.

Zou H., Wang J., Chen F., Bao H., Jiao D., Zhang K., Song Z., Li X., « Monolithically integrated tri-axis shock accelerometers with MHz-level high resonant-frequency », *Journal of Micromechanics and Microengineering*, vol. 27, n° 7, 2017b, p. 075009.

Zworykin V.K., «Convection current responsive instrument», U.S. patent, 2440189, Apr., 1945.

Chapter 2: Sensitivity enhancement of a 3-axis convective accelerometer

Introduction

The main drawback of convective accelerometers is the proportionality between sensitivity and power consumption. In this chapter, two potential solutions are proposed and studied to improve sensitivity, especially in the out-of-plane axis, without increasing power consumption. In section 2.1, an existing planar 3-axis CMOS MEMS accelerometers is described. Then, in section 2.2, a first improved design is proposed. It consists in a modified design that will combine convection in the cavity and displacement of the heater to improve out-of-plane sensitivity. Finally, in section 2.3, a second solution is investigated to improve energy-efficiency thanks to an optimized shape of heater to increase both in-plane and out-of-plane sensitivities without increasing power consumption.

2.1 Existing 3-axis CMOS MEMS convective accelerometer

2.1.1 Measurement of out-of-plane acceleration using a planar convective accelerometer

To measure out-of-plane acceleration using the planar structure of a convective accelerometer, the key parameter is vertical asymmetry between the top cover and the bottom cavity. To better explain the working principle of the sensor, a cross section of the sensor is presented in Figure 2.1 (a) when no acceleration is applied. The hot bubble generated by the heater is represented by the red circle. Its shape is initially symmetrical according to *xOz* plane in the absence of acceleration. However, it is asymmetrical according to *xOy* plane due to the asymmetry between the top and bottom cavities. With this configuration, both detectors measure the same temperature: the common mode temperature.

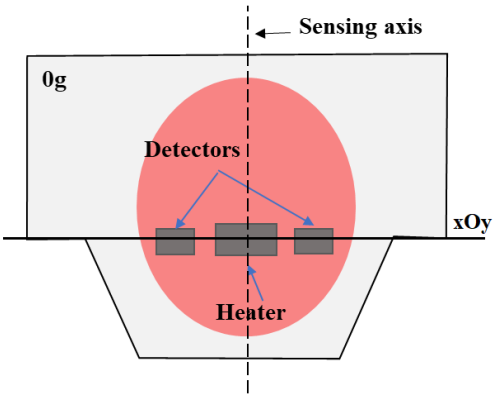

(a)

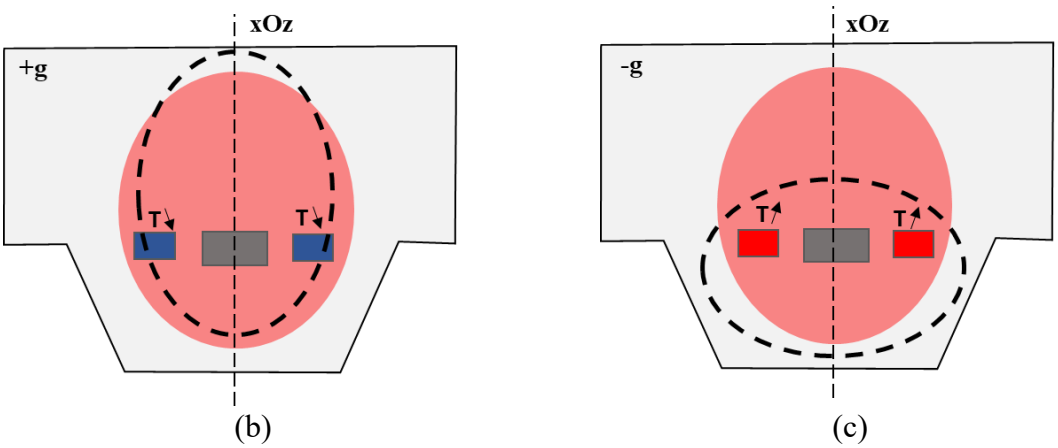

Figure 2.1. *Principle of out-of-plane acceleration measurement of a three-axis convective accelerometer: (a) hot bubble shape in absence of acceleration and its deformation (dashed line) due to a (b) positive or a (c) negative acceleration.*

By applying an out-of-plane acceleration on the sensor, a deformation of the hot bubble is observed. As presented in Figure 2.1 (b), a positive acceleration stretches the hot bubble along z-axis (*xOz*) which results in a temperature decrease in the *xOy* plane. at the contrary, a negative acceleration tends to flatten the hot bubble and therefore the temperature of the detectors increases as illustrated in Figure 2.1 (c).

This measurement technique was used to create a planar CMOS-compatible triaxial convective accelerometer (Nguyen 2013).

2.1.2 Limitations of the existing design

The existing planar 3-axis convective accelerometer consists of a square shaped heater attached by two arms that are interconnected with the detector's bridges in a spider web structure (Nguyen 2013). All suspended structures are 45°-oriented to facilitate etching process. At each detector location in the *xOy* plane, resistances for in-plane and out-of-plane acceleration sensing are implemented together. Figure 2.2 illustrates this sensor, which will be used as a reference in this chapter.

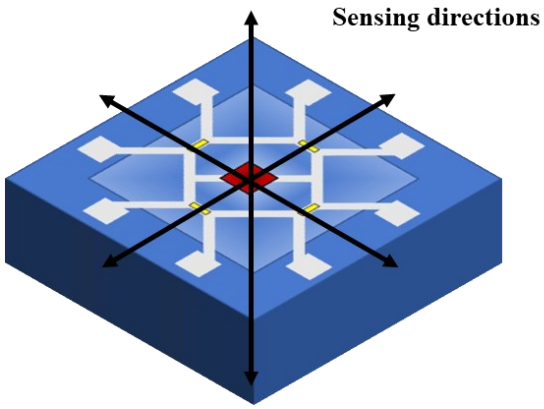

Figure 2.2. *artist view of a planar three-axis convective accelerometer (Nguyen 2013).*

Geometric parameters of the existing device are listed in Table 2.1 with respect to dimensions presented in Figure 2.3.

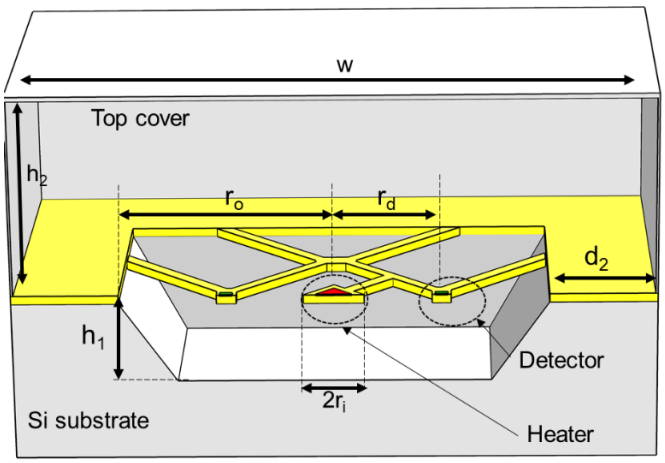

Figure 2.3. *Simplified cross-sectional view of a 3-axis thermal accelerometer from (Nguyen 2013) with main dimensions.*

Table 2.1. *Geometrical parameters of State-of-the-Art device (Nguyen 2013).*

Symbol	Description	Value	Unit
r_d	Distance from heater center to detector	240	µm
r_i	Heater half width	45	µm
r_o	Bottom cavity half width	500	µm
h_1	Bottom cavity depth	190	µm

Symbol	Description	Value	Unit
h_2	Top cover height	1	mm
d_2	Distance from bottom cavity edge to top cover	2.5	mm
w	Top cover width = $2(r_o + d_2)$	7	mm

Initially, in-plane and out-of-plane sensitivities for this State-of-the-Art design have been assessed through 2D FEM simulations. Main problem with a 2D model is that sensor's geometry is represented as a cross sectional view where a single in-plane axis, *xOz*, exists. Geometry along y-axis is considered as infinite. Since sensitivity of convective accelerometer is strongly affected by size of heater, top cover and bottom cavity, extending infinitely these dimensions along y-axis leads to enlarge the hot bubble surrounding the heater and therefore to overestimate sensitivity in both in-plane and out-of-plane directions. This was observed in (Nguyen, 2013), where experimental in-plane sensitivities were measured about five times below expectations. The over-estimation in 2D simulations rise to one order of magnitude for sensitivity to out-of-plane accelerations.

Another drawback of 2D geometry simplification is the misplacement of detectors as it was pointed out in (Mezghani, Tounsi et al., 2013). In a 3D FEM model, optimal position for temperature detectors got closer to the heater. This has led to place detectors away from their optimal location and therefore decrease sensor sensitivity.

In the following, 3D FEM modeling will be used to optimize detectors' position, heater's design and detectors' bridges and to predict more precisely sensor performances.

2.2 Mechanical solution for sensitivity enhancement

2.2.1 Presentation of the mechanical solution

Convective accelerometer commonly takes advantage of the natural convection of air, or any other gas, in a closed cavity that changes the heat distribution and induces a temperature variation in presence of an acceleration. Temperature variation is later converted into an electrical signal. However, the so-obtained temperature variation, in other terms the sensitivity, is relatively low due to small dimensions, especially for out-of-plane accelerations. In an innovative idea, we propose to increase the temperature variations in the cavity using a mechanical solution that allows the heater plate to move vertically whenever an out-of-plane

acceleration is applied. This solution can be implemented using flexible suspension bridges to connect the heater to substrate as presented in Figure 2.4.

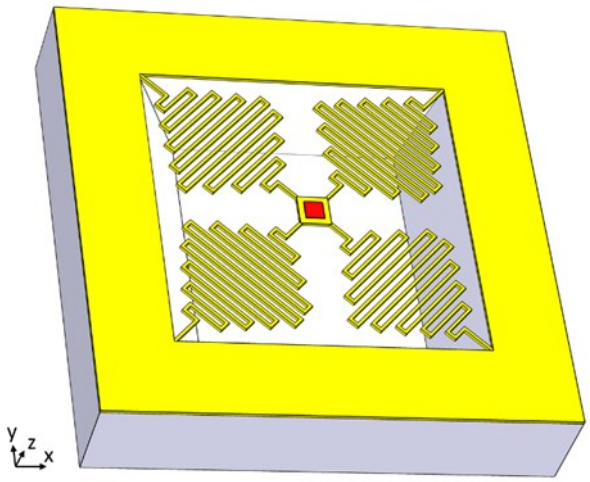

Figure 2.4. *Proposed design of a 3-axis convective accelerometer with flexible bridges.*

In the proposed solution, the heater is used as a seismic mass that moves vertically under the effect of an out-of-plane acceleration. The heater is attached to the cavity borders with four flexible bridges forming a spring-mass system. Inertial force that is created on the heater plate, when an acceleration is applied, is given by:

$$\vec{F} = m\,\vec{a} = -k\,z\,\overrightarrow{ez} \tag{12}$$

With:

- $\vec{F}$, the force applied on the heater plate (N)
- m, the heater mass (kg)
- $\vec{a}$, the acceleration vector (m/s^2)
- k, the spring stiffness (N/m)
- z, the displacement of the heater (m)
- $\overrightarrow{ez}$, the unity vector of z axis.

Therefore, the heater displacement is a function of acceleration, mass and spring constant in the form:

$$z = -\frac{m}{k}a = \frac{ml^3}{4E_m w d^3}a \tag{13}$$

With

- l, the length of supporting bridges (m)
- w, the beam width (m)
- d, the beam thickness (m)
- E_m, the equivalent young's modulus of the bridge ($kg.m^{-1}.s^{-2}$)

From the above equation, the heater plate and its surrounding hot bubble, moves away from the lateral non-moving detectors in the opposite direction of the z-axis acceleration. This produces a shift in the isotherms along z-axis and exposes all four lateral detectors to a different isotherm which induces a temperature variation. To clearly illustrate the principle, Figure 2.5 and Figure 2.6 present the heater and surrounding isotherms with and without displacement due to 1000g positive and negative accelerations, respectively.

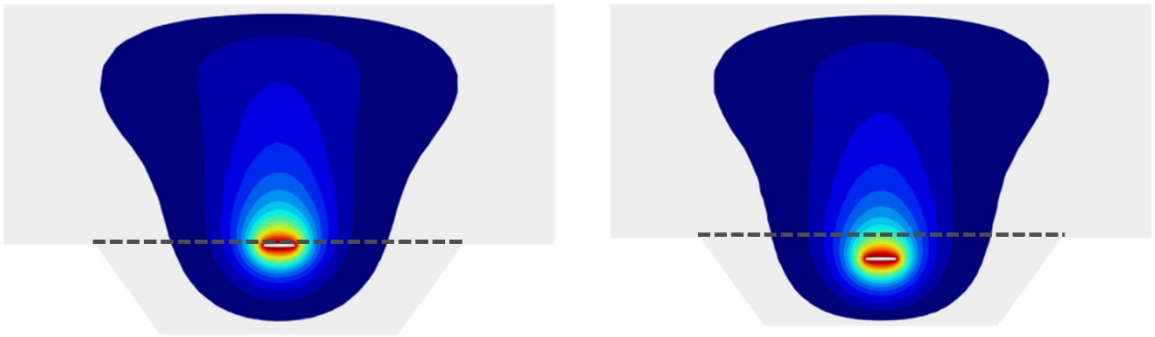

(a) (b)

Figure 2.5. *Simulated isotherms for a +1000g out-of-plane acceleration (a) without and (b) with an acceleration-induced heater displacement.*

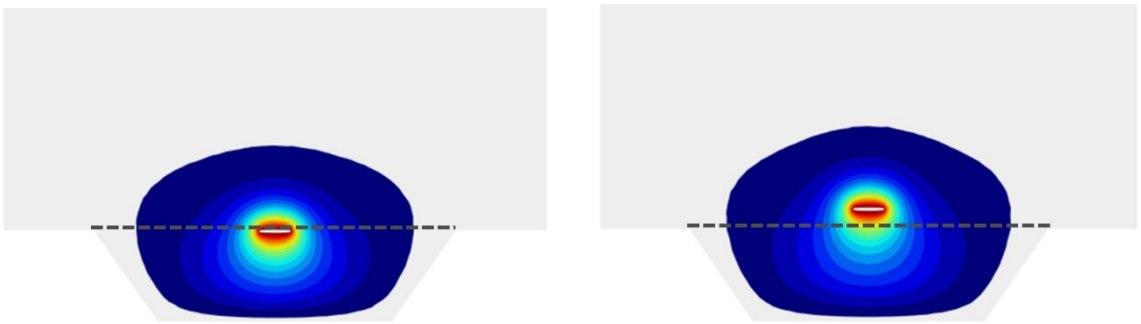

(a) (b)

Figure 2.6. *Simulated isotherms for a -1000g out-of-plane acceleration (a) without and (b) with an acceleration-induced heater displacement.*

By comparing the so-obtained isotherms in presence of a heater displacement, it is clear that the displacement of the hot bubble surrounding the heater moves along the vertical axis together with the heater. Assuming that detectors stay in the same plane, one can expect a higher change in common-mode temperature measured by detectors and thus a higher sensitivity.

To better explain the efficiency of the proposed solution, temperature profiles along x-axis, where detectors are located, are plotted in Figure 2.7 for conventional and flexible designs. Without acceleration, the temperature profile (T_0) is identical for both structures. Under acceleration, the temperature profile ($T_{acc\ rigid}$) obtained for a conventional rigid design is small even for a large acceleration of 1000 g. A variation of less than 20K is obtained for detectors located at equal distance between the heater and the border of the cavity. On the contrary, the temperature profile ($T_{acc\ flexible}$) is clearly modified for the moving heater and it is obvious that, if detectors are located close to the heater, sensitivity will increase up to about 100K.

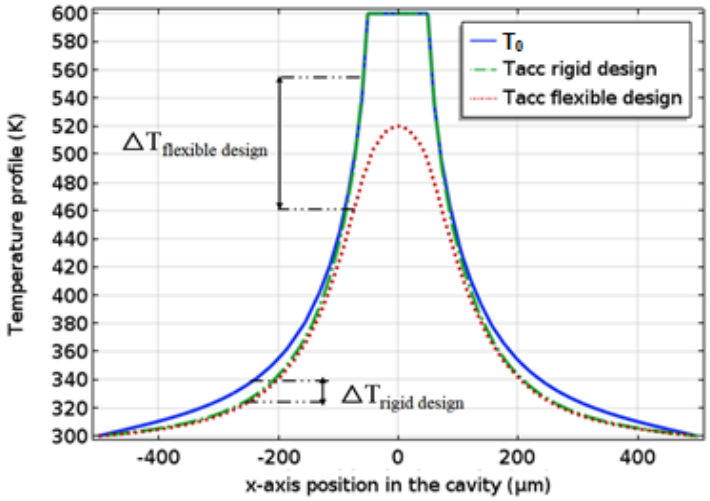

Figure 2.7. *Temperature profiles along the x-axis for z-axis accelerations of 0 g (T_0) and +1000 g for rigid (Tacc rigid) and flexible (Tacc flexible) designs.*

2.2.2 Numerical investigation of the mechanical solution

2.2.2.1 Numerical modeling environment

3D FEM simulations are performed on the reference structure described in previous section. Several *physics* modules have been used to implement heat transfer phenomena, that take place inside the accelerometer bottom cavity and top cover, together with mechanical aspects of the heater and its supporting bridges. These *physics* modules include:

- *Heat transfer* to model thermal distribution inside a closed volume of air. Here, temperature of substrate and top cover walls is defined as ambient, whereas temperature at the heater edges is set to 600K.
- *Laminar flow* to compute velocity and pressure fields. Here, a volume force is defined to express the influence of acceleration on the flow.
- *Fluid structure interaction* to model couplings between structural mechanics and fluid dynamics and to describe interactions between a moving and deformable solid and the surrounding fluid. Here, a load is applied on the heater and its attachment bridges. This load represents the inertial force per volume unit resulting from the acceleration.

Last but not least, the cavity is considered as a closed volume filled with a compressible and non-turbulent fluid with temperature-dependent properties.

2.2.2.2 Determination of the optimal location for detectors

Different designs have been simulated to compare optimal location of detectors:

- *Design 1* composed of a square-shaped heater of about 100 µm side length, attached to the cavity boundaries using four straight and rigid beams.
- *Design 2* composed of the same heater as *Design 1* but with four zig-zag-shaped flexible suspension bridges.
- *Design 3* similar to *Design 2* but with an additional seismic mass on top of the heater.

Design 3 will be studied in next section. Figure 2.8 presents acceleration-induced temperature variations along the x-axis due to a negative 1g acceleration along z-axis.

By comparing the temperature variation given by the flexible design and the rigid one, according to Figure 2.8, two main conclusions can be stated:

- A maximal sensitivity of about 11mK/g is demonstrated for *Design 1* if detectors are located roughly at equal distance between heater center and cavity boundary. At this location, sensitivity of *Design 2* is comparable.
- When detectors are placed closer to the heater, a clear increase of sensitivity for *Design 2* is demonstrated. A maximum would be obtained for detectors located at the heater's boundaries.

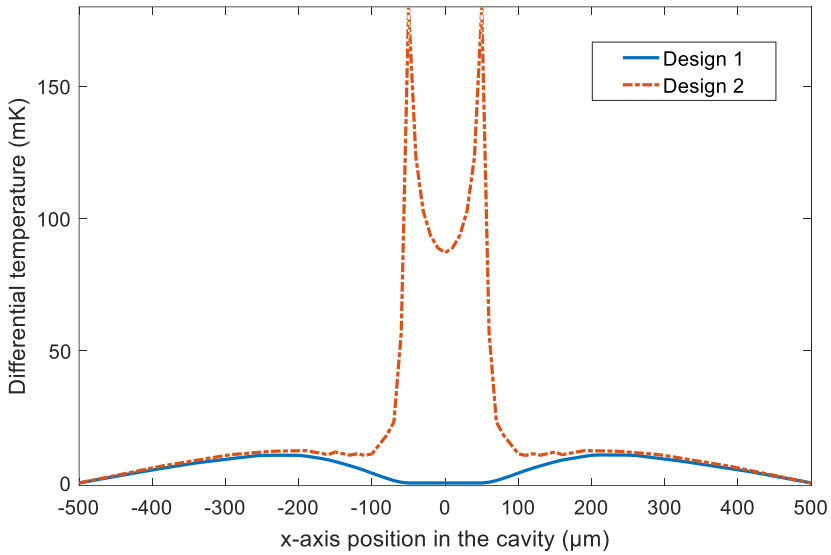

Figure 2.8. *Acceleration induced temperature variations along x-axis due to out-of-plane -1g acceleration.*

Figure 2.9 reports sensitivity for *Design 2* as a function of the distance between detectors and heater's edges.

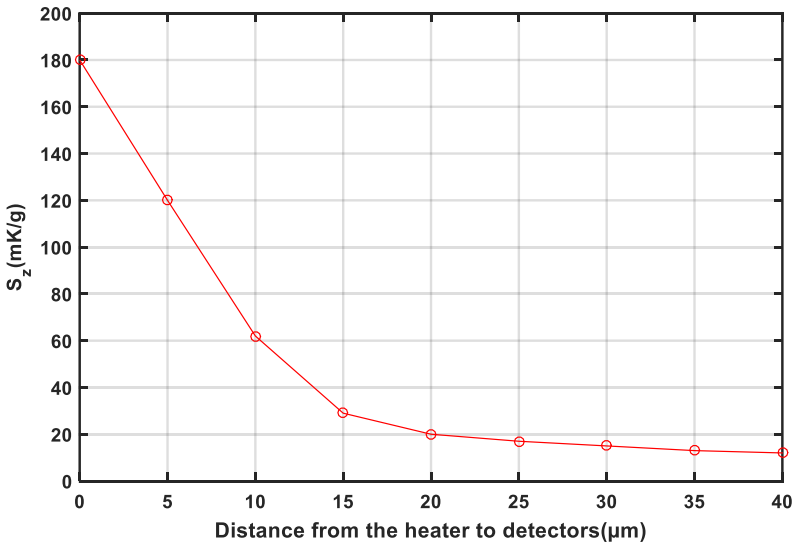

Figure 2.9. *Out-of-plane simulated sensitivity values as a function of the distance between detector and heater for Design 2.*

By comparing both designs, we notice that out-of-plane sensitivity of *Design 2* is about 5 times higher when detectors are located 10µm away from the heater's frame, and almost 3 times

higher for 15µm. It is therefore obvious that, for a convective accelerometer with a movable heater, z-axis detectors should be placed as close as possible to the heater to sense temperature variations induced by heater's movement.

From results presented in Figure 2.9, sensitivity reaches its highest value, 180mK/g, at the heater's boundaries. Sensitivity reaches 12 mK/g when the detectors are placed around 40 µm away from the heater, which is almost the same sensitivity given by the heater design with rigid beams (*Design 1*).

2.2.2.3 Sensitivity vs mass thickness

In this section, we propose to study the impact of an additional seismic mass above the heater on the out-of-plane sensitivity of the previously introduced *Design 3* device. Seismic mass is expected to increase heater's displacement for a given acceleration. Initially, heater's displacement under 1g acceleration is 34nm for flexible beams (*Design 2*). Simulations were performed after adding an *Au* seismic mass with different thicknesses to the simulated device. Temperature variations in the cavity of *Design3* are plotted for two different thicknesses due to a negative unity acceleration along z-axis in Figure 2.10.

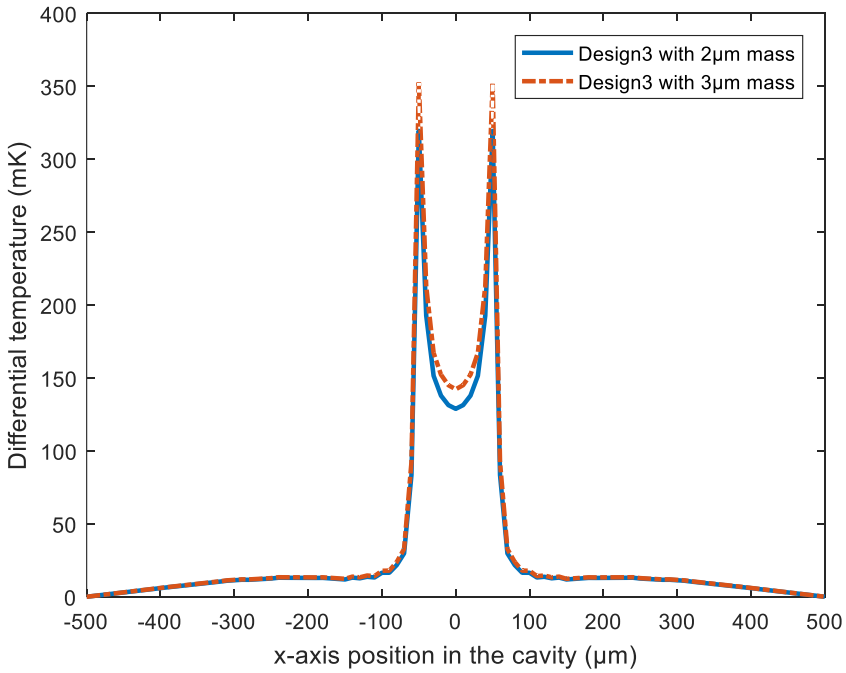

Figure 2.10. *Acceleration-induced temperature variations along x-axis for -1g z-axis acceleration for two different seismic mass thicknesses.*

Out-of-plane sensitivity values are extracted at 10 µm from the heater's edges and plotted in Figure 2.11. versus seismic mass thickness.

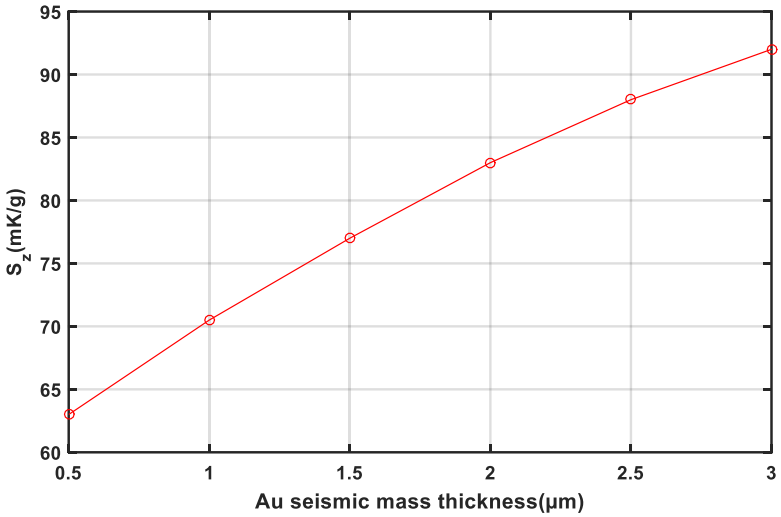

Figure 2.11. *Out-of-plane sensitivity of Design 3 vs mass thickness.*

Figure 2.11 shows that the out-of-plane sensitivity of *Design 3* increases almost linearly with thickness of an added seismic mass. By adding 3µm-thickness mass, 50% increase in sensitivity is observed. Although increasing the thickness of the seismic mass is beneficial in terms of out-of-plane sensitivity, implementing an additional material is not easy. *met2-met4* layers of the CMOS process can be easily used, but metal will only replace the oxide removed by planarization. Therefore, the thickness of the heater would remain the same and the expected result in terms of heater's mass is then less obvious.

2.2.3 Integration of mechanical solution in CMOS technology

2.2.3.1 Design rules and post-process specifications

To release the mechanical structure of a CMOS convective accelerometer, bulk micromachining using anisotropic wet etching of silicon is a convenient method due to its simplicity and cost-effectiveness. Wet etching using Tetramethylammonium hydroxide (TMAH) solution is a popular choice for its CMOS compatibility.

Wet etching is anisotropic, which means that the etch rate is different from one plane to another. While the etching rate of (100)-oriented Si wafer is the highest in the direction perpendicular to the (100) plane, it is very low with respect to the (111) plane, which makes it a virtual stopping wall for the etching process (Biswas, Kal, 2006). This property is very helpful

to obtain suspended structure oriented at 45°. A cross-section of etch profile obtained from anisotropic wet etching of a (100)-oriented Si substrate is presented in Figure 2.12.

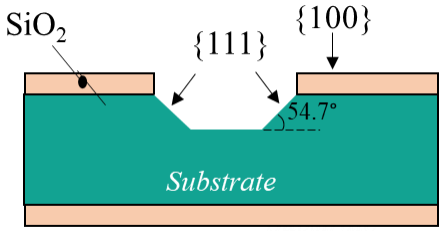

Figure 2.12. *Illustration of anisotropic wet etching profiles of a (100)-oriented silicon wafer.*

To guarantee the success of the micromachining post-process, several design rules must be followed. Some of these rules are limiting the design space of suspended structures. In the semi-industrial process that we are targeting, some important rules are:

- R_1: minimum width of a suspended microstructure is 25 µm.
- R_2: minimum distance between two microstructures is 35 µm.
- R_3: minimum enclosure of *Polysilicon* resistances into a structure is 4 µm.

Figure 2.13 presents an illustration of the design rules for suspended microstructure.

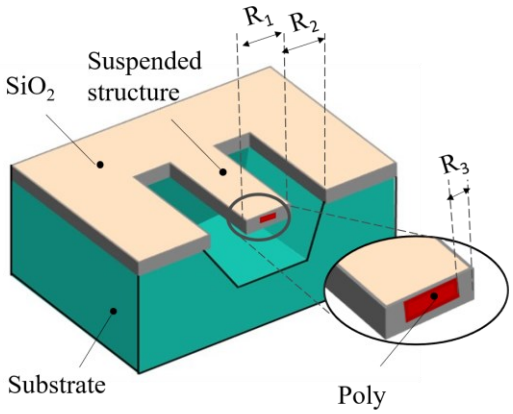

Figure 2.13. *Design rules for FSBM post-process bulk etching of an AMS C35 die.*

2.2.3.2 Design of detector's beams

Our aim in this study is to find a design of detector's beams that is suitable for anisotropic wet etching. The design should also be as compact as possible to maximize the space left for the heater's beams. As the latter will be placed in cavity's diagonals to benefit from higher

etching rates, detector's beams will be perpendicular to the cavity's boundaries, thus leading to slow etching. Therefore, etching simulations have been performed on different designs using Anisotropic Crystalline Etching Simulation (ACES) software, which estimates the etching time and profile during FSBM process (Zhu and Liu 2000).

A 25 µm–width straight beam geometry, presented in Figure 2.14 (a), was initially chosen to hold detectors in our structure. This simple geometry allows a large space to implement the zig-zag heater bridges. Due to the important length of the beam (450 µm) and the low etching rate (1µm/min) in the direction perpendicular to the (100) plane, an etching time of more than 7 hours would be required for a correct release. Immersing the structure in the etching solution all this time can damage the proximity electronics and etch the silicon underneath and on the edges of the substrate.

To decrease this etching time, a 45°-oriented V-shape structure is added to the beam, as shown in Figure 2.14 (b), to reduce its length and add a fast-etching profile geometry. The V-shape opening is released fast, therefore the beam will be attacked from 2 directions instead of 1, which will facilitate the etching process and help releasing the geometry faster than in the first design. However, even with this configuration, the etching stopping walls (111) still exist, so the etching can't be realized in a reasonable time because the beam is still too long. The next design, presented in Figure 2.14 (c), includes an additional diamond shape since the 45° orientation is needed for a faster etching process. With this last design, detector's beams can be released within 4 hours, which is a reasonable time for etching process.

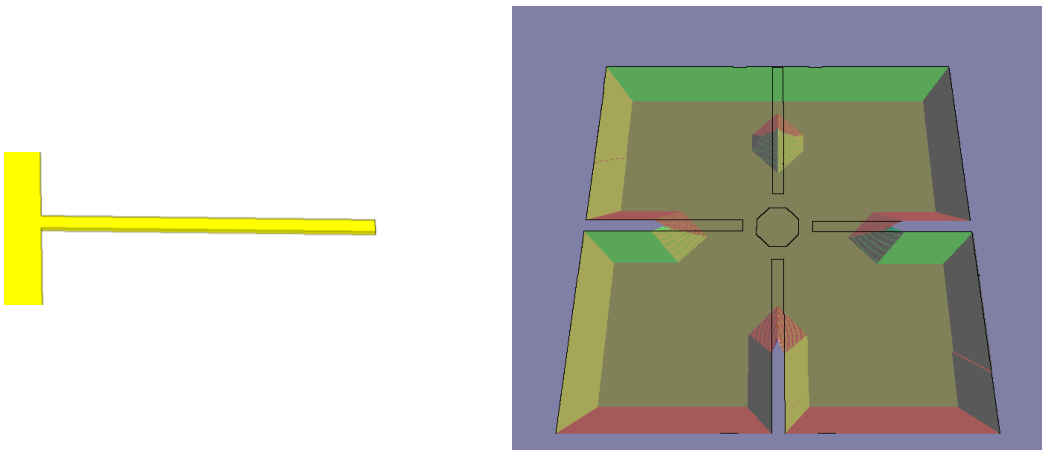

(a)

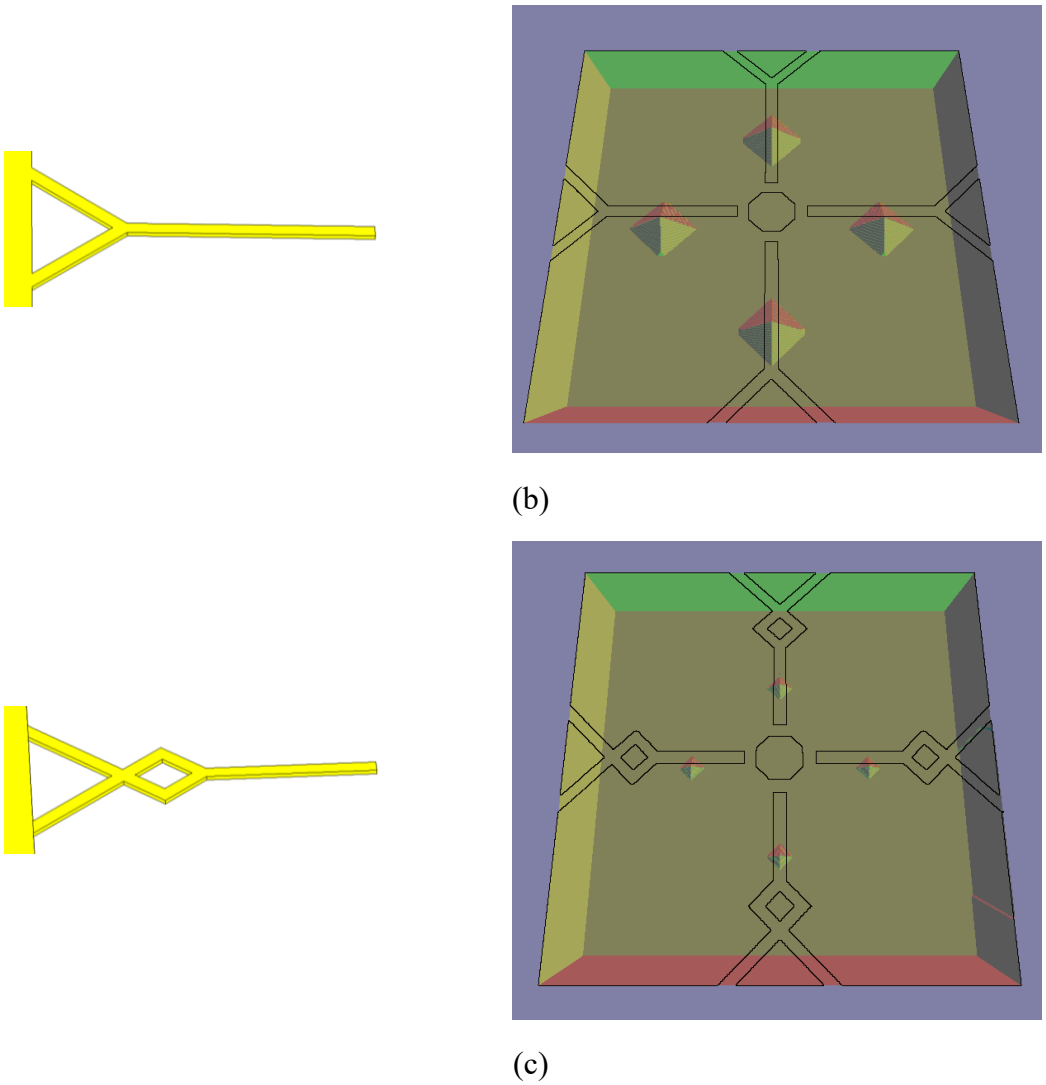

(b)

(c)

Figure 2.14. *ACES simulation of different detector's beams for an etching time of 4 hours.*

2.2.3.3 Design of a suspended heater with flexible beams

A 140 µm side-length heater plate was chosen since the larger the heater plate is, the larger the seismic mass may be embedded. Hexagonal shape has been preferred to reduce the time needed to release the heater's plate.

Flexibility of suspension bridges is maximized by a zig-zag structure. Using design rules R_1 and R_2, beam width is set to 25 µm, the number of turns of each beam is 15 and their total length is 2.4 mm. Figure 2.15 presents the design of the heater and its supporting zig-zag shaped beams.

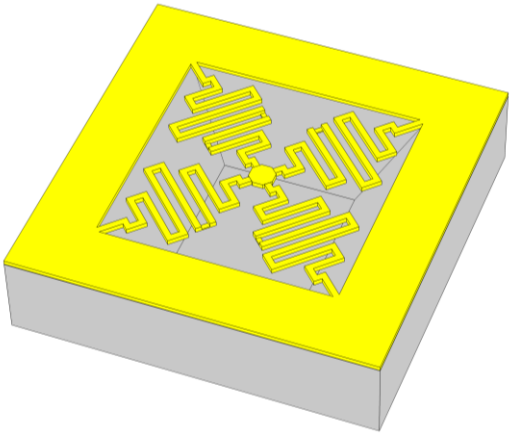

Figure 2.15. *Illustration of the proposed heater plate and its attachment beams.*

Etching simulations were done on the heater bridges using (100) oriented wafer with an etching rate of 1µm/min, a typical value found in the literature (Tabata, Asahi et al. 1992) with selectivity ratio of (111)/(100) = 0.033. Results, presented in Figure 2.16 , shows that the heater bridges are released in one hour. However, about 4 hours are required for heater's plate release. This etching time is still acceptable and is consistent with requirements to release detectors.

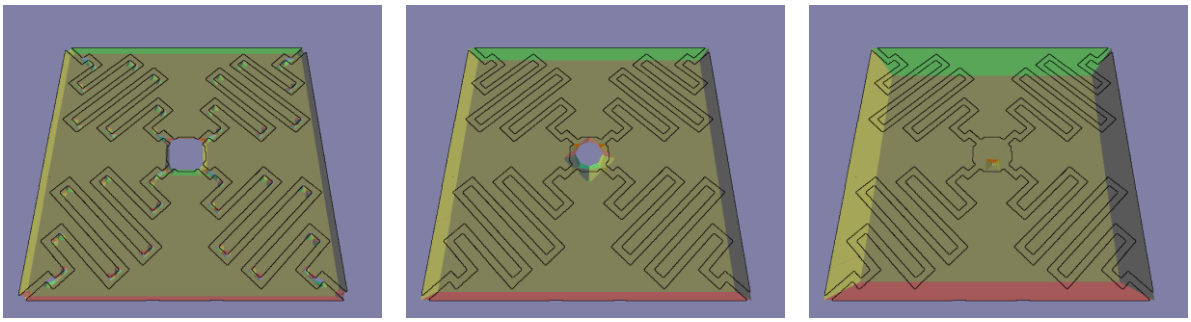

(a) (b) (c)

Figure 2.16. *Simulation of the heater and its flexible attachment beams within (a) 1hour, (b) 2 hours and (c) 4hours of etching time.*

Once geometry of the heater plate, its flexible suspended structure and the detector beams are defined with respect to both CMOS process and FSBM post-process, (Figure 2.17(a)), layout of the sensor is realized using Cadence© software as shown in Figure 2.17(b).

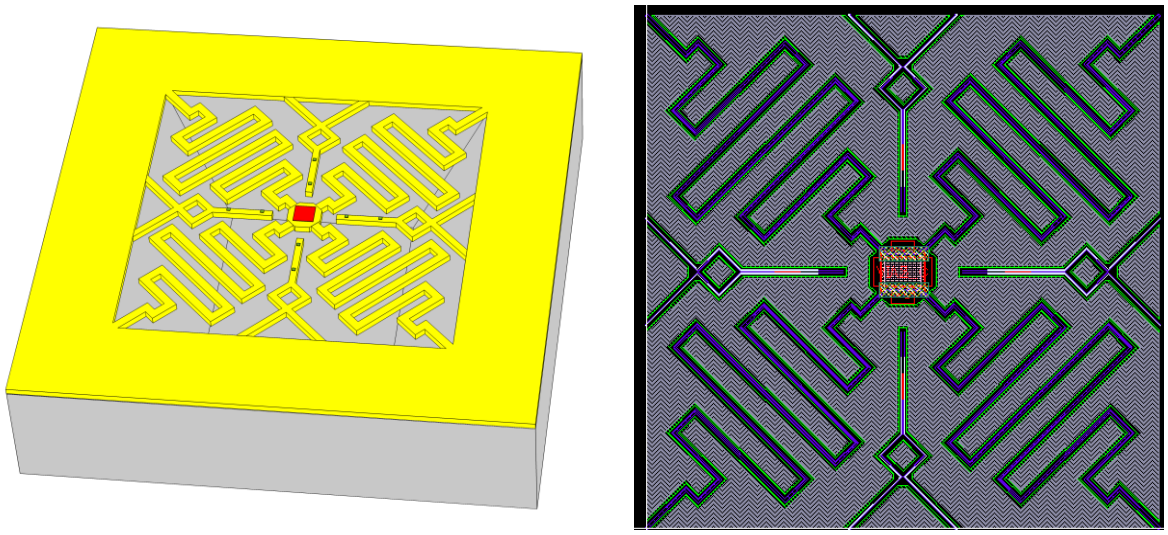

(a) *(b)*

Figure 2.17. *Designed 3-axis convective accelerometer with flexible heater : (a) artist view and (b) layout.*

2.2.3.4 Discussion and conclusion

While studying the 3-axis convective accelerometer with a moving heater, multiple limitations appeared. Initially, main condition to improve the out-of-plane sensitivity using a moving heater consists in measuring temperature as close as possible to the heater. From simulation results, it is clear that out-of-plane sensitivity is the highest at heater's edges and decreases with distance between heater and detectors. Unfortunately, design rules for successful FSBM etching of silicon imply, according to R_1, a minimum distance between two independent structures, i.e., heater and detector's bridge, of 35µm. Taking into account the minimum enclosure of polysilicon inside a released structure, R_3=4µm, the total distance between heater's boundaries and polysilicon temperature detectors is then about 40 µm. Sensitivity of such an accelerometer is then practically the same as sensitivity of a classical design. Therefore, our efforts have been focused on optimizing the State of the Art (SoA) design that will be described in next section.

2.3 Efficiency enhancement of SoA design

2.3.1 Numerical model development and validation

2.3.1.1 Numerical model development

As previously mentioned, a 3D model will be used. Usually, some geometry simplifications are applied to reduce simulation time. Main simplification generally consists in considering the heater as an SiO_2 heater plate with a fixed temperature applied on its sides as a boundary condition. In this study, heater will be modeled to take into account heat losses and heat exchanges, including heat losses along connection wires and embedded resistances to increase accuracy. With respect to the SoA design (Nguyen, 2013, Mailly, Nguyen et al. 2014), heating resistance is made of *Highly Resistive Polysilicon* (PolyH) and biased with a DC current through two *Aluminum* (Met1) wires. Heating resistances is embedded inside an SiO_2 heater plate as illustrated in Figure 2.18.

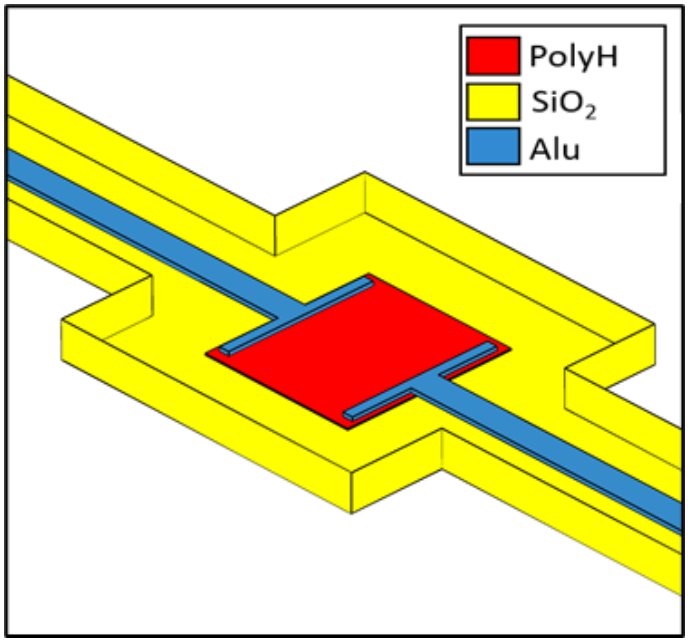

Figure 2.18. *Heater model and corresponding layers.*

Material properties are set according to AMS foundry specifications for this CMOS 0.35µm technology to properly model heat transfer. Table 2.2 presents material properties for heating resistance and connecting wires, which include linear and quadratic temperature coefficients TC_i and sheet resistance $R_{\square}$. In addition, width and position of each layer are defined with respect to the technology. Thickness of the suspended structure is set to 6µm.

Table 2.2. *Properties of heater active materials.*

Material	PolyH	Met1 Aluminum
TC_1 (K^{-1})	$-0.75'10^{-3}$	$3.3'10^{-3}$
TC_2 (K^{-2})	$3.82'10^{-6}$	0
$R_{\square}$ (Ω/□)	$120'10^{-3}$	$120'10^{-3}$

Physics modules used for the proposed 3D model include *Joule Heating* to transform electrical energy into heat when applying an electrical voltage between both extremities of aluminum connecting wires. *Heat Transfer* is also used to model thermal distribution within the cavity, heat transfer from heating resistance to SiO_2 frame, suspension beams and surrounding air. To model air convection induced by an acceleration, *laminar flow* module is added to model acceleration effect by applying a volumic force on fluid enclosed within the cavity.

The whole structure, including the top and bottom cavities, is considered as a closed volume of air at atmospheric pressure. The air is modeled as a compressible and non-turbulent fluid and its properties are temperature dependent. Cavity walls are assumed to be isothermal boundaries with a fixed ambient temperature of 300 K. Finally, meshing of the model is refined till sensitivity converges to a quasi-constant value independently of the number of meshes to obtain a good trade-off between accuracy and simulation time. Based on this modeling effort, and using the developed 3D model, we will now assess accuracy with respect to silicon.

2.3.1.2 Numerical model validation

In this section, accuracy of the developed model is verified with respect to experimental results obtained with an SoA accelerometer for different heating power as reported in the literature (Mailly, Nguyen et al. 2014).

Simulated temperature variations along the x-axis, induced by an in-plane acceleration towards the right, are presented in Figure 2.19 for various heating temperatures. It is first observed that the actual detectors' location of the tested device, i.e., about 250µm away from the cavity center, does not correspond to the maximum sensitivity that is obtained far closer to the center of the cavity. As previously explained, this was a consequence of using a 2D model for the design of this device.

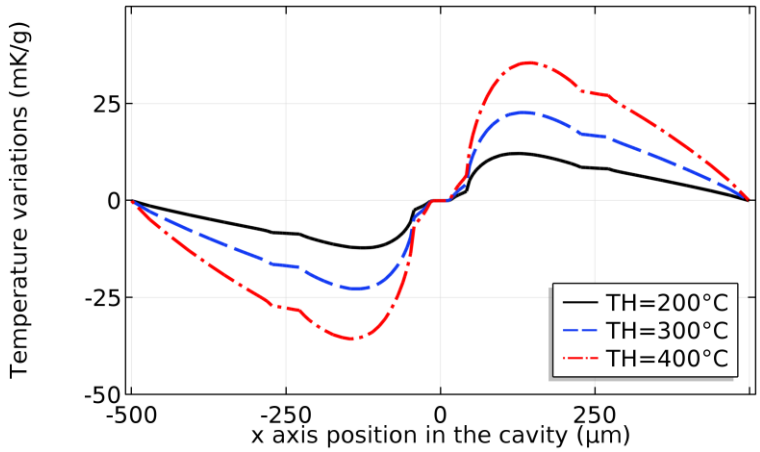

Figure 2.19. *Simulated temperature variations along the x axis of an SoA accelerometer for different heating temperatures in presence of an in-plane accelerations towards the right.*

Table 2.3. *Comparison between experimental and simulated in-plane sensitivities using the proposed 3D FEM model versus heating temperature and power consumption.*

T(°C)	***P(mW)***	***S_xExp(mK/g) (Mailly, Nguyen et al. 2014)***	***S_xSim(mK/g)***	***Error***
200	3.6	15	16.8	+12%
250	4.7	22	25.5	+16%
300	5.9	29	33.8	+16.5%
350	7.1	36	42	+17%
400	8.3	47	55	+17%

Sensitivities obtained from 3D simulations with detectors located 250 µm away from the cavity center, $S_{x,y}Sim$, are then compared with experimental sensitivities, $S_{x,y}Exp$, in Table 2.3 and plotted in Figure 2.20. Even if an overestimation up to 17% remains, this is a huge improvement with respect to a 2D model as estimated sensitivity was four times higher than reality (Nguyen, 2013). Residual overestimation might result from neglecting radiative heat losses in our 3D model. This simplification is impacting results more and more significantly when temperature increases. Overall, we can consider our 3D model acceptable to drive design of an optimized device as explained in (Oberkampf and Barone 2006). This device optimization is presented in the next section.

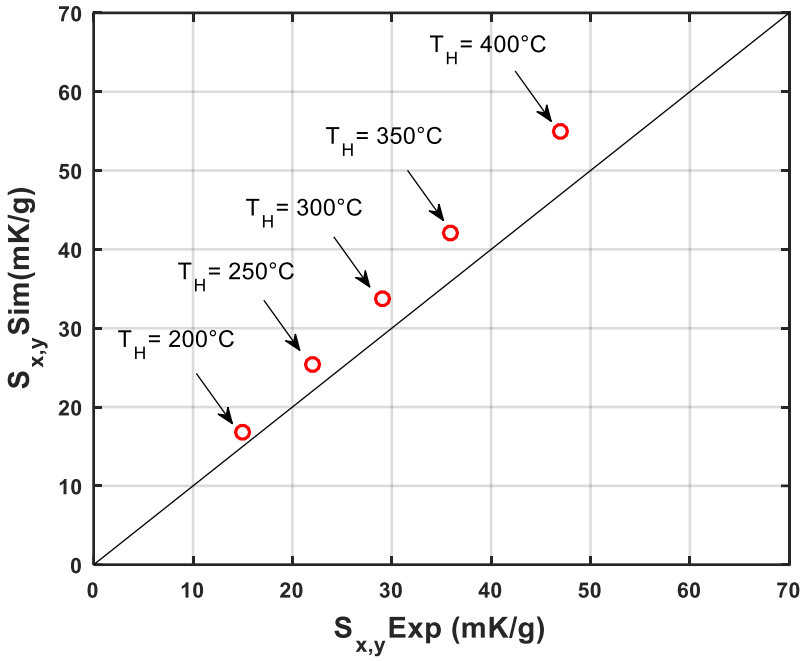

Figure 2.20. *Simulated in-plane sensitivities versus experimental sensitivities for different heater temperatures.*

2.3.2 Design of an efficient heater shape

Based on the previously validated 3D model, we will study in this section the effect of heater size and shape on accelerometer performances. Sensitivity is strongly dependent on the shape and size of the heater, as both design parameters have a strong impact on both convection and heat transfer (Mezghani, Tounsi et al. 2012, Mezghani, Tounsi et al. 2013). The purpose is then to select shape and size of a heater that improves sensor sensitivity in all three axis.

To maintain high temperatures of the fluid, reported convective accelerometers require generally high heating power (Luo, Yang et al. 2001, Courteaud, Crespy et al. 2008, Garraud, Combette et al. 2012). It is then crucial to consider power consumption and, therefore, to find a trade-off between sensor sensitivity and power consumed in the heater. For this purpose, the ratio between sensitivity and power consumption is set as a figure of merit to evaluate energy-efficiency of studied solutions.

2.3.2.1 Overview of studied heater designs

Four heater designs, compatible with a 0.35µm CMOS technology and FSBM post-process, have been studied.

The *Square60* heater design is a simple 45°-oriented square plate with 60µm side length attached by four bridges. The side length is increased to 100µm in the *Square100* heater design. This is the largest heater size fabricated using CMOS technology and FSBM post-process found in literature (Garraud, Giani et al. 2011), probably because larger heater would be too long to etch. Figure 2.21 (a) presents the implementation of *Square60* and *Square100* designs.

The *Quadruple* design, presented in Figure 2.21 (b), proposes replacing the single heating resistance in the *Square100* heater plate by 4 micro-resistances implemented at the heater corners for symmetrical heat distribution all over the structure. These heating resistances are square shaped and connected in a parallel configuration.

Figure 2.21 (c) presents the *Wings* heater design, in which the heater plate is extended to 150µm, and perforated in the center by a 100µm-wide opening in order to facilitate post-CMOS etching. Same micro-resistances as used in the *Quadruple* heater, are placed outside the perforated plate in four wings located in each corner of the heater.

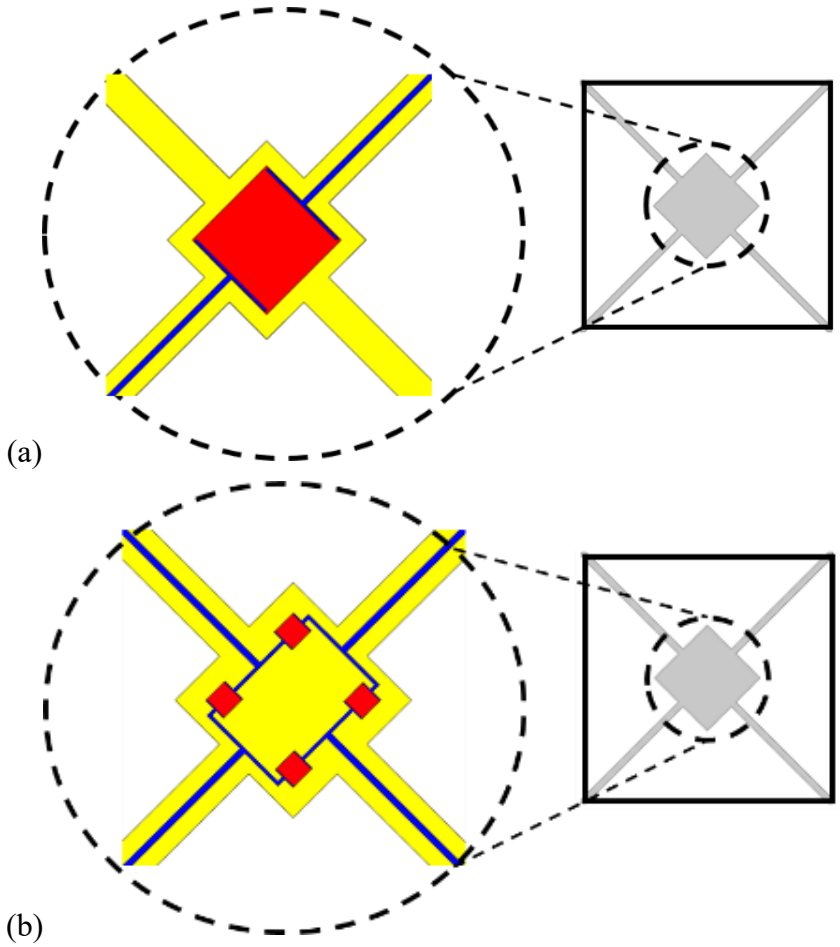

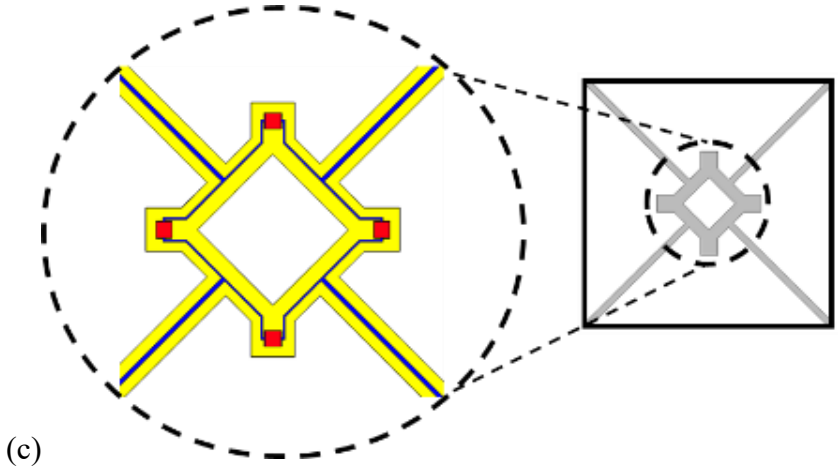

(c)

Figure 2.21. *Proposed design details of studied heaters (a) Square60 and Square100, (b) Quadruple, and (c) Wings.*

2.3.2.2 Performance assessment at low heating power

One of the simplest ways to improve sensitivity of convective accelerometers is to increase heater's size to expand the surrounding volume of heated air, which enlarges isotherms and impacts positively air convection in the cavity. This effect can be observed on isotherms of *Square100* that are slightly wider than of *Square60*, Figure 2.22 (a) and (b). However, increasing the size of heating resistance requires more power to maintain an identical temperature. Therefore, for a given power consumption, temperature decreases with the inverse of heater's size: comparing again *Square60* with *Square100* heaters, maximum heating temperature decreases from 580K for *Square60* heater down to 510K in *Square100* heater for a dissipated power of 7mW. Similar maximum temperatures, i.e., 500K, are observed for *Quadruple* design, Figure 2.22 (c), and *Wings* design, Figure 2.22 (d), that are both larger than *Square60*.

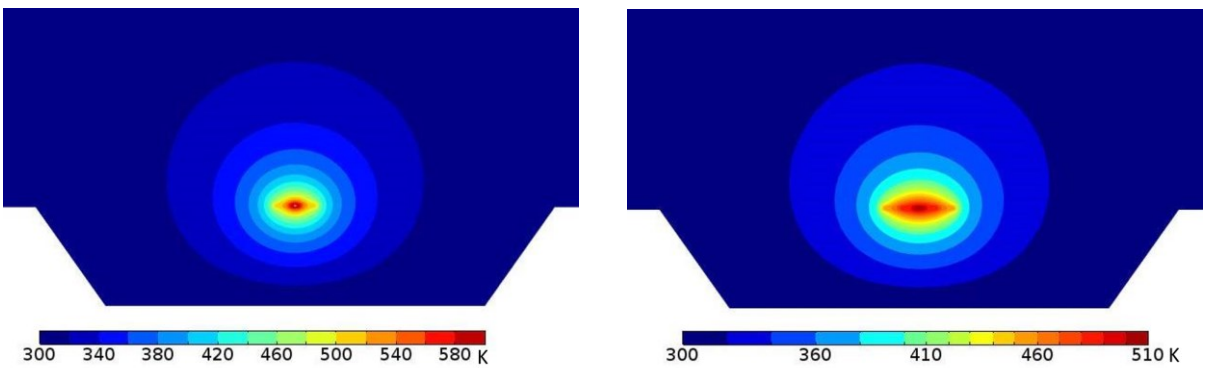

(a) (b)

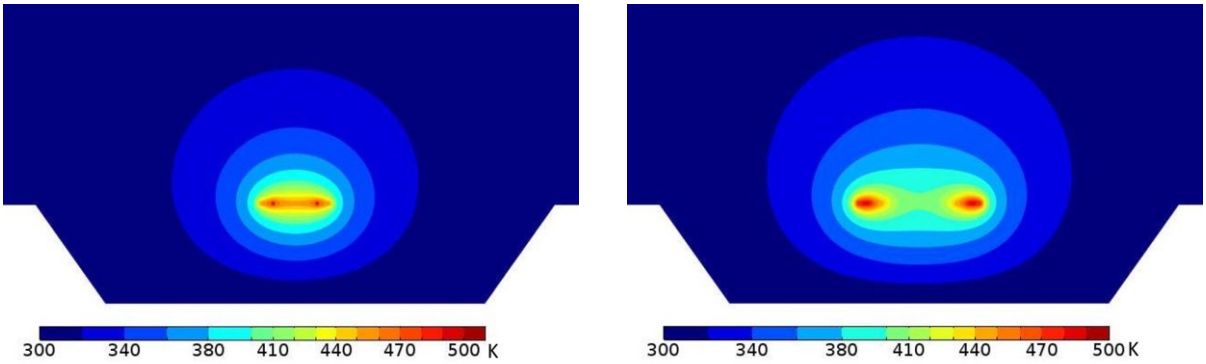

(c) (d)

Figure 2.22. *Generated isotherms in the cavity under an input power of 7mW by various heaters (a) Square60, (b) Square100, (c) Quadruple, and (d) Wings.*

However, maximum temperature is not the leading parameter affecting sensitivity. This is demonstrated in Table 2.4. that reports complete simulation results for the four studied heaters with identical power dissipation. For each heater, average temperature, in-plane and out-of-plane sensitivities and corresponding efficiency are listed. Obviously, sensitivities are determined for an optimal positioning of detectors.

Table 2.4. *Average heater temperature, in-plane and out-of-plane sensitivities and efficiencies for studied heaters at same heating power of 7 mW.*

	$T_{H\,avg}(K)$	*Sx (mK/g)*	$E_x(mK/g/mW)$	*Sz (mK/g)*	$E_z(mK/g/mW)$
Square60	560	50	7.1	2.7	0.39
Square100	503	56	8	3.9	0.56
Quadruple	512	48	6.9	3.2	0.46
Wings	482	70	10	5.5	0.79

It is clearly established that despite a lower average temperature with respect to its counterparts, *Wings* design allows the highest sensitivities for both in-plane and out-of-plane accelerations. Obviously, efficiency is also higher for this design. When four microheaters are used (*Quadruple* design), heat distribution in the cavity is modified and the hot bubble becomes

flatter as illustrated in Figure 2.22 (c). However, despite this temperature redistribution, sensitivities of the *Quadruple* design are lower than those of *Square100*.

Finally, for the *Wings* design, it is clear from Figure 2.22 (d) that increasing the size of the heater enlarges the hot bubble. Maximum temperature is obtained where heating resistors are located. The key point for this heater is that the hollow plate strongly reduce conduction in the plate thus leading to four independent hot point, each one being in front of a detector. Therefore, for the same power consumption than *Quadruple* and *Square100* designs, same heating temperature is obtained despite a larger size. Advantages of a center-opening in the heater is then two-fold. On the one hand, it allows to enlarge the heater without increasing post-process releasing time and, on the other hand, it moves the central hot point and splits it in four deported ones located closer to detectors.

2.3.2.3 Performance assessment at maximum heating power

Temperature variations along the cavity at maximum heating power (i.e., for the highest possible bias voltage 3,3V or for the highest tolerated heating temperature 700K), under in-plane and out-of-plane accelerations are presented in Figure 2.23 (a) and (b), respectively.

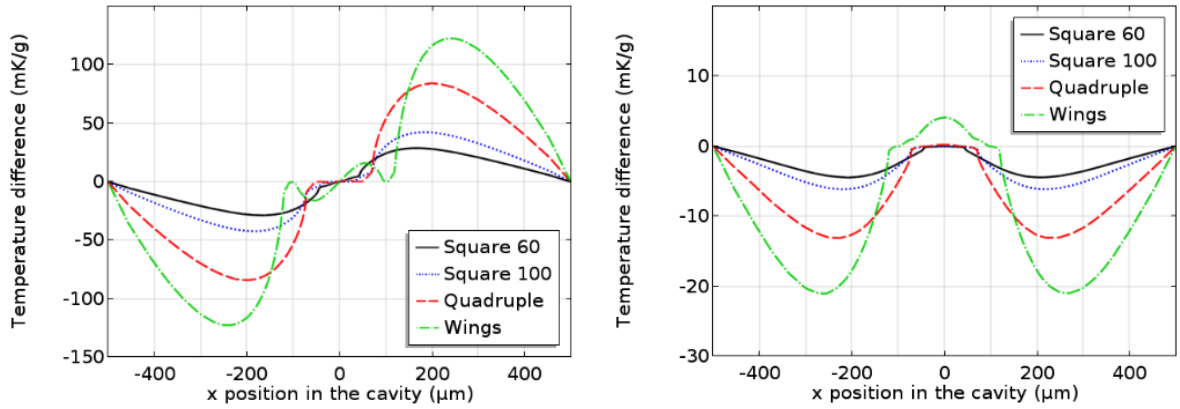

(a) (b)

Figure 2.23. *Temperature variations in the cavity for studied heaters under 1g (a) in-plane and (b) out-of-plane accelerations at maximum power dissipation.*

Considering the optimal location of temperature detectors for each heater design, corresponding maximum sensitivities, in mK/g, are given in Table 2.5. Sensitivities have then been normalized to the one of *Square60* and reported in Figure 2.24 (a). By dividing sensitivity by the dissipated power, efficiency can be similarly reported in Figure 2.24 (b).

Table 2.5. *In-plane and out-of-plane maximum sensitivities obtained with different heaters for their maximum heating power.*

	P_{max}(mW)	T(K)	V_{heater} (V)	Sx (mK/g)	Sz (mK/g)
Square60	8	592	3.3	62	4.5
Square100	9	555	3.3	85	6.2
Quadruple	14	700	2.44	171	13
Wings	17	700	2.6	246	21

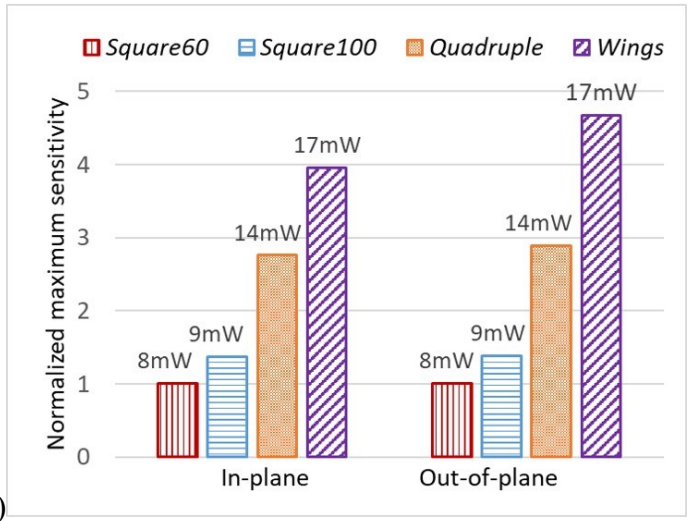

(a)

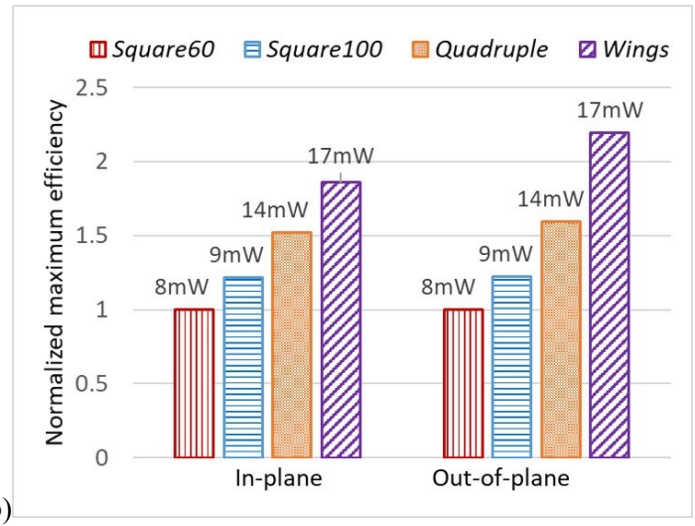

(b)

Figure 2.24. *Comparison between the four proposed heaters for in-plane and out-of-plane accelerations in terms of (a) maximum sensitivity and (b) maximum efficiency. Data are normalized to 1 for the Square60 heater.*

This confirms the results of the constant power study of the previous section and demonstrates that *Wings* heater exhibits the highest maximum sensitivity but also the highest energy-efficiency. This is then a promising shape of heater to increase performances of the SoA 3-axis accelerometer.

Conclusion

In this chapter, two solutions for sensitivity improvement of a 3-axis convective accelerometer have been studied.

The first solution is based on a mechanical modification of the heater suspension bridges to build an accelerometer cumulating convective transduction and proof-mass displacement. Simulations predict a significant increase of out-of-plane sensitivity. However, practical implementation was found to be impossible with respect to FSBM post-process design rules.

The second solution is based on revisiting heater shape and size to improve both in-plane and out-of-plane sensitivities with a good energy-efficiency. A new heater shape, namely *Wings*, was found to reduce maximum temperature, to increase not only sensitivities but also the ratio between sensitivity and power consumption. It is based on a larger plate with a large opening in the middle and four un-centered heating resistors. This solution appears to be compatible with a 0.35µm CMOS technology and a FSBM post-process. This heater will then be extensively studied in next chapter to design and to optimize the SoA 3-axis convective accelerometer.

REFERENCES

Baglio S., Castorina S., Fortuna L., Savalli N., « Modeling and design of novel photo-thermo-mechanical microactuators », *Sensors and Actuators A: Physical*, vol. 101, n° 1-2, 2002, p. 185-193.

Biswas K., Kal S., « Etch characteristics of KOH, TMAH and dual doped TMAH for bulk micromachining of silicon », *Microelectronics Journal*, vol. 37, n°6, 2006, p. 519-525.

Chaehoi A., Conception et Modélisation de MEMS monolithique CMOS en technologie FSBM: Application aux accéléromètres, Thèse de doctorat, Université Montpellier II-Sciences et Techniques du Languedoc, 2005.

Courteaud J., Crespy N., Combette P., Sorli B., Giani A., « Studies and optimization of the frequency response of a micromachined thermal accelerometer », *Sensors and Actuators A: Physical,* vol. 147, n° 1, 2008, p. 75-82.

Garraud A., Combette P., Deblonde A., Loisel P., Giani A., « Closed-loop micromachined accelerometer based on thermal convection », *Micro & Nano Letters,* vol. 7, n° 11, 2012, p. 1092-1093.

Garraud A., Giani A., Combette P., Charlot B., Richard M., « A dual axis CMOS micromachined convective thermal accelerometer », *Sensors and Actuators A: Physical*, vol. 170, n° 1-2, 2011, p. 44-50.

Luo XB., Yang YJ., Zheng F., Li ZX., Guo ZY., « An optimized micromachined convective accelerometer with no proof mass », *Journal of Micromechanics and Microengineering*, vol. 11, n° 5, 2001, p. 504.

Mailly F., Nguyen H.B., Latorre L., Nouet P., « CMOS implementation of a 3-axis thermal convective accelerometer», *IEEE Sensors*, 2014, p. 1471-1474.

Mezghani B., Tounsi F., Masmoudi M., Rekik AA., Mailly F., Nouet P., « Efficiency modeling of a CMOS MEMS convective accelerometer », *7th International Conference on Design & Technology of Integrated Systems in Nanoscale Era*, 2012, p. 1-5.

Mezghani B., Tounsi F., Rekik AA., Mailly F., Masmoudi M., Nouet P., « Sensitivity and power modeling of CMOS MEMS single axis convective accelerometers », *Microelectronics Journal*, vol. 44, n° 12, 2013, p. 1092-1098.

Nguyen HB., Conception et réalisation d'un accéléromètre convectif 3-axes en technologie CMOS, Thèse de doctorat, Montpellier 2, 2013.

Oberkampf W.L., Barone. M.F. « Measures of agreement between computation and experiment: Validation metrics », *Journal of Computational Physics*, vol. 217 n° 1, 2006, p. 5–36.

Tabata O., Asahi R., et al. «Anisotropic etching of silicon in TMAH solutions. » *Sensors and Actuators A: Physical*, vol.34, n° 1, 1992, p. 51-57.

Zhu Z., Liu C., « Anisotropic crystalline etching simulation using a continuous cellular automata algorithm », *Computer Modeling Engineering Sciences*, vol. 1, n° 1, 2000, p. 11-19.

Chapter 3: Development of a new 3-axis CMOS MEMS convective accelerometer with high energy-efficiency

Introduction

In this chapter, we will investigate the design of an energy-efficient convective accelerometer based on the original wing-shaped heater proposed in previous chapter.

Heater's geometry will be first optimized for the best energy-efficiency in all three sensitive axis. Then, optimal detector's position will be defined and geometry of the detector's supporting bridges will be optimized. Optimization will be carried out with respect to design rules of a 0.35µm CMOS technology associated to a Front-Side-Bulk-Micromachining (FSBM) post-process. Expected performance of the so-obtained sensor will then be accessed followed by describing CMOS readout circuit.

3.1 Geometry optimization of the new heater

3.1.1 Technological considerations

Geometrical parameters of the selected heater shape (i.e., *Wings*) are studied and optimized to further improve the expected performance. Both general and close-up views of the *Wings* heater are illustrated in Figure 3.1(a) and (b), respectively. Initial values for geometrical parameters are listed in Table 3.1. These initial values are set to the minimum allowed by fabrication technology except for *b*, *c* and *d* that are arbitrary set.

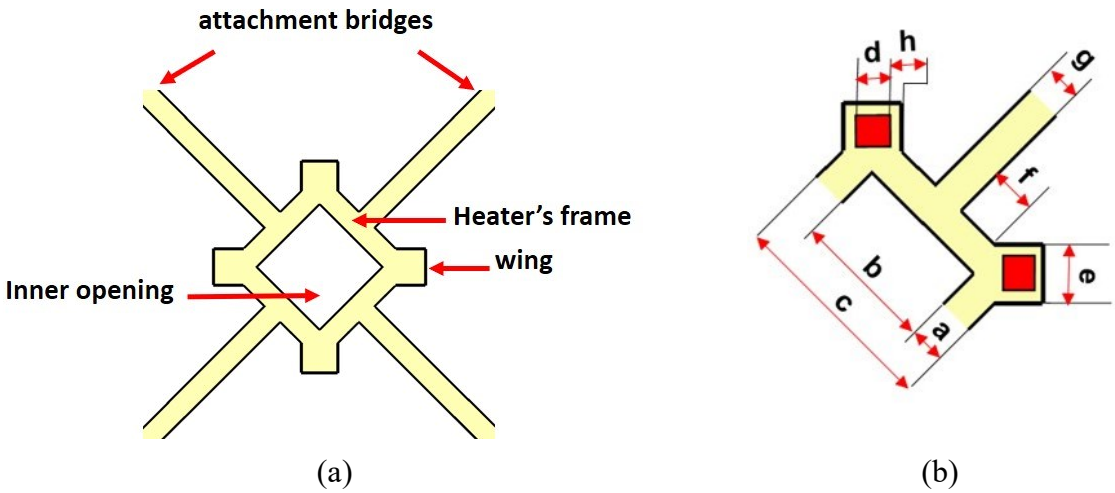

Figure 3.1. *(a) General and (b) close-up view of the proposed heater and its four attachment bridges with their main geometrical parameters.*

Table 3.1. *List of main dimensions of the selected heater and initial values*

Symbol	Description	Value	Unit
a	Width of the heater frame linking the four micro-heaters	25	µm
b	Inner side length of the heater frame (inner opening)	100	µm
c	Side length of the heater frame	150	µm
d	Side length of the square heating resistance	15	µm
e	Side length of the heating wing	41	µm
f	Distance between the heating wing and its attachment bridge	35	µm
g	Width of the attachment bridge	25	µm
h	Width of the SiO_2 enclosure around the heating resistance	13	µm

3.1.2 Optimization of the heater frame's width

The first design parameter to be optimized is *a,* the width of the square-shaped frame that connects the four wings together. Different values for beam width *a* were applied while keeping all other parameters to their nominal values of Table 3.1.

Simulations were performed with different values of *a* ranging from 25 up to 57µm. In-plane and out-of-plane sensitivities and corresponding efficiencies are reported with respect to *a* in Figure 3.2 and Figure 3.3, respectively. It is shown that in-plane sensitivity drops from 246mK/g for *a*= 25µm down to 206mK/g for *a*= 57µm. Accordingly, in-plane efficiency also decreases from 14.5mK/g/mW to 12mK/g/mW. For out-of-plane accelerations, sensitivity drops from 21 mK/g for *a*=25µm down to 18 mK/g for *a*=57µm. Accordingly, out-of-plane efficiency also decreases from 1.23mK/g/mW to 1.05mK/g/mW. As a conclusion, the lower is the width of the heater frame *a*, the higher the sensitivity.

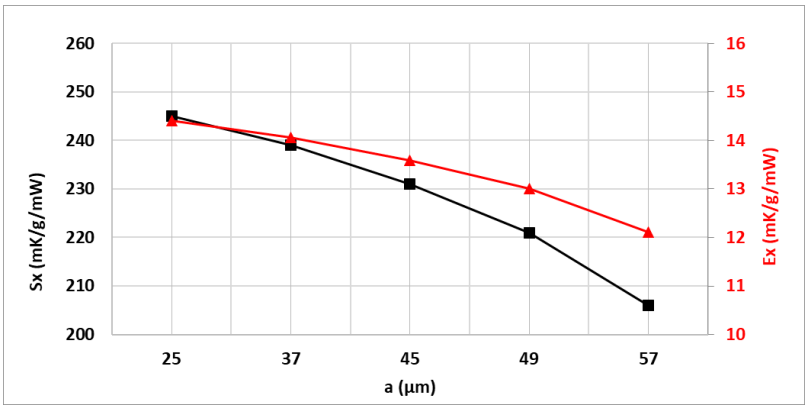

Figure 3.2. *In-plane sensitivities and corresponding efficiencies obtained for different frame widths and a heating power of 17 mW.*

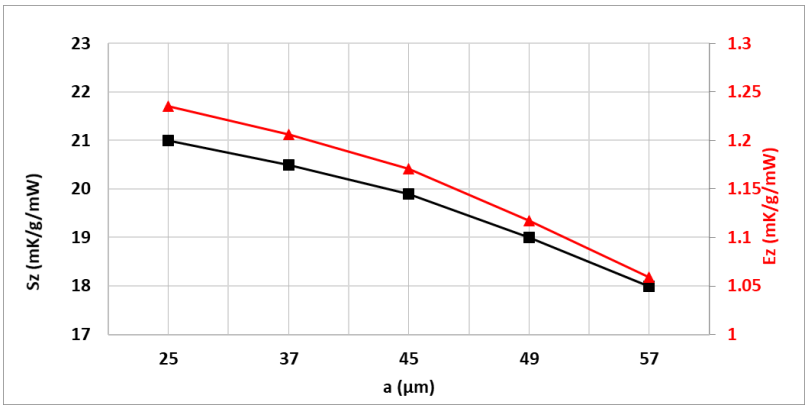

Figure 3.3. *Out-of-plane sensitivities and corresponding efficiencies obtained for different frame widths and a heating power of 17 mW.*

As a physical explanation, it appears that increasing frame's width *a* increases both the SiO_2 beam section and the frame surface. Therefore, heat conduction through the frame and more importantly heat losses by convection are both increased. As a result, both sensitivity and efficiency degrade.

Since minimizing SiO_2 cross section and exchange area results in better sensitivity and efficiency of the heater, some other parameters, namely *d*, *e*, *f*, *g* and *h*, will be kept to their minimum values as mentioned in Table 3.1 without any additional demonstration.

3.1.3 Optimization of the size of the heater's wings

The next design parameter to be optimized is the side length of the square heating resistance, *d*. This parameter directly impacts wing size *e,* side length of the heater frame *b* and side length of the inner opening *c* as reported in Table 3.2. We have then defined a design space varying from 5 up to 45µm for *d*. The so-obtained values for *b*, *c* and *e* are then calculated and reported, in Table 3.2, to minimize SiO_2 cross section, heat conduction and heat exchange surface.

Table 3.2. *Possible geometrical parameters for the heater as a function of d.*

Parameters	**Optimal values (µm)**			
d	5	15	25	45
$e= d+2h$	31	41	51	71
$c= g+2f+\sqrt{2}e$	139	153	167	196
$b=c-a$	89	103	117	146

With $a = g = 25$ µm, $f = 35$ µm and $h = 13$ µm set to their minimum due to *FSBM* post-process design rules.

Simulations of the accelerometer with different heater parameters are performed for 15mW heating power and the so-obtained temperature variations for in-plane and out-of-plane accelerations are presented in Figure 3.4(a) and (b). From these graphs, in-plane and out-of-plane sensitivities are extracted at the position giving the maximum temperature variation. These sensitivities are then plotted versus *d* in Figure 3.5 and Figure 3.6, respectively.

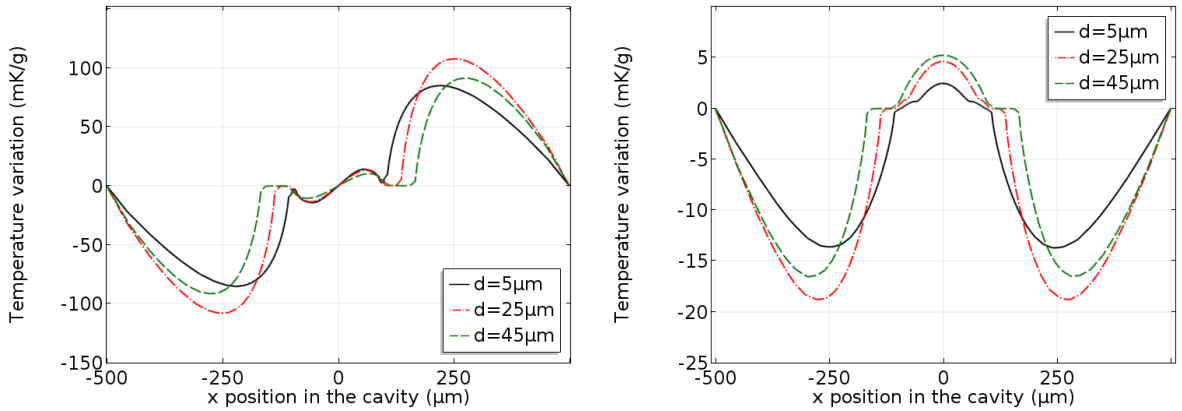

Figure 3.4. *Acceleration-induced temperature variations, in the detector's line, for a heating power of 15 mW and for (a) in-plane and (b) out-of-plane accelerations of 1g.*

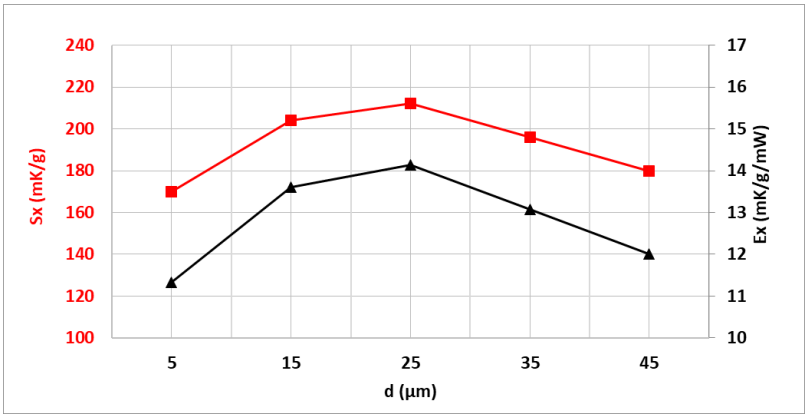

Figure 3.5. *In-plane sensitivities and corresponding efficiencies for different heating resistance side lengths and a heating power of 15 mW.*

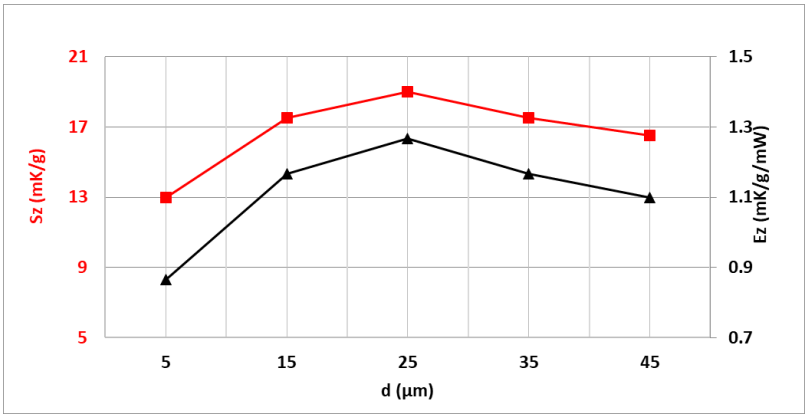

Figure 3.6. *Out-of-plane sensitivities and corresponding efficiencies for different heating resistance side lengths and a heating power of 15 mW.*

From the above results, sensitivity as a function of *d* behaves as follow:

- For low values of *d*, both in-plane and out-of-plane sensitivities are low.
- Sensitivities then increase with *d* to reach 218 mK/g for in-plane accelerations and 19 mK/g for out-of-plane accelerations at *d*=25µm.
- Further increase of *d* above 25 µm reduces sensitivity.

For physical understanding of the above results, isotherms generated by a heating power of 7mW without acceleration are illustrated in Figure 3.7(a), (b) and (c) for *d* equals to 5, 25 µm and 45µm, respectively.

For *d*=5µm, power is dissipated in a so small volume that heat exchange leads to a very small hot isotherm and poor convection mechanisms. The hot spot is at high temperature, but sensitivity is low due to the small size of the hot bubble, which largely affects the sensitivity (Mezghani, Tounsi et al. 2013).

For *d*=45µm, power is dissipated in a large volume while the so-obtained maximum temperature is low as the sensitivity and thus the efficiency. It can be easily understood that a large hot spot with a low temperature will minimize convection.

Finally, it is observed that there is an optimum size for the heater's resistors, around *d*=25 µm, that leads to a large size of the hot spot isotherms and a high temperature. This behavior is observed because we are comparing heaters with the same power dissipation to consider energy efficiency. From this study, we are now able to design an energy-efficient heater and next section will investigate temperature detection.

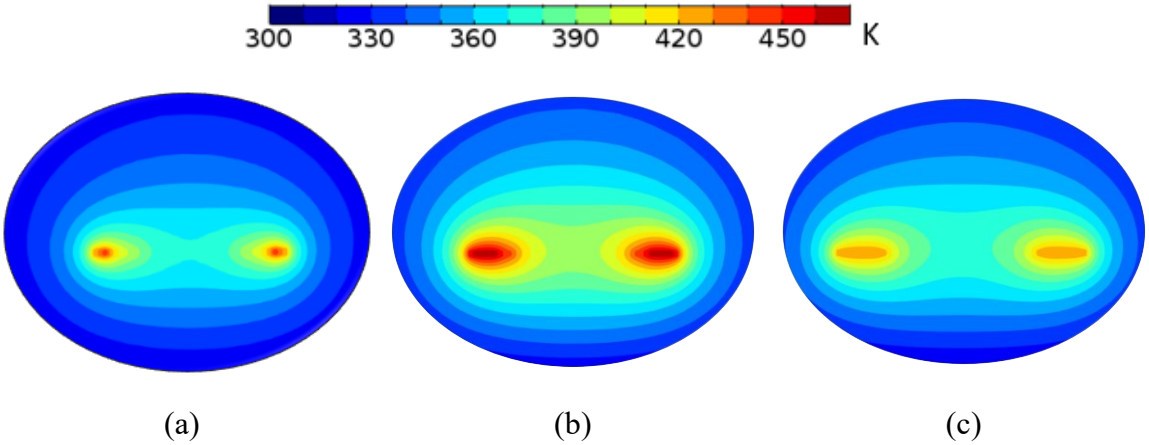

Figure 3.7. *(xOz) cross section of the hot bubble generated by the micro-heater with a resistance size of (a) 5 µm, (b) 25 µm and (b) 45 µm.*

3.2 Temperature detectors to optimize energy-efficiency

3.2.1 Investigation of optimal detector position

In this section, we investigate locations of maximum temperature variations, where in-plane and out-of-plane detectors should be located. FEM simulations have been performed with the optimal dimensions of the heater to analyze temperature variations due to acceleration. Figure 3.8 reports temperature variations in the detectors' plane versus distance to the center of a 1mm cavity for a 1g acceleration.

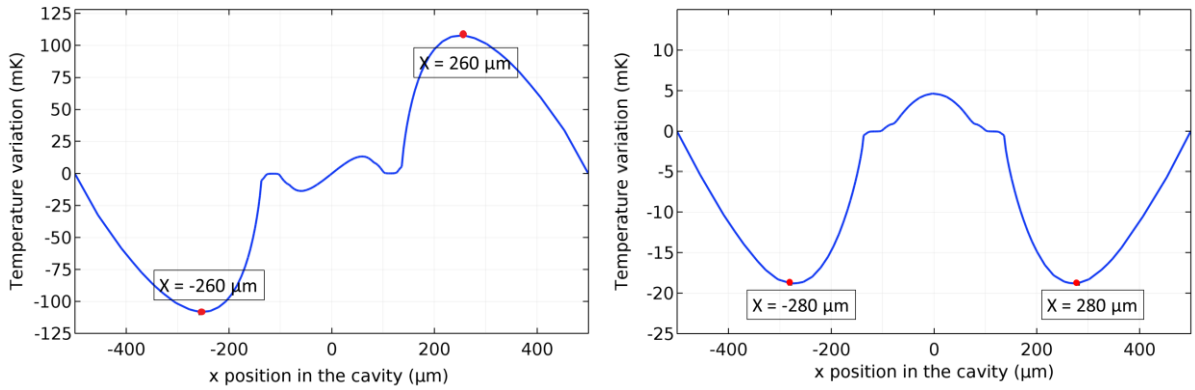

(a) *(b)*

Figure 3.8. *Temperature variation in the cavity and corresponding maximum sensitivity locations for unity (a) in-plane and (b) out-of-plane accelerations at 15mW.*

It comes that optimal detector location for in-plane acceleration, Figure 3.8(a), corresponding to the maximum temperature variation is 260 µm from the cavity center. At this position, sensitivity is 218 mK/g. For an out-of-plane acceleration, Figure 3.8(b), temperature variation profile shows a small shift in the detectors' optimal position and maximum temperature variation is found, 20 µm closer to the cavity edge, at 280 µm where a sensitivity of 19 µm/g is obtained.

To summarize, Figure 3.9 illustrates the optimal location of the required temperature detectors inside the cavity for sensing accelerations through x-axis, d_x, y-axis, d_y, and z-axis, d_z. It is worth noting that four detectors can be placed for sensing out-of-plane accelerations.

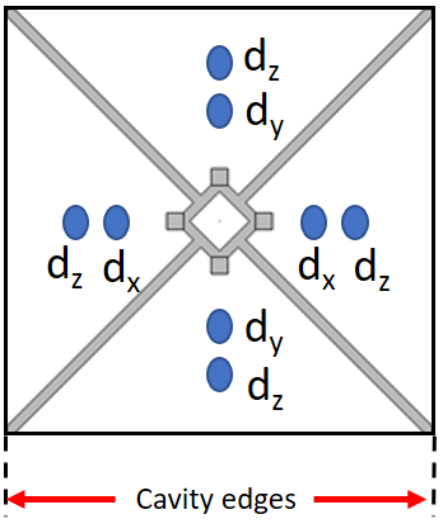

Figure 3.9. *Optimal locations for in-plane and out-of-plane detectors inside the cavity.*

3.2.1 Impact of detector's suspension bridges on sensitivity

In previous simulations, detector suspension bridges were not present. However, their presence in the FEM model is important for accurate estimation of sensitivity. In fact, introducing detector bridges slightly modify the air flow in the cavity, affecting temperature distribution and introducing a new heat exchange between air and sensing bridges, which locally decreases the temperature around the detector. Figure 3.10 presents (xOy) cross section of isotherms obtained without acceleration (i.e. common mode temperature) without (Figure 3.10(a)) and with (Figure 3.10(b)) detectors. Disturbance of the isotherms are then clearly seen when detector bridges are present in the cavity.

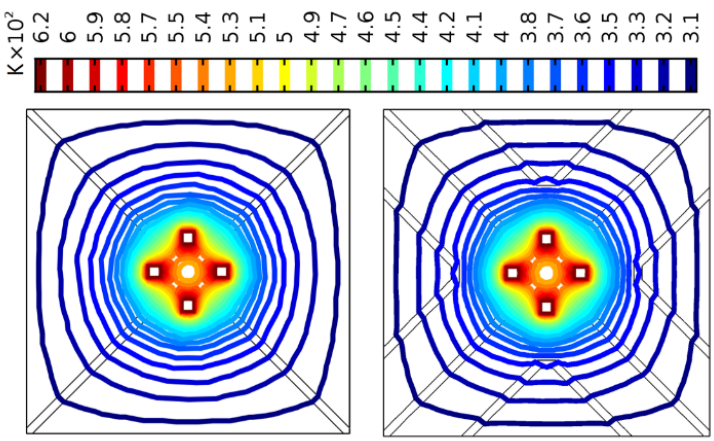

(a) *(b)*

Figure 3.10. *(xOy) cross section of isotherms (a) without and (b) with detector bridges.*

Temperature variations in the detector plane without (black continuous line) and with (red dashed line) detector's suspension bridges for an in-plane and an out-of-plane acceleration of 1g are presented in Figure 3.11 (a) and Figure 3.11 (b), respectively. From both figures, an important decrease in temperature variation is observed and the corresponding maximum sensitivities are given in Table 3.3. It was found that the presence of detector bridges in the model reduces in-plane and out-of-plane sensitivities of about 25% and 35% respectively. From these results, we consider modifying the design of detector's bridges to reduce sensitivity loss.

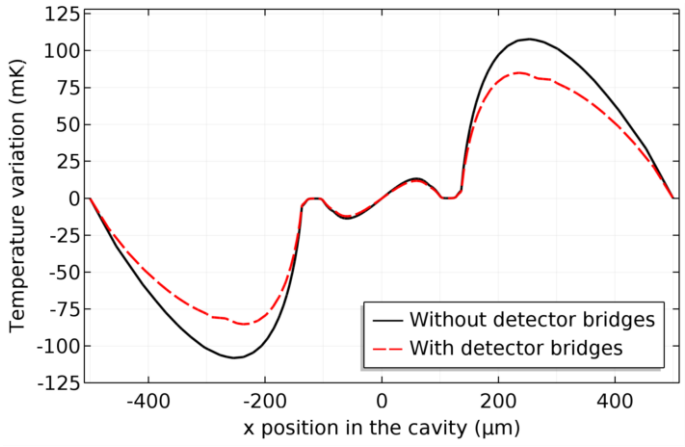

(a)

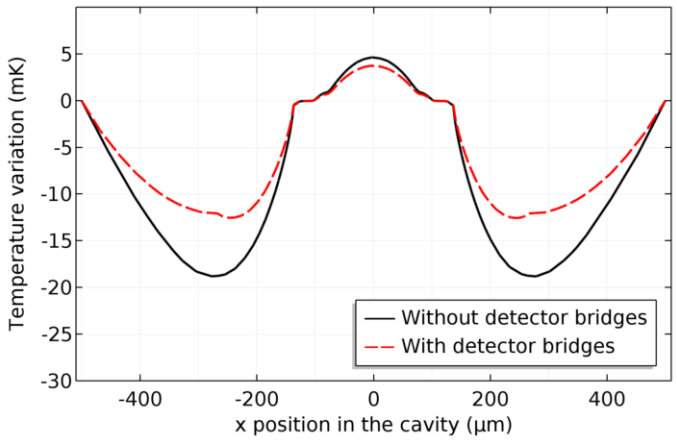

(b)

Figure 3.11. *Temperature variations in the cavity with and without detector bridges due to unity (a) in-plane acceleration and (b) out-of-plane acceleration.*

Table 3.3. *Sensitivity comparison between FEM models with and without detector bridges.*

Parameter	Design without detectors	Design with detectors	Sensitivity decrease
S_x	212	167	25%
S_z	19	12.5	35%

3.2.2 Optimal design of detector's suspension bridges

According to previous results, two different designs of suspension bridges are considered. *Design1* is a Y-shaped bridge, with both in-plane and out-of-plane sensing resistors on the same bridge as shown in Figure 3.12. Then, Figure 3.13 illustrates *Design2* with two independent bridges for in-plane and out-of-plane resistors respectively. This second design aims to reduce thermal couplings between both detectors.

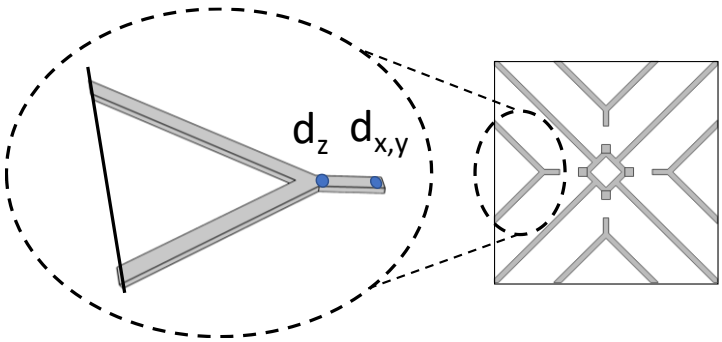

Figure 3.12. *Design1: single arm holding structure.*

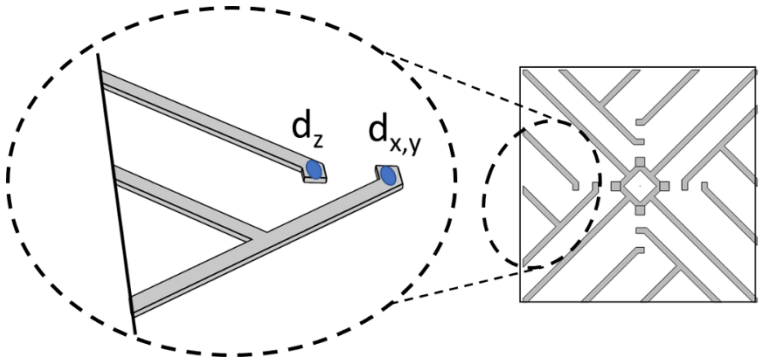

Figure 3.13. *Design2: dual arms holding structure.*

Evaluated sensitivities for these two designs are listed in Table 3.4 for both in-plane and out-of-plane accelerations. The dual arms design leads to a loss in sensitivity of more than 10%. This can be explained by the fact that adding a second SiO_2 bridge creates a new thermal path for heat dissipation by conduction in *Design2*. This bridge increases thermal dissipation from heater to the cavity boundary, increasing disturbance of the hot bubble and therefore decreasing sensitivity.

Table 3.4. *Sensitivities at 15 mW for studied holding structures for detectors.*

	In-plane sensitivity (mK/g)	**Out-of-plane sensitivity (mK/g)**
Design1	169	12
Design2	146	10
Design3	167	12.5
Design4	178	13.5

We have then studied a third solution, *Design3*, with a single bridge, as shown in Figure 3.14, to minimize volume of material and thus heat conduction by placing both detectors at the same location. Since out-of-plane sensitivity is lower, detector's position is set to ±280µm from the heater center. A small increase (decrease) of out-of-plane (in-plane) sensitivity is reported in Table 3.4. To further reduce the thermal conduction to cavity boundaries a last holding structure, *Design4*, has been finally studied (see Figure 3.15).

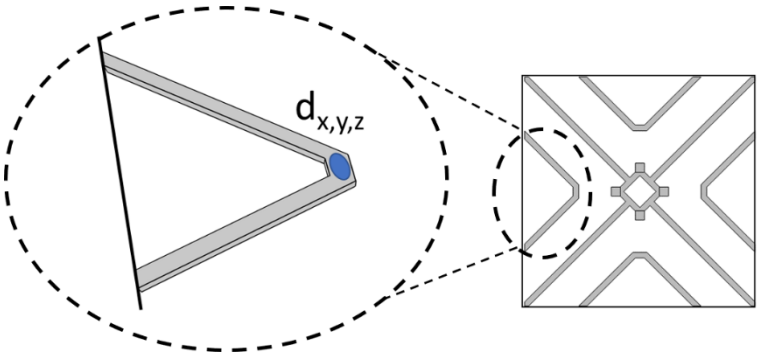

Figure 3.14. *Design3: single arm holding structure with single detectors' location.*

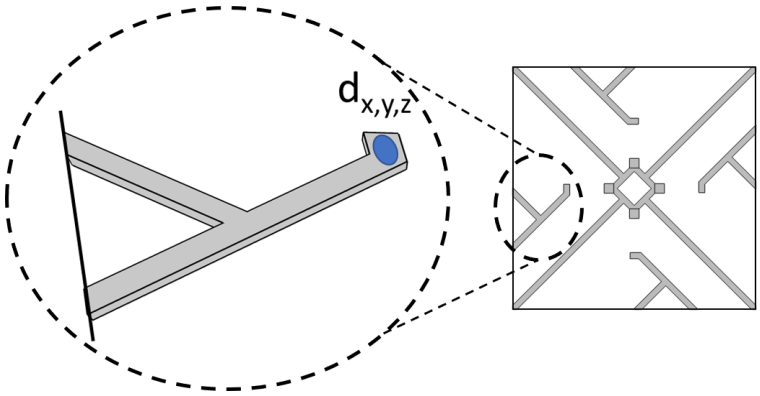

Figure 3.15. *Design4: single arm holding structure with reduced thermal conduction.*

Simulation results, listed in Table 3.4, show that both in-plane and out-of-plane sensitivities are slightly improved when using *Design4* to hold temperature detectors. After verifying compatibility of all 4 designs with FSBM post-process, towards etching simulations (cf. Figure 3.16), we have then chosen *Design4* to elaborate our final sensor.

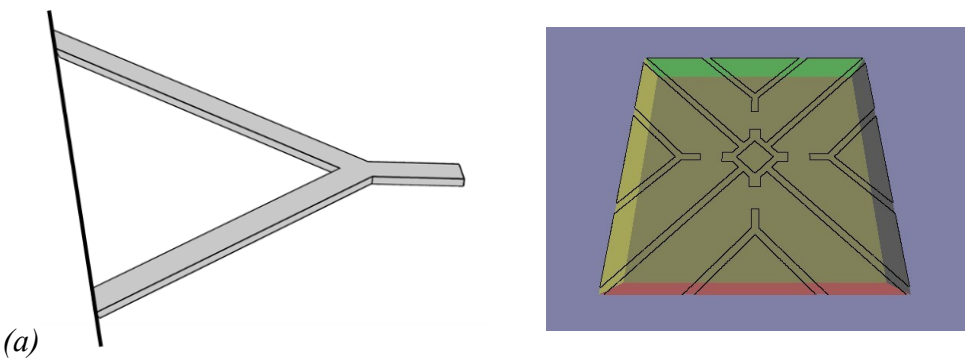

(a)

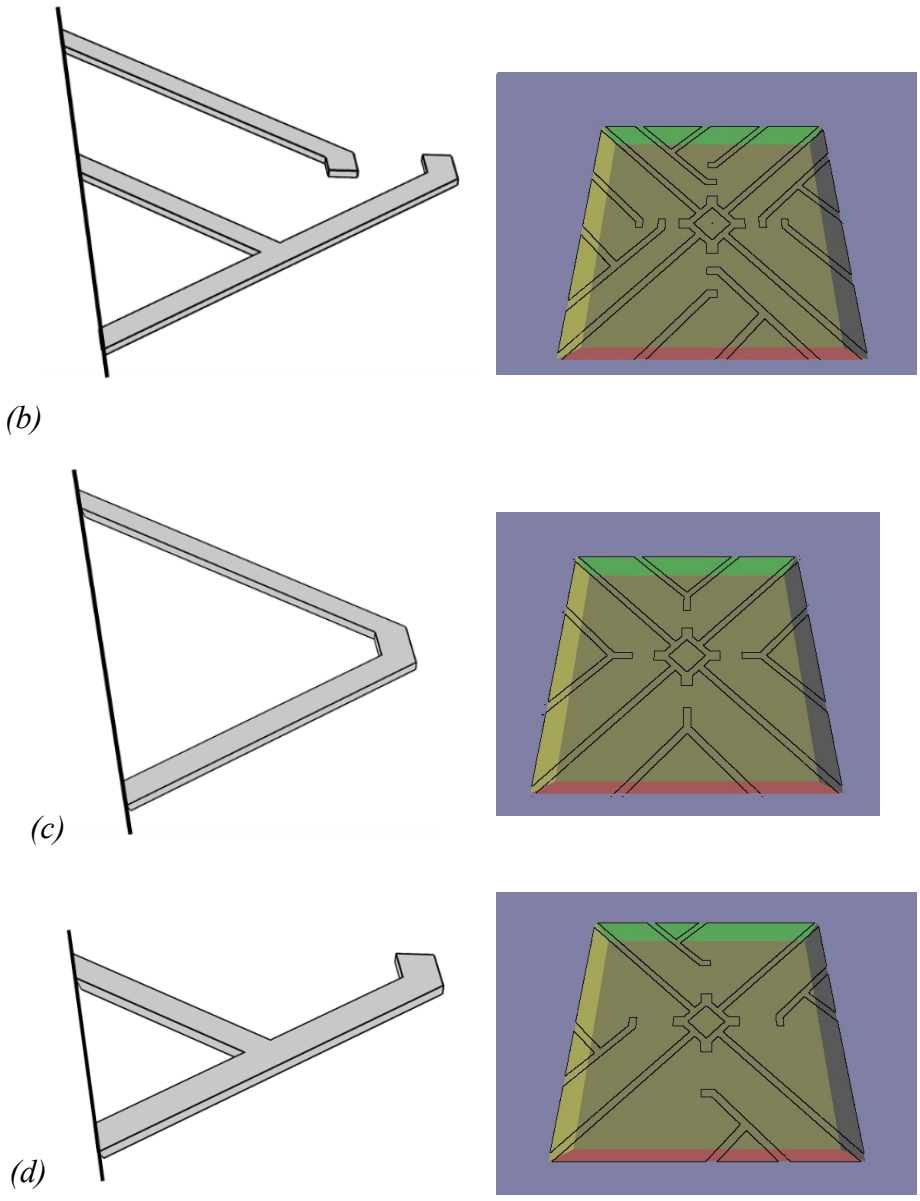

Figure 3.16. *Etching results for different holding structures after 2hours of etching.*

3.3 Performance assessment of the proposed 3-axis microaccelerometer

In this section, sensitivities and energy-efficiency of the proposed convective accelerometer, illustrated in Figure 3.17, are compared with the reference device from (Mailly, Nguyen et al. 2014). Expected improvements relate to an original square-shaped heater holding four independent and deported heat sources and to a new holding structure for detectors with a low thermal conductivity.

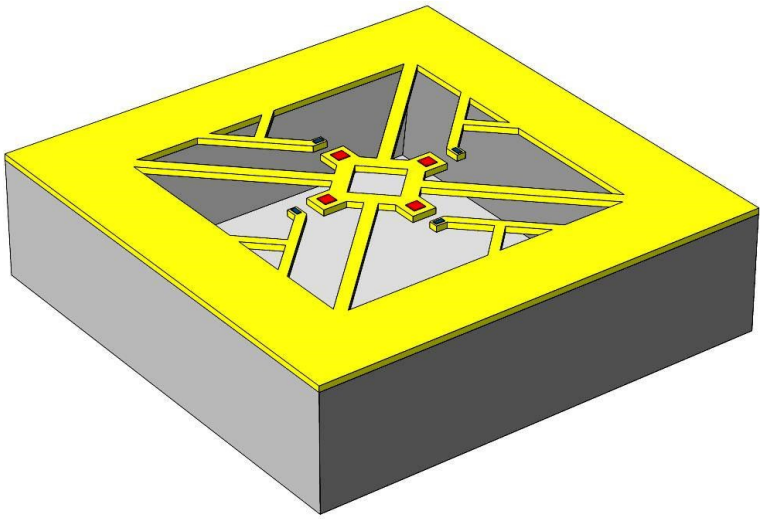

Figure 3.17. *3D illustration of the proposed 3-axis convective accelerometer with optimized heater and low-thermal conduction holders for thermal detectors.*

3.3.1 Assessment of maximum reachable heating power

The main contribution of the new heater design is to enlarge the hot spot area and thus to increase the maximum power dissipation before potential damages while concentrating hot spots only where needed. This potentially leads to doubling the heating power without exceeding a given safety limit in temperature (set to 700K in our case). As shown in Figure 3.18, the maximum heating temperature with the proposed accelerometer is now reached with a heating power of 19mW versus only 9mW using the SoA accelerometer.

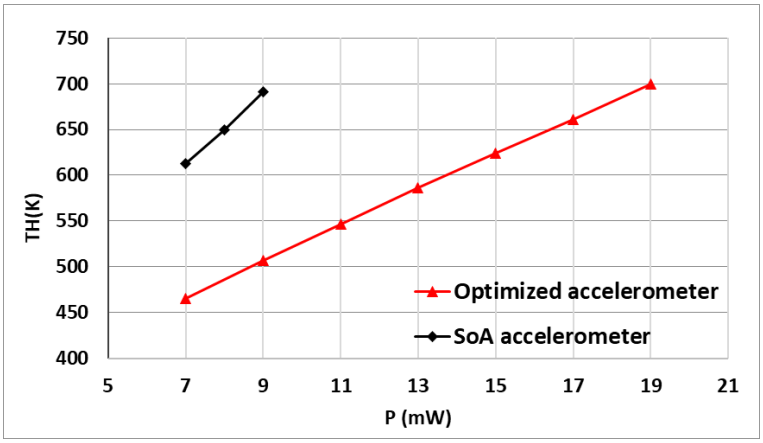

Figure 3.18. *Simulated maximum temperatures of SoA and Optimized 3D accelerometer for various heating powers.*

3.3.2 Assessment of sensitivity

By comparing sensitivities obtained with the proposed shape and with the reference shape, an increase higher than 31% is observed for in-plane sensitivity in the heating power range of 7mW up to 9mW. For out-of-plane sensitivity, improvement is even better, about 71%, at same heating power. For a power consumption of 9 mW, sensitivity increases from 64 mK/g to 84 mK/g for in-plane accelerations and from 3.5 mK/g to 6 mK/g for out-of-plane accelerations.

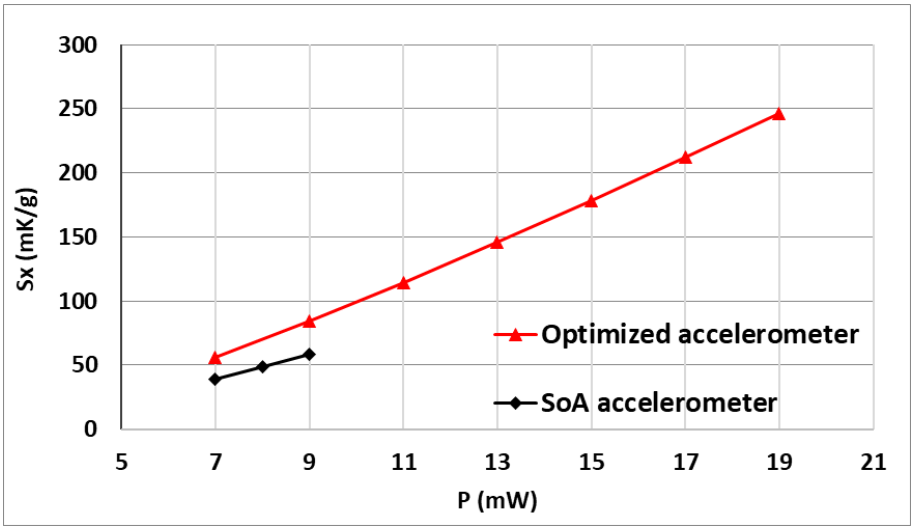

Figure 3.19. *Simulated in-plane sensitivities of SoA and Optimized 3D accelerometer for various heating powers.*

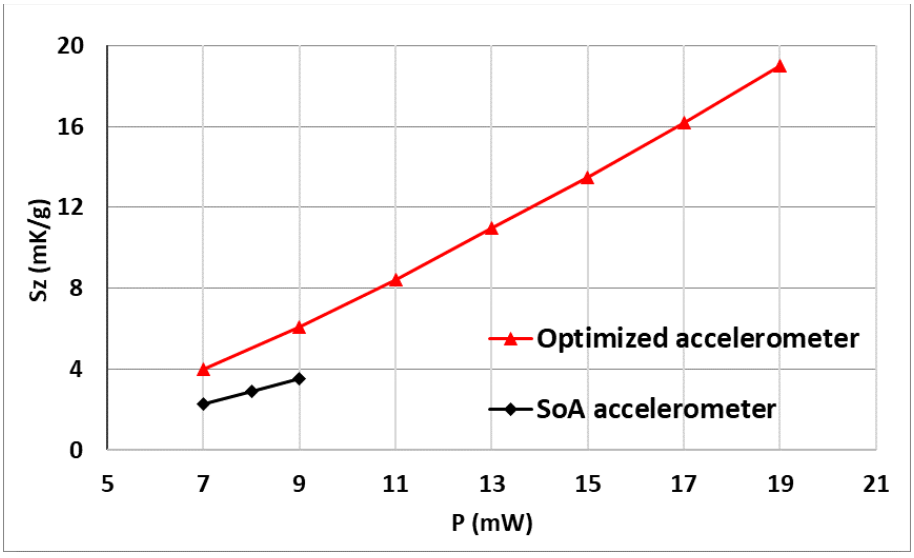

Figure 3.20. *Simulated out-of-plane sensitivities of SoA and Optimized 3D accelerometer for various heating powers.*

As stated in previous section, higher reported sensitivities for the new heater shape at identical heating power is obtained with a lower maximum temperature and thus operating range may extend, as illustrated in Figure 3.19 and Figure 3.20, up to 19 mW in heating power with a nearly 5-fold increase of sensitivity with respect to the minimal heating power of 7 mW.

As a result, maximum sensitivity with the proposed accelerometer is more than four times higher for in-plane, and more than five times higher for out-of-plane accelerations.

3.3.3 Assessment of energy-efficiency

Energy efficiency is defined as the ratio between sensitivity (in mK/g) and the heating power (in mW). Figure 3.21 and Figure 3.22 present calculated efficiencies issued from both SoA and optimized accelerometers. As shown in previous section, at a given power consumption, in-plane and out-of-plane sensitivities are both higher for the proposed heater shape. It is therefore obvious that the latter is more energy-efficient over the lower power range [7 mW – 9 mW]. For power consumption beyond 9 mW, efficiency of our proposed heater rises and reaches a maximum of 13 mK/g/mW and 1 mK/g/mW for in-plane and out-of-plane accelerations respectively. Maximum in-plane and out-of-plane efficiencies of the optimized accelerometer are respectively 2-fold and 2.5-fold the maximum efficiencies of the SoA accelerometer. These results are summarized in Figure 3.23.

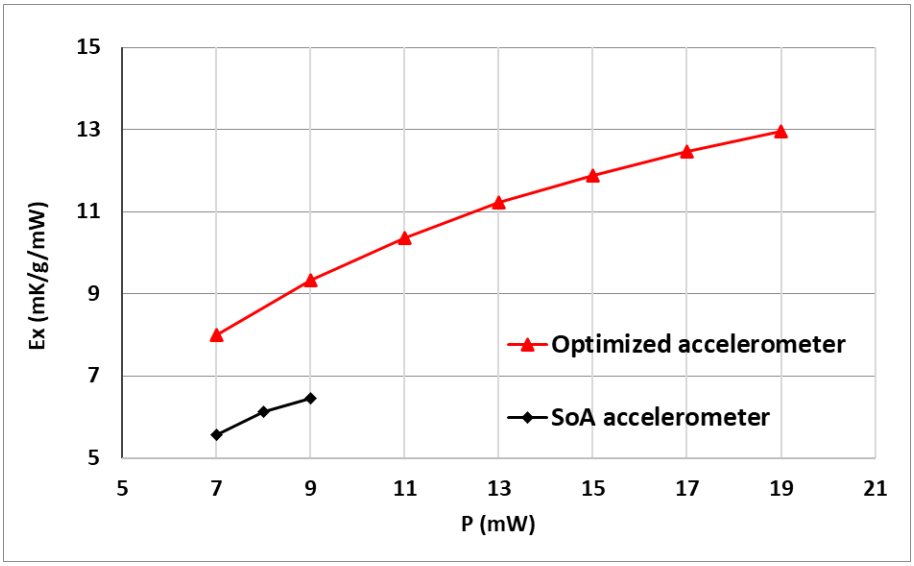

Figure 3.21. *Simulated in-plane efficiencies of SoA and Optimized 3D accelerometer for different heating power.*

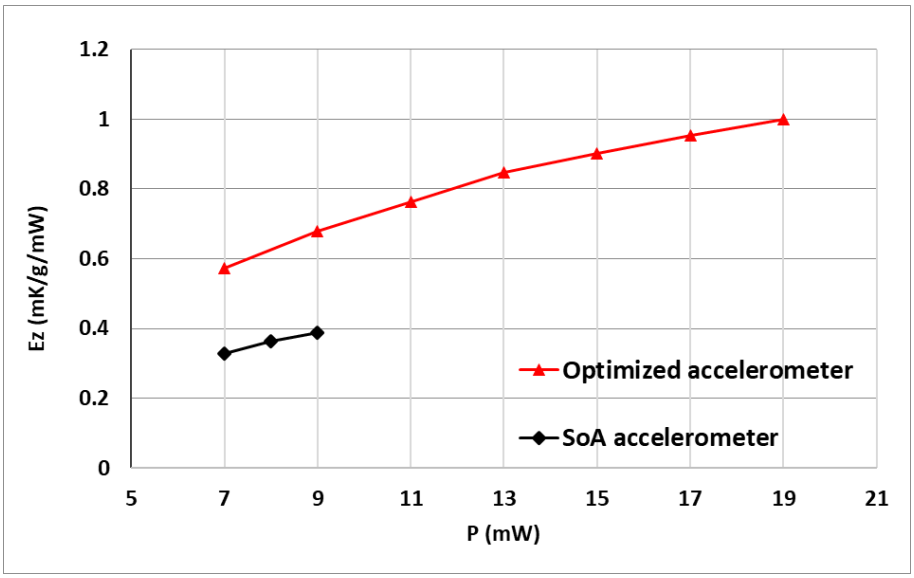

Figure 3.22. *Simulated out-of-plane efficiencies of SoA and Optimized 3D accelerometer for different heating power.*

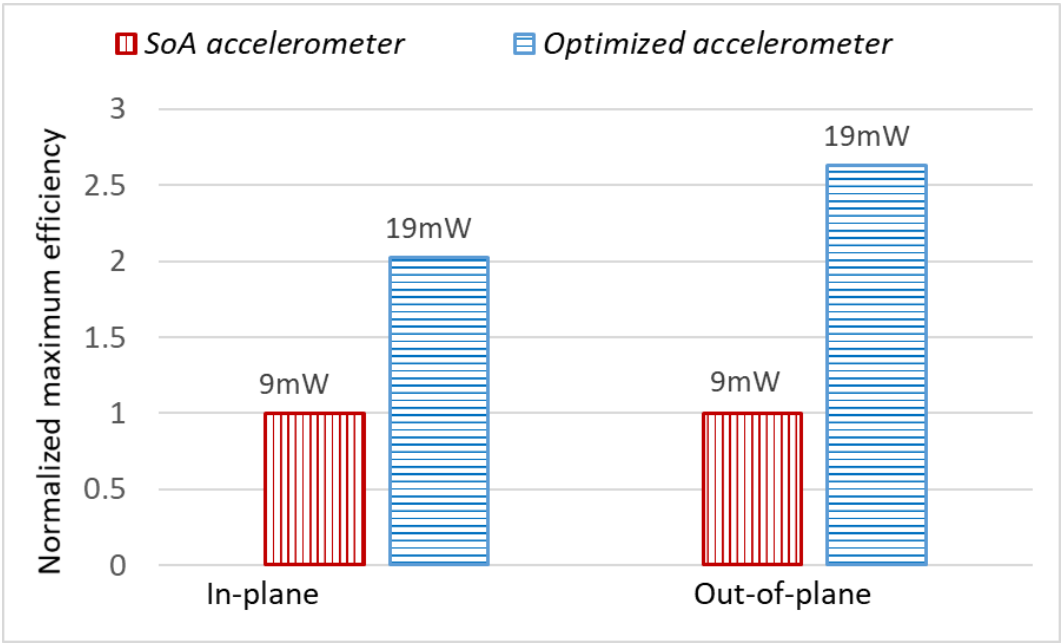

Figure 3.23. *Normalized maximum efficiency for optimized accelerometer and SoA accelerometer for both in-plane and out-of-plane accelerations.*

3.4 CMOS implementation of the developed 3D accelerometer

3.4.1 Design and specifications of the new heater

The new heater design is intended to exploit standard CMOS process, hence high attention was paid to geometry, with respect to design rules, thermal and electrical conductivities as well as the maximum current densities in conductors.

Heater resistor will be implemented with high resistive polysilicon (*PolyH*) which presents the highest sheet resistance available in this 0.35µm manufacturing process. High resistivity allows implementing a high resistance in a reduced footprint, i.e., 15µm×13µm for a 1kΩ resistance. Each of the four resistors is enclosed in a 40µm×40µm wing. Heating resistors are connected in a parallel configuration. Compared to serial connection, parallel configuration allows to reach higher power dissipation and thus higher sensitivity for a given supply voltage.

Simulations show that required power to reach a maximum temperature of 700K is 19 mW, corresponding to a voltage of 2.18V and a total current of 8.72mA (i.e., 2.18mA for each resistance). Current is flowing through 4µm wide metal wires (*met1* layer) implemented along each of the heater's attachment arms. Maximum current density for *met1* layer is 1mA/µm. Thus, wires are designed large enough to support the supplied current of two resistances. Each 4µm wire is then split into two wires to supply two resistors on its left and right sides.

Additionally, four 400Ω *Poly1* resistors are serially connected and implemented as close as possible, i.e., 0.6µm away, to each heating resistor. These resistors will be used to measure average heating temperature. Figure 3.24 illustrates the implementation of microheaters and surrounding temperature monitoring resistors.

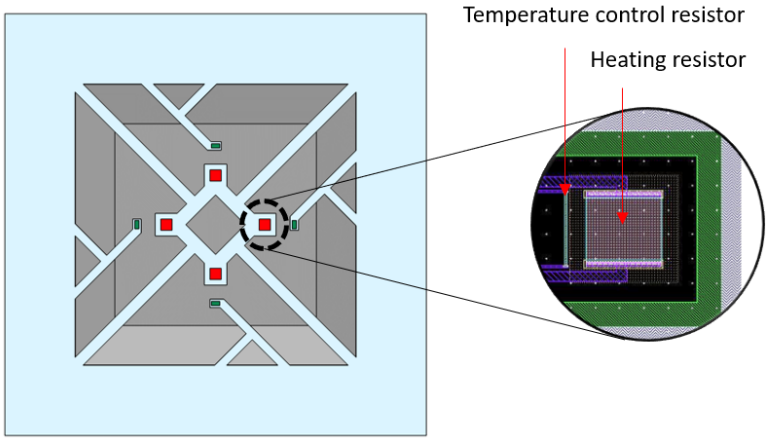

Figure 3.24. *Proposed 3D accelerometer and close-up view on layout of a wing with heating and temperature monitoring resistors.*

3.4.2 Design and specifications of optimized detectors

To choose appropriate material for sensing resistances, sensitivity to temperature change of available resistive materials (*Poly1*, *Poly2* and *PolyH*) is investigated in the operating temperature range, i.e., 300K to 700K, using following equations:

$$R(T) = R_{T0}(1 + T_{C1}\,\Delta T + T_{C2}\;\Delta T^2) \tag{14}$$

$$\alpha(T) = \frac{1}{R}\frac{dR}{dT} \approx \frac{1}{R(T)}\;\frac{R(T+dT) - R(T)}{dT} \tag{15}$$

With:

- $R(T)$, resistance (Ω) at a given temperature T
- R_{T0}, resistance (Ω) at T_0=300K
- $\Delta T = T - T_0$, temperature difference between T and T_0 (K)
- T_{C1} (K^{-1}) and T_{C2} (K^{-2}), linear and quadratic Temperature Coefficient of Resistance
- $\alpha(T)$, thermal sensitivity of relative variation of resistance (K^{-1})

Using (14) and (15), and according to parameters listed in Table 3.5, thermal sensitivity of relative variation of resistance for available resistive layers is presented in Figure 3.25.

Table 3.5. *Material parameters of Poly1, Poly2, PolyH, and Met1 for the AMS 0.35µm CMOS process.*

	Poly1	***Poly2***	***PolyH***	***Met1***
T_{C1} **(x10^{-3} K^{-1})**	0.9	0.59	-0.75	-
T_{C2} **(x10^{-6} K^{-2})**	-	0.77	3.82	-
R_s **(Ω/□)**	8	50	1200	-
J_{met1} **(mA/µm)**	-	-	-	1

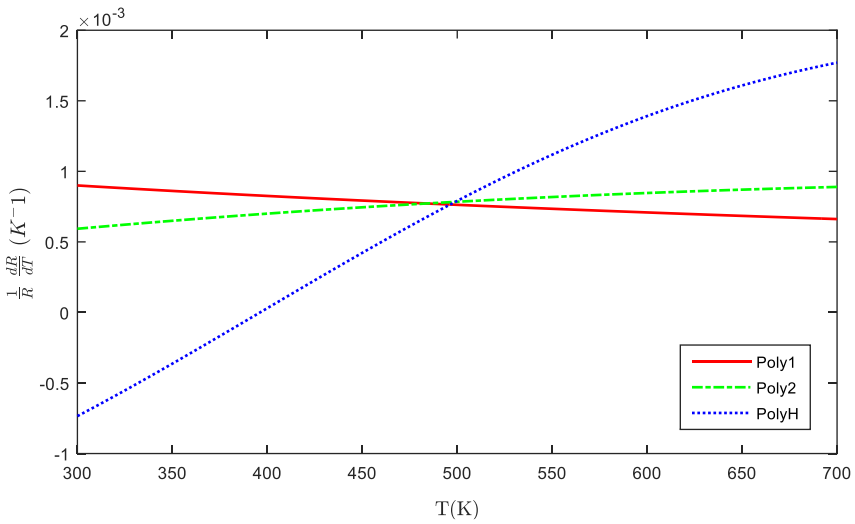

Figure 3.25. *Thermal sensitivity of relative variation of resistances for different resistive layers of AMS 0.35µm CMOS process as a function of temperature.*

From simulated temperature profile (Figure 3.26) at maximum heating temperature, i.e., 700K, common mode temperature of detectors is 358K. According to Figure 3.25, the best sensitivity to temperature variations for a temperature range between 300K and 358K is obtained for *Poly1* layer. Unfortunately, it is not possible to use *Poly1* due to its small sheet resistance. Indeed, detector's holding bridges are designed at minimum possible width (i.e., 25 µm) to reduce heat conduction towards cavity boundaries. Therefore, available surface to implement detectors is small. Final choice for detectors is then to use *Poly2* material which sensitivity to temperature is a bit lower than that of *Poly1* but with a higher sheet resistance.

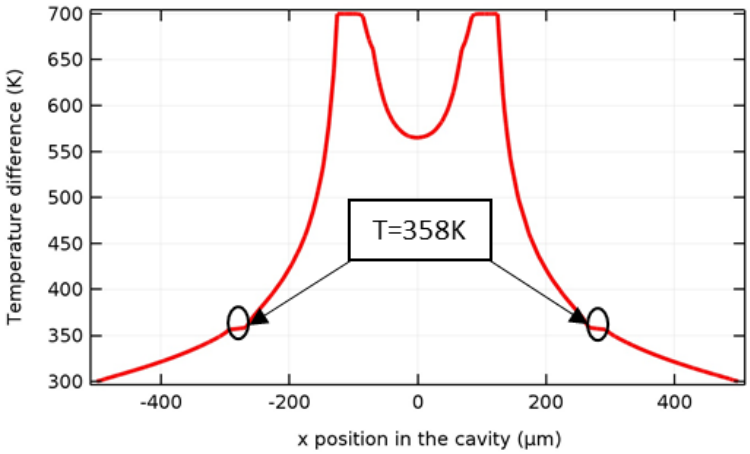

Figure 3.26. *Temperature profile along x-axis without acceleration for maximum heating temperature T_H=700K.*

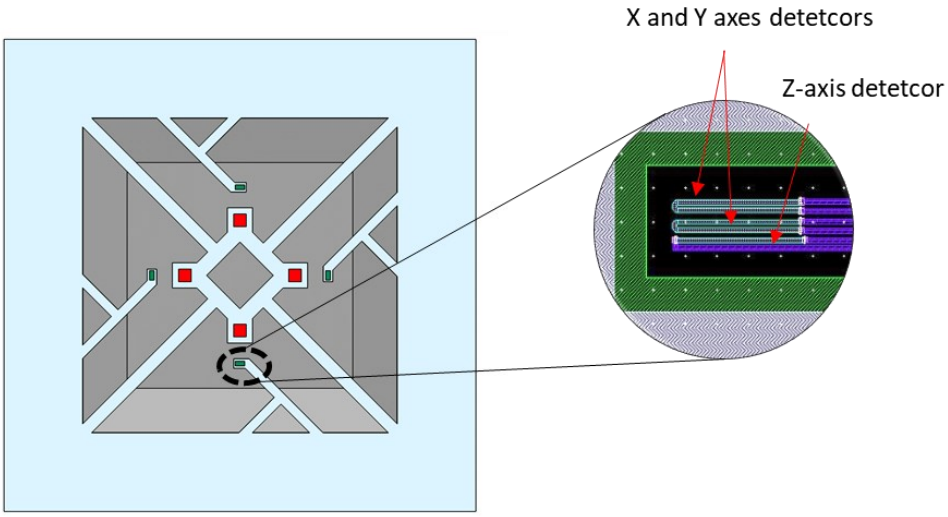

Figure 3.27. *Proposed 3D accelerometer and close-up view on layout of a temperature detector head.*

Each temperature detector head hosts three resistors. Two of them are dedicated to differential temperature measurement due to in-plane acceleration (x- or y-axis). Each is 2.5kΩ at 300K and they are connected in a full bridge configuration. The third resistor is dedicated to common mode temperature measurement due to an out-of-plane acceleration (z-axis). These 1.25kΩ z-axis resistors are connected in series by pairs to measure the average temperature of detectors. Figure 3.27 illustrates the layout of one detector head.

3.4.3 Design and implementation of the CMOS readout electronics

A conditioning and readout circuit is required to convert temperature-induced resistance variations into an electrical voltage and amplify it. The use of CMOS process gives the advantage of placing this circuit on the same chip as the sensing device to obtain a smart MEMS with reduced footprint and cost.

A Wheatstone bridge is the traditional way for measuring resistance variations. This well-known circuit is a very simple arrangement of four resistors. One, two or four of them may be sensitive to a physical magnitude to create quarter, half or full Wheatstone bridge, respectively. Figure 3.28. illustrates the implementation of a full Wheatstone bridge where all resistances are sensitive.

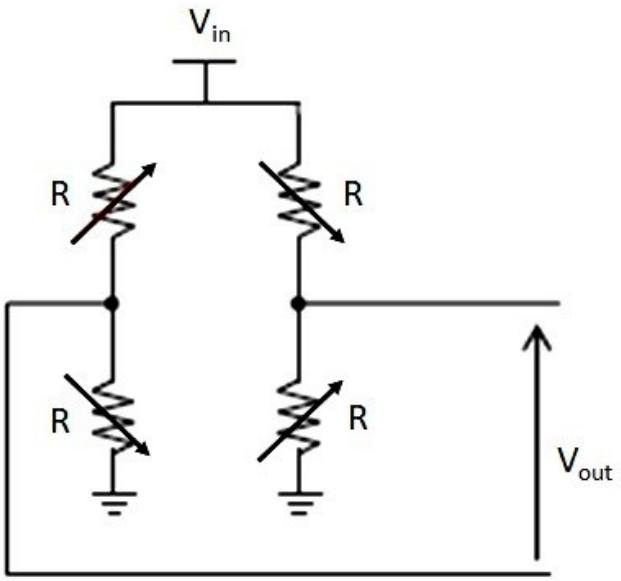

Figure 3.28. *Implementation of a full Wheatstone bridge circuit.*

Differential output voltage of a Wheatstone bridge does not depend on resistance but rather on its relative variation and the number of sensitive resistors. When all nominal resistances are equal to R, it comes:

$$V_{out} = n\frac{\Delta R}{R}\frac{V_{in}}{4} \tag{16}$$

With:

- $\Delta R/R$, the relative change in resistance (equal to $\alpha(T)\Delta T$ according to equation 15)
- n, the number of sensitive resistances (1, 2 or 4)
- V_{in}, the supply voltage (V)

For a given supply voltage, biasing current is inversely proportional to its equivalent resistance, using small resistances requires high biasing current and thus increases power consumption:

$$I = \frac{V_{in}}{R} \tag{17}$$

$$P = R\,I^2 \tag{18}$$

With:

- R, the equivalent resistance (Ω) equals to the nominal resistance of one resistance
- I, the biasing current (A)
- P, the dissipated power (W)

On the other hand, increasing the value of resistances in a Wheatstone bridge decreases the sensor's resolution since the rms value of noise in a resistance is proportional to the square root of its value:

$$V_{noise} = \sqrt{4kTR}\sqrt{BW} \tag{19}$$

With:

- $k = 1{,}82 \,.\, 10^{-23}$ J.K^{-1}, the Boltzmann constant
- T, the temperature (K)
- BW, the bandwidth of the sensor (Hz)

Signal to Noise Ratio (SNR) is an indication of the accelerometer ability to measure small signals. Higher the SNR value is, better the sensitivity. From previous equations, SNR of a Wheatstone bridge writes:

$$SNR_{wheatstone} = \frac{V_{out}}{V_{noise}} = \frac{\Delta R\, V_{in}}{4\, R} \frac{n}{\sqrt{4kTR}\sqrt{BW}} \tag{20}$$

Therefore, for a highly sensitive convective accelerometer, it is very important to use low resistances at the cost of high-power consumption.

As an alternative to Wheatstone Bridge, LIRMM has proposed and patented a bridge with current-recycling and embedded amplification, the so-called active bridge. A typical schematic is presented in Figure 3.29. This circuit merges a Wheatstone bridge with a Low Noise Amplifier (LNA) to provide signal amplification without additional power consumption. This self-biased circuit proved an equivalent performance as a Wheatstone bridge for a lower power consumption (Boujamaa, Alandry et al. 2010) (Boujamaa, Dumas et al. 2009). Therefore, it will be used for conditioning temperature-sensitive resistors in our sensor.

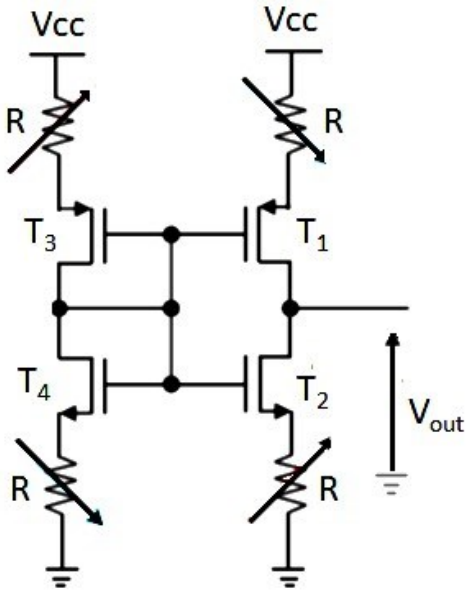

Figure 3.29. *Schematic of an active bridge.*

The active bridge circuit consists of two branches both containing a NMOS and a PMOS transistors in series with two resistors. Like in a Wheatstone bridge, one, two or four sensitive resistances can be used. In the case of a full bridge, with identical nominal value R and identical absolute value of resistance variation ΔR, output voltage V_{out} is given by:

$$V_{out} = 4\,\Delta R\; I\; G \tag{21}$$

With:

- ΔR, the resistance variation (Ω)
- I, the biasing current of each branch (A)
- G, the gain of the embedded amplifier

In the designed demonstrator, two full active bridges are used for x- and y-axis. Full bridge arrangement is possible since for each in-plane axis, four resistors vary equally with an opposite sign for one pair with respect to the second one located in the opposite detector head. Figure 3.30(a) illustrates the architecture of x and y-axis conditioning circuits. A circuit based on an operational amplifier and a single resistance is also added for closed loop operation. This current-to-voltage converter circuit delivers a feedback current in the left branch to balance bridge's differential outputs. As a result, a ground-referenced output voltage is obtained and both sensitivity and full-scale of the smart sensor can be adjusted by choosing R_{fb}.

Considering that all temperature sensors vary with the same sign due to an out-of-plane acceleration, a different configuration is used for z-axis with only two sensitive resistors. Each sensitive resistance is made of two of the four z-axis resistors, distributed on opposite detector heads, connected in series (Figure 3.30-b). An adjustable supply voltage V_{dd_offset} is powering left branches on all active bridges to compensate easily for process-induced offset.

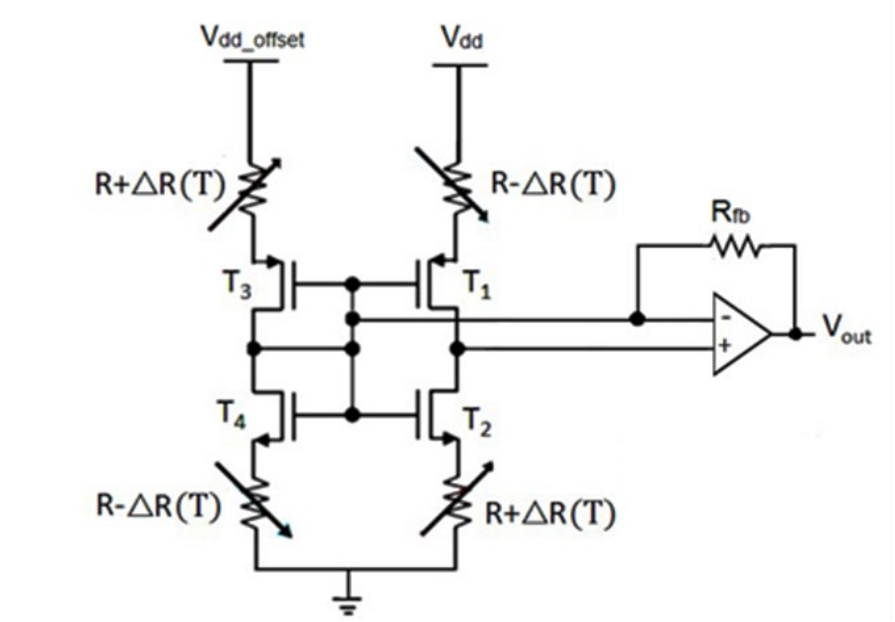

(a)

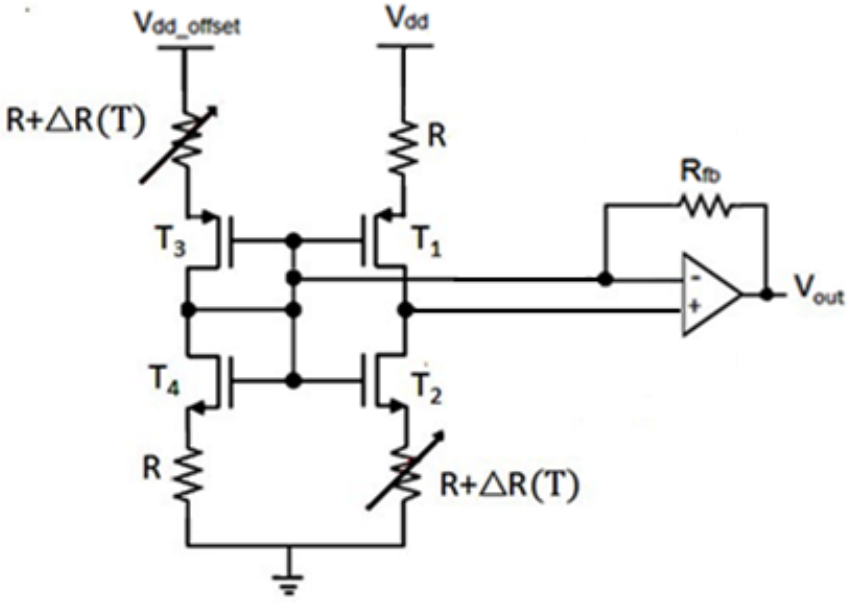

(b)

Figure 3.30. *Conditioning and read-out chains for sensing in-plane (a) and out-of-plane (b) accelerations.*

3.4.4 Preliminary fabrication results

The developed sensor was fabricated in a CMOS 0.35 µm technology from Austria Microsystems (AMS) followed by a FSBM post-process. This fabrication was coordinated by CMP service (Grenoble, France). Figure 3.31 presents the $2.6\,mm \times 2\,mm$ layout of the proposed accelerometer designed using Cadence© Software suite. In this layout, the MEMS area may be clearly distinguished from the electronic area. The MEMS area contains, after FSBM post-process, a cavity and suspended structures that embed sensing and heating resistors. Left electronics area includes the three amplified active bridges and their output stage. Layout at the right side of the MEMS area corresponds to another project. It is then worth noting that the total sensor size including I/O pads is less than $4mm^2$. A picture of the fabricated prototype before (a) and after (b) FSBM post-process is presented in Figure 3.32.

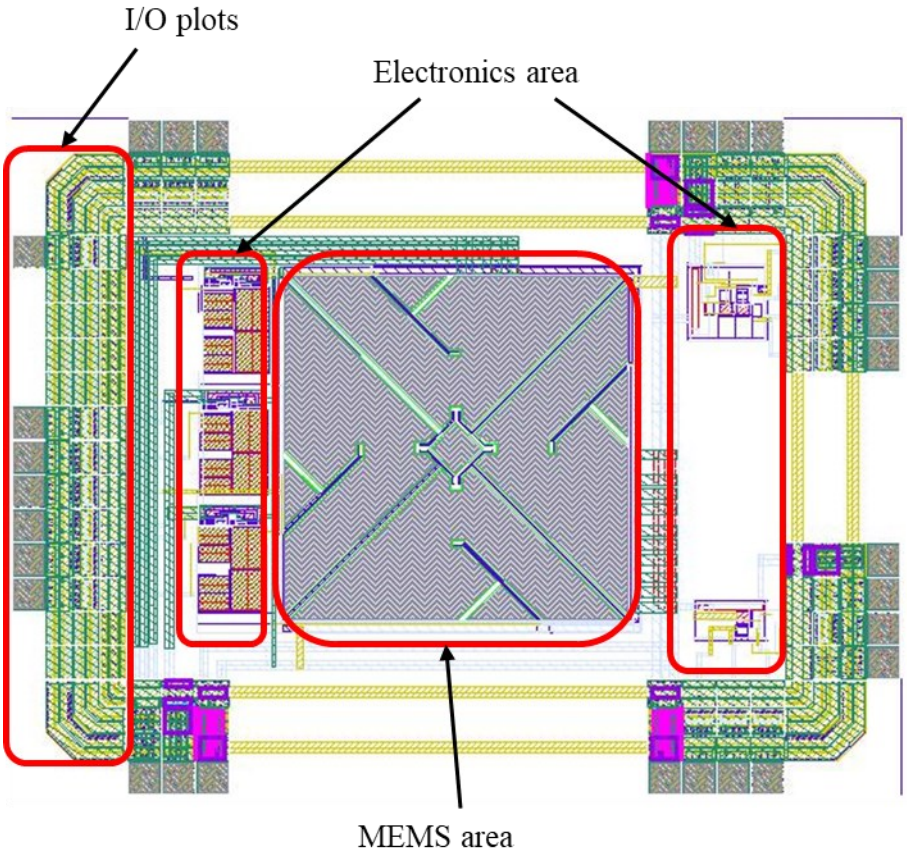

Figure 3.31. *Layout of the proposed Smart-MEMS 3D accelerometer.*

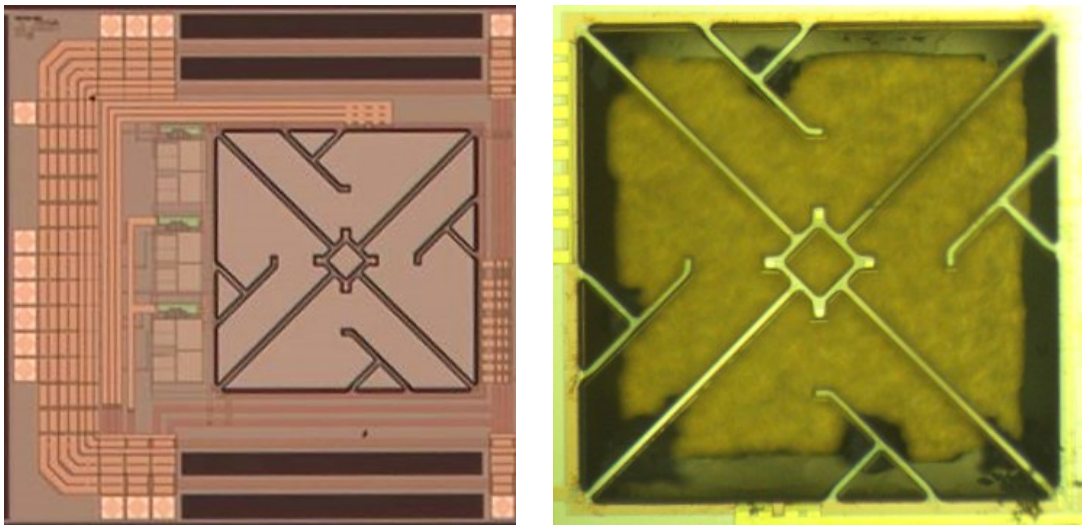

(a) (b)

Figure 3.32. *Picture of the 3D accelerometer die before (a) and after (b) FSBM post-process.*

Conclusion

In this chapter, a 3-axis smart-MEMS accelerometer has been designed in a 0.35µm CMOS technology with respect to FSBM post-process constraints. Performances have been extensively studied with expected improvements in terms of sensitivity and efficiency with respect to a SoA device (Mailly, Nguyen et al. 2014).

Thanks to the use of deported wings to hold heating resistors, a larger hot spot has been observed. Maximum temperature, set at 700K to avoid device damages or early ageing, is reached for a total power dissipation of 19mW, more than twice the maximum heating power of the reference sensor. It results in a large range of possible sensitivities by adjusting the power dissipation.

Additionally, a better positioning of detectors also increases sensitivity. For a given heating power of 9 mW, sensitivities of 84mK/g and 6mK/g for in-plane and out-of-plane accelerations are expected with improvements, with respect to the reference device, of about 31% (64mK/g) and 71% (3.5mK/g) respectively.

As a result, maximum sensitivities, at a constant temperature of 700K, of 246mK/g and 19mK/g for in-plane and out-of-plane accelerations are expected with improvements, with respect to the reference device, of about 283% (64mK/g) and 442% (3.5mK/g) respectively. Efficiency of the sensor in terms of sensitivity to heating power ratio is also strongly improved

with maximum efficiencies at 700K multiplied by about 2 and 2.5 for in-plane and out-of-plane accelerations respectively.

Finally, efficient conditioning and read-out electronics has been implemented on-chip using a self-biased bridge with signal amplification developed at LIRMM a decade ago and the layout of the so-obtained design has been presented. A prototype has been manufactured in a 0.35µm CMOS technology followed by a FSBM post-process to create the cavity and release suspended structures that hold heater and detectors. Tests have not been undertaken at the time of writing.

REFERENCES

Boujamaa EM., Alandry B., Hacine S., Latorre L., Mailly F., Nouet Pascal., « A low power interface circuit for resistive sensors with digital offset compensation », *Proceedings of 2010 IEEE International Symposium on Circuits and Systems*, 2010.

Boujamaa EM., Dumas N., Latorre L., Mailly F., Nouet P., « An innovative, offset immune, conditioning and read-out circuitry for resistive MEMS sensors », *Joint IEEE North-East Workshop on Circuits and Systems and TAISA Conference*, 2009.

Mailly F., Nguyen H.B., Latorre L., Nouet P., « CMOS implementation of a 3-axis thermal convective accelerometer», *IEEE Sensors*, 2014, p. 1471-1474.

Mezghani B., Tounsi F., Rekik AA., Mailly F., Masmoudi M., Nouet P., « Sensitivity and power modeling of CMOS MEMS single axis convective accelerometers », *Microelectronics Journal,* vol. 44, n° 12, 2013, p. 1092-1098.

Chapter 4: Analytical/Numerical modeling of a CMOS 3-axis convective accelerometer

Introduction

In order to predict the response of a convective microaccelerometer, or inversely, to design a specific sensor for a given sensitivity, it is necessary to accurately describe the relation between sensor sensitivity and both design and operation parameters. Two approaches are generally used. The first one consists in a mathematical modeling of a simplified geometry of the accelerometer. The second approach consists in numerical simulations based on Finite Element Model (FEM) analysis to accurately determine sensor's performance. To get the best of the above, compact analytical models calibrated with respect to FEM simulations are proposed in this chapter to quickly calculate sensitivities of the proposed CMOS MEMS triaxial convective accelerometer. From an initial set of FEM simulations, we will first establish analytical expressions representing both in-plane and out-of-plane sensitivities as a function of design and operation parameters. The so-obtained compact analytical models will be then validated with respect to FEM simulations to demonstrate their accuracy over a wide range of design parameters and heater temperatures. To our knowledge, no such compact models exist in literature to estimate sensitivities of 3-axis convective accelerometers.

4.1 Compact analytical/numerical modeling approach

4.1.1 FEM model and nominal sensor geometry

For the sake of simplicity and speed, we decided to build a FEM model of the sensor without detectors' suspension bridges. These structures reduce sensitivity by about 20%. However, their inclusion in FEM simulations increases simulation time by about 30%. In addition, their design is specific for each heater/cavity dimensions. We will therefore develop a set of compact models without taking into account detectors' suspension bridges, and the over-sensitivity induced by this simplification can be further compensated.

FEM model is based on the previously proposed heater. A cross-section of the microsensor with main geometrical parameters is presented in Figure 4.1. Nominal values are chosen to reach maximum sensitivity for nominal value of cavity half width, $r_{o,}$ of 500 µm. These nominal values are reported in Table 4.1.

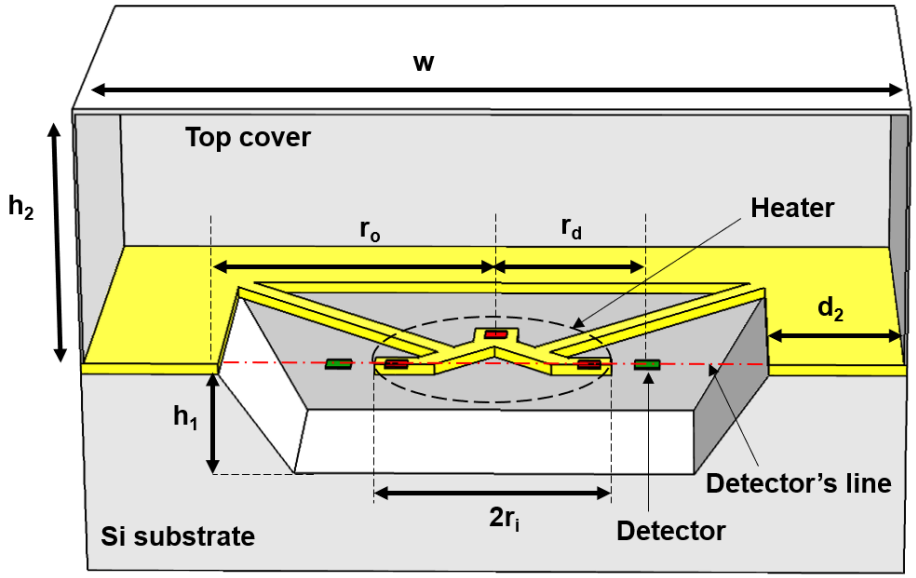

Figure 4.1. *Simplified cross-sectional view of the thermal accelerometer under study with main design parameters.*

Table 4.1. *List of accelerometer parameters and nominal values*

Symbol	Description	Value	Unit
r_i	Heater half-width	135	µm
r_o	Bottom cavity half-width	500	µm
$r_{d(x,y)}$	Optimal position for in-plane detectors	260	µm
$r_{d(z)}$	Optimal position for out-of-plane detectors	280	µm
h_1	Bottom cavity depth	700	µm
h_2	Top cover height	3	mm
d_2	Distance from bottom cavity edge to lateral boundary	3	mm
w	Top cover width = 2 (r_o + d_2)	7	mm

4.1.2 Steps for analytical/numerical modeling

The sensitivity of the convective accelerometer, which working principle is based on the natural convection of fluid, can be expressed as:

$$S = \frac{\delta T}{a} \propto Ra\, f(R)\, \Delta T_H \tag{22}$$

With:

- *S,* the sensitivity (K/g),
- *δT,* the acceleration-induced temperature variation of detectors (K)
- *a,* the applied acceleration (g) with 1g = 9.8 m.s^{-2}
- *Ra*, the dimensionless Rayleigh number
- *f(R)*, a function of device geometry
- ΔT_H, temperature difference between heater and bulk (K)

This expression shows that the sensitivity is proportional to the Rayleigh number, i.e. to fluid properties, to the geometry, represented by f(R), and to heater temperature with respect to substrate, ΔT_H (Lin and Jones 2005).

In this chapter, we aim to express the dependance of the sensitivity on heater temperature, T_H, and main geometrical parameters h_1, h_2, r_o and d_2. Therefore, FEM simulations of the convective accelerometer are performed by varying these parameters one by one to characterize their effect on sensitivity.

Design of Experiment is as follows:

- Impact of heating temperature on sensitivity is first extracted for both in-plane and out-of-plane accelerations, for nominal geometry corresponding to maximum sensitivity. S_{T_H} (mK/g), i.e., the nominal sensitivity as a function of heater temperature is established.
- Impact of cavity depth on sensitivity is characterized by varying h_1. C_{h1}, a dimensionless correction factor, is determined as a function of h_1.
- Impact of cavity half width, r_o, on sensitivity is determined for different values of r_o. C_{ro}, a dimensionless correction factor, is determined as a function of r_o.
- Impact of top cavity dimensions (h_2 and d_2, respectively) is then investigated. C_{h2} and C_{d2} a pair of dimensionless correction factors are determined as a function of h_2 and d_2.

Final expressions for in-plane and out-of-plane sensitivities are then expressed as:

$$S_{(x,y)} = S_{T_H(x,y)}\ C_{h1(x,y)}\ C_{h2(x,y)}\ C_{ro(x,y)}\ C_{d2(x,y)} \tag{23}$$

$$S_{(z)} = S_{TH(z)}\ C_{h1(z)}\ C_{h2(z)}\ C_{ro(z)}\ C_{d2(z)} \tag{24}$$

Where subscripts *(x,y)* and *(z)* refer, respectively, to in-plane and out-of-plane sensitivities.

Since nominal values for h_1, h_2 and d_2, specified in Table 4.1, correspond to maximum sensitivity, all three associated correction factors are always lower than unity. Similarly, since the nominal value of r_o corresponds to nominal sensitivity, S_{T_H}, C_{ro} will be equal to 1 for r_o=500µm.

4.2 Impact of heater temperature

To establish the dependance of sensor sensitivity on heater temperature T_H, numerical studies are performed on a sensor with nominal dimensions and heater temperatures ranging from 400K up to 700K, which is the highest temperature that can be used without jeopardizing device reliability (Baglio, Castorina et al. 2002, Chaehoi 2005).

Acceleration-induced temperature variations (i.e., difference in temperature with and without acceleration) are then evaluated for each heater temperature. These are plotted in Figure 4.2(a) and Figure 4.2(b), for in-plane (x- and y-axis) and out-of-plane accelerations, respectively, as a function of the detectors' position.

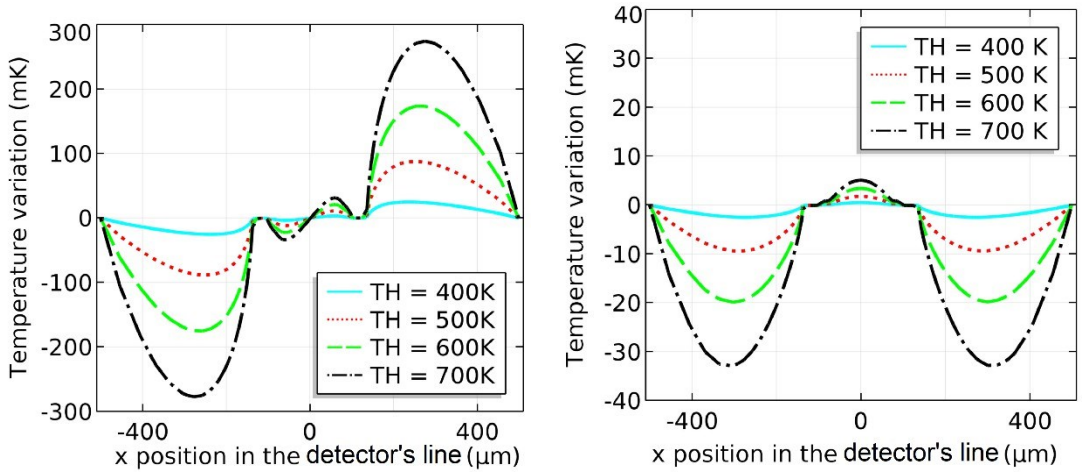

Figure 4.2. *Acceleration-induced temperature variations inside the cavity for T_H ranging from 400K up to 700K for (a) 1g in-plane, and (b) 1g out-of-plane accelerations.*

In-plane and out-of-plane sensitivities are then extracted at x-position corresponding to the maximum temperature variation and plotted, respectively, Figure 4.3(a) and Figure 4.3(b) versus heater temperature difference ΔT_H.

Using nominal parameters of the sensor, the location of maximum temperature variations, from heater-center, is 260 µm for in-plane and 280 µm for out-of-plane sensitivities. Negligible variations of these optimal locations are observed when varying T_H.

The exponential shape of Figure 4.3(a) and Figure 4.3(b) indicates that sensitivity is strongly dependent on T_H.

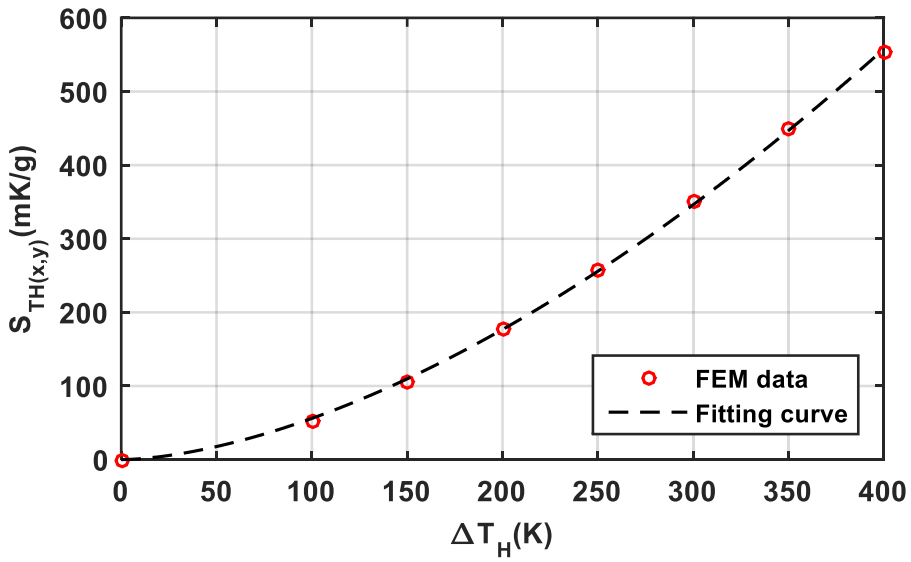

(a)

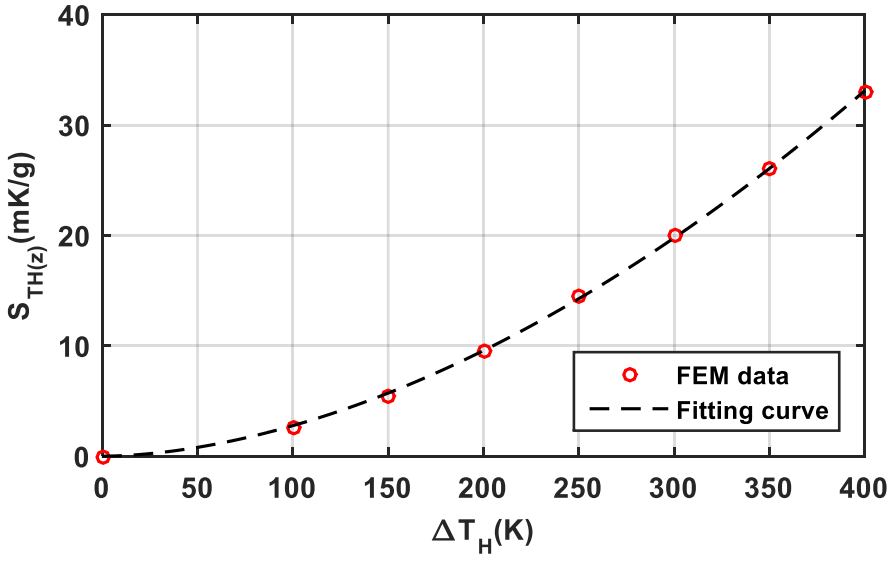

(b)

Figure 4.3. *(a) In-plane and (b) out-of-plane sensitivities vs. heater temperature difference.*

Using MATLAB, a simple curve fitting operation is applied on the data points extracted from simulation using this equation:

$$S_{T_H} = a\, x^n \tag{25}$$

Coefficients a and n are given by MATLAB fitting function and nominal in-plane sensitivity is then expressed, in mK/g, as a function of heater temperature:

$$S_{T_H(x,y)} = 0.026\,(T_H - T_o)^{1.66} \tag{26}$$

Likewise, nominal out-of-plane sensitivity, in mK/g, is given by:

$$S_{T_H(z)} = 7.2 \times 10^{-4}\,(T_H - T_o)^{1.8} \tag{27}$$

4.3 Impact of bottom cavity depth

Depth of the micromachined bottom cavity is considered as the most critical parameter affecting sensitivity (Luo and Young 2001, Courteaud, Crespy et al. 2008, Garraud, Combette et al. 2011). This geometrical parameter is strongly dependent on silicon micromachining conditions, such as etching time, etchant solution, and temperature conditions during the anisotropic etching post-process.

While modeling sensitivity dependence on bottom cavity depth, heater temperature should also be taken into consideration. In this set of simulations:

- h_1 is varied from 50µm up to 700µm with 50µm steps.
- For each value of h_1, a parametric study is performed on a range of heater temperature from 350K to 700K. Other parameters h_2, d_2, r_i *and* r_o are set to their nominal values (Table 4.1).
- Both in-plane and out-plane acceleration-induced temperature variations, along the x-axis, are simulated for different heater temperature.

As an example, acceleration-induced temperature variations are plotted for some bottom cavity depths at a heating temperature of 600 K for in-plane, Figure 4.4(a), and out-of-plane, Figure 4.4(b), accelerations.

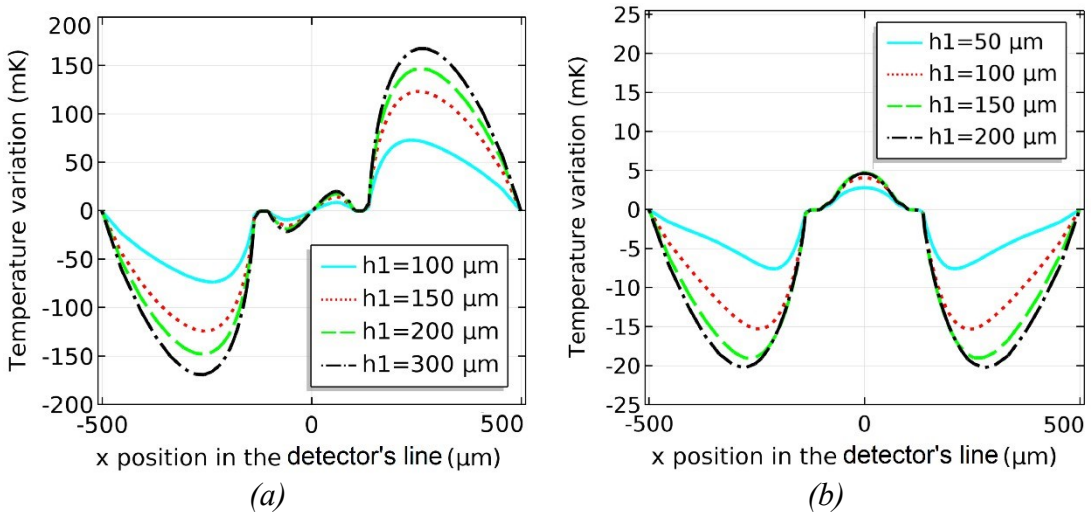

Figure 4.4. *temperature variations along x-axis for different bottom cavity depths, h_1, T_H=600K and (a) 1g in-plane accelerations, or (b) 1g out-of-plane accelerations.*

From each combination of T_H and h_1, sensitivity is extracted, from temperature variation profile, and plotted with respect to the sensitivity obtained for nominal value of h_1, i.e., 700µm, at same temperature T_H. We then obtain a quasi-linear variation for each value of h_1 as reported in Figure 4.5(a) and Figure 4.5(b) for in-plane and out-of-plane accelerations respectively. An attenuation factor can be extracted from the slope of each line.

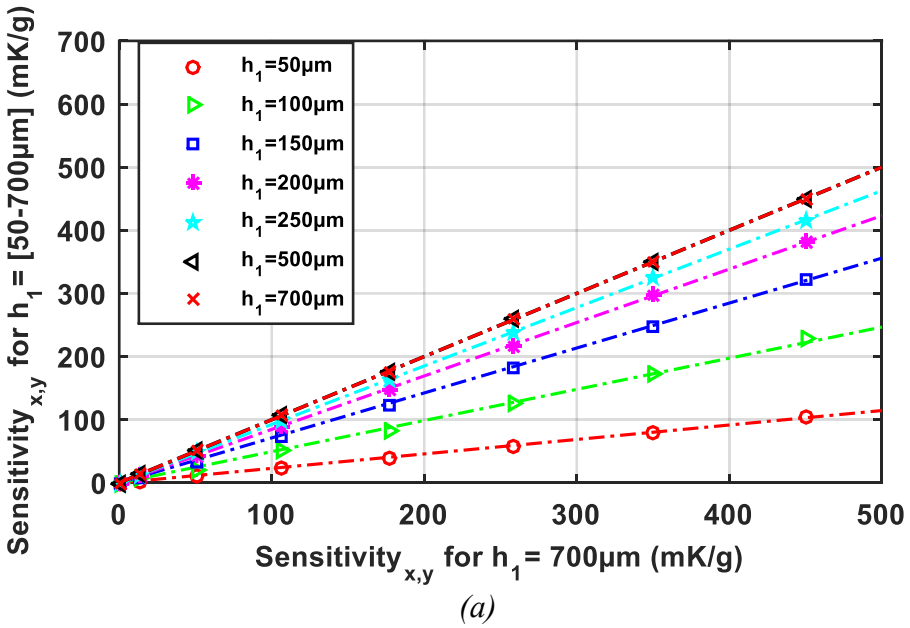

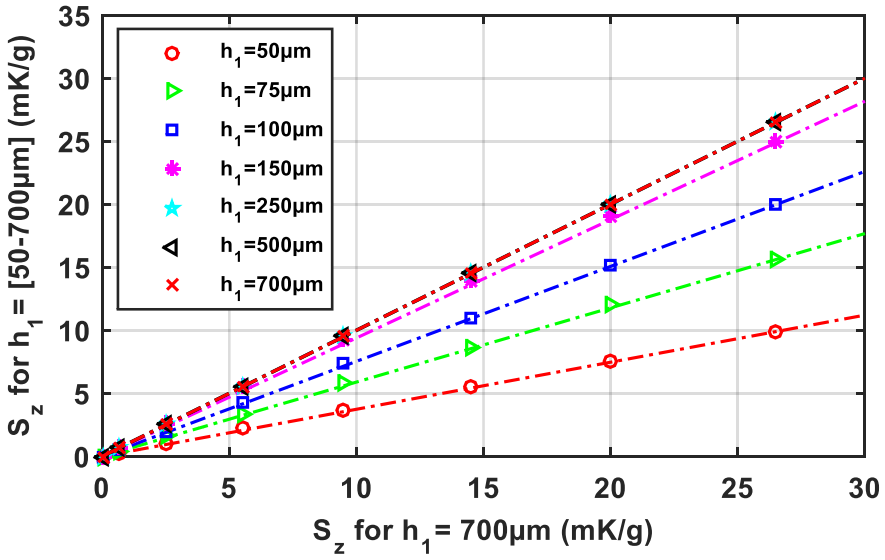

(b)

Figure 4.5. *(a) In-plane and (b) out-of-plane sensitivities for h_1 = [50µm-700µm] vs sensitivity for h_1=700µm for different heater temperatures.*

From the above, correction factors $C_{h1(x,y)}$ and $C_{h1(z)}$ may be plotted versus h_1 in Figure 4.6 for (a) in-plane and (b) out-of-plane sensitivities. Impact of cavity depth h_1 is similar for in-plane and out-of-plane sensitivities. For small values of h_1, a linear relationship is observed, then, for higher values of h_1, saturation occurs (i.e., sensitivity becomes constant), and the correction factor tends toward 1.

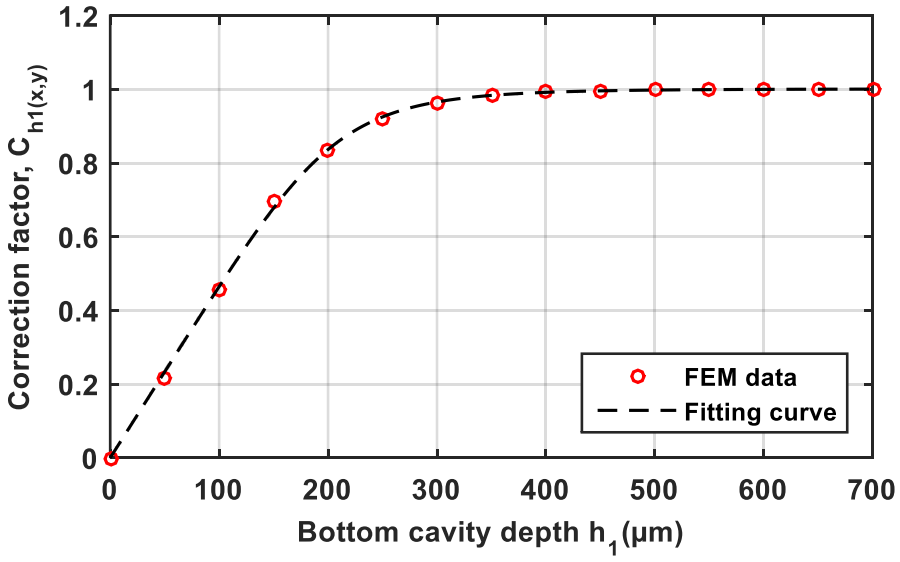

(a)

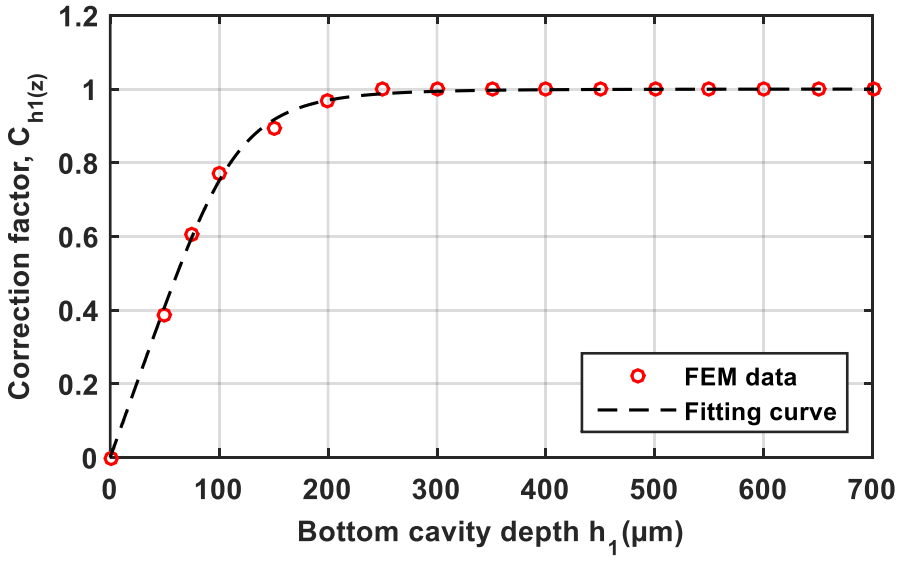

(b)

Figure 4.6. *Correction factors for (a) in-plane and (b) out-of-plane sensitivities vs. bottom cavity depth h_1.*

To explain this behavior, isotherms generated by the heater inside the bottom cavity, for h_1=50µm, 100µm, 400µm and 700µm are reported in Figure 4.8(a), (b), (c) and (d), respectively. For bottom cavity depths higher than 400 µm, the size and shape of the hot bubble stays almost the same. The latter is solely governed by heater temperature and distance to lateral walls of the bottom cavity fixed by r_o. For this reason, sensitivities stay constant for a given value of the pair (T_H, r_o) for large cavity depth. However, bottom cavity depth becomes a crucial limiting factor for lower values. Here, it modifies the shape and size of the hot bubble limiting acceleration-induced temperature variation and therefore decreases the sensitivity.

(a) *(b)*

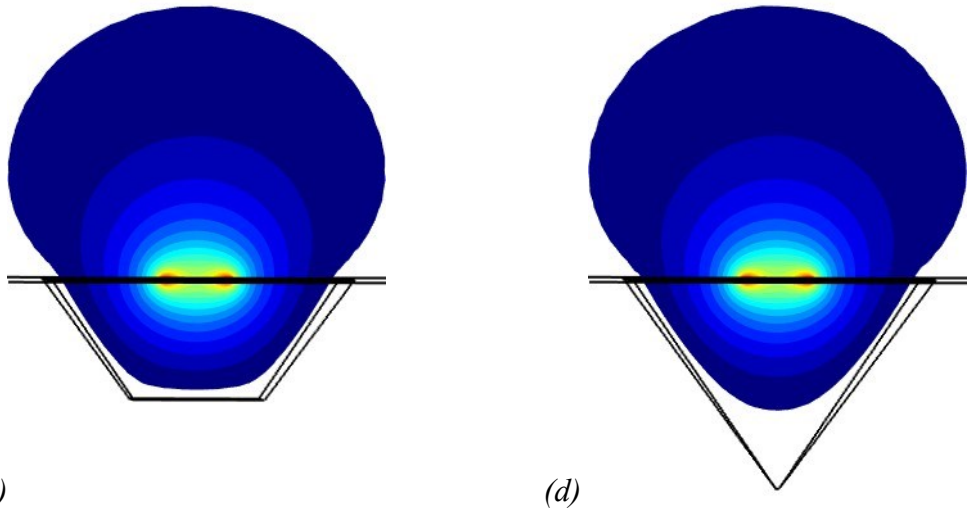

(c) *(d)*

Figure 4.7. *Cross-sections of isotherms generated by the heater inside bottom cavities h_1 of (a) 50 µm, (b) 100 µm, (c) 400 µm and (d) 700 µm.*

From the above, the impact of h_1 on sensitivity can be modeled as:

$$C_{h_1} = \frac{h_1}{\sqrt[n]{{h_1}^n + b^n}} \tag{28}$$

As expected, the correction factor of equation (28) tends toward 1 when h_1 is high enough and reduces for lower values of h_1. Constant b is the depth at which the transition between linear and saturation regions occurs, whereas n is fixed by the shape of the transition between both regions. Using (28) as a model to fit the data points, both b and n constants are obtained from the MATLAB fitting function. The correction factors $C_{h1(x,y)}$ and $C_{h1(z)}$ for the microsensor under investigation are then given by:

$$C_{h_1(x,y)} = \frac{h_1}{\sqrt[5]{h_1^5 + 215^5}} \tag{29}$$

$$C_{h_1(z)} = \frac{h_1}{\sqrt[4]{h_1^4 + 122^4}} \tag{30}$$

Transition depths in (29) and (30) corresponds to r_o= 500 µm. Since these transition depths depend linearly on the distance between cavity side walls (Rekik 2011), expressions of correction factors can be generalized as:

$$C_{h1(x,y)} = \frac{h_1}{\sqrt[5]{h_1^5 + (0.43\, r_o)^5}} \tag{31}$$

$$C_{h1(z)} = \frac{h_1}{\sqrt[4]{h_1^4 + (0.24\, r_o)^4}} \tag{32}$$

The effect of the bottom cavity half-width r_o on the sensitivity will be studied extensively in next section.

4.4 Impact of bottom cavity width

To model sensitivity dependence on bottom cavity half-width r_o, FEM simulations have been performed for different pairs of heater temperature T_H and bottom cavity depth h_1 for r_o ranging from 400 µm up to 1200 µm. The five simulated pairs are (400K, 0.25r_o), (450K, 0.5r_o), (500K, 0.75r_o), (550K, r_o), (600K, 1.25r_o), where h_1 is a function of r_o. Minimum value for bottom cavity half-width r_o is set to 300µm, which is the smallest cavity fabricated for CMOS MEMS convective accelerometer (Mukherjee, Basu et al. 2017).

The so-obtained temperature profiles, along the x-axis, for different values of r_o, T_H=600K and h_1=1.25r_o, are plotted in Figure 4.8 for (a) in-plane and (b) out-of-plane accelerations.

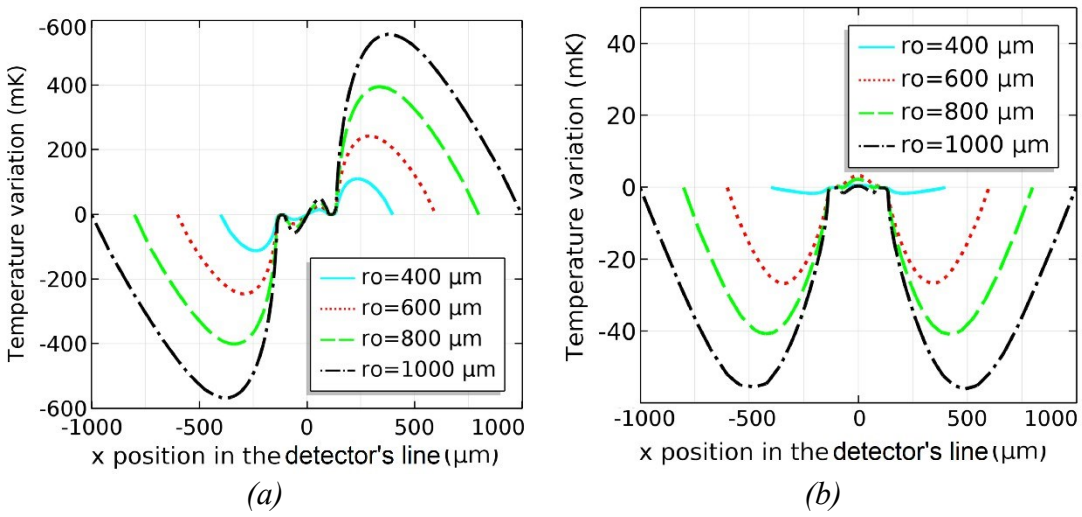

Figure 4.8. *Acceleration-induced temperature variations along the x-axis for different r_o, T_H=600K and h_1=1.25r_o, for (a) in-plane and (b) out-of-plane accelerations.*

It is worth noting that optimal position of detectors is strongly affected by r_o. To model this phenomenon, the optimal positions for in-plane, $r_{d(x,y)}$, and out-of-plane, $r_{d(z)}$, accelerations are plotted as a function of r_o (Figure 4.9 (a) and (b), respectively).

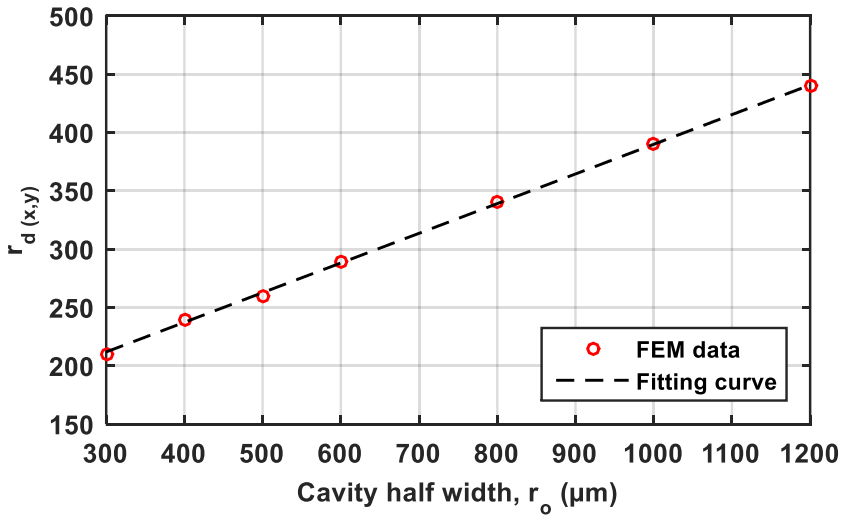

(a)

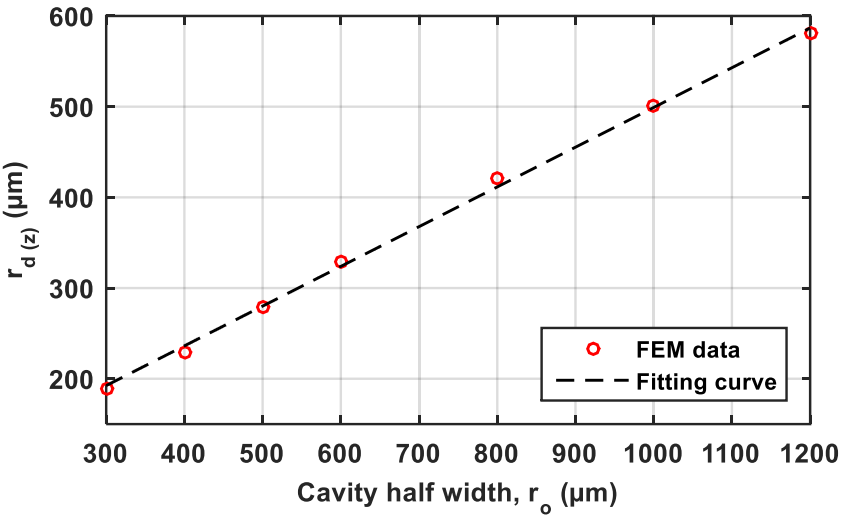

(b)

Figure 4.9. *Optimal detectors locations for (a) in-plane accelerations, $r_{d(x,y)}$, and (b) out-of-plane accelerations, $r_{d(z)}$ vs. bottom cavity half-width r_o.*

Using a linear fit, optimal detector's positions can be expressed by:

$$r_{d(x,y)} = 0.25\,(r_o + 540) \tag{33}$$

$$r_{d(z)} = 0.44\,(r_o + 139) \tag{34}$$

Assuming the optimal positioning of detectors as modeled above, sensitivities for values of r_o from 300µm up to 1200µm have been plotted with respect to sensitivities obtained for r_o=500µm in Figure 4.10 for (a) in-plane and (b) out-of-plane accelerations.

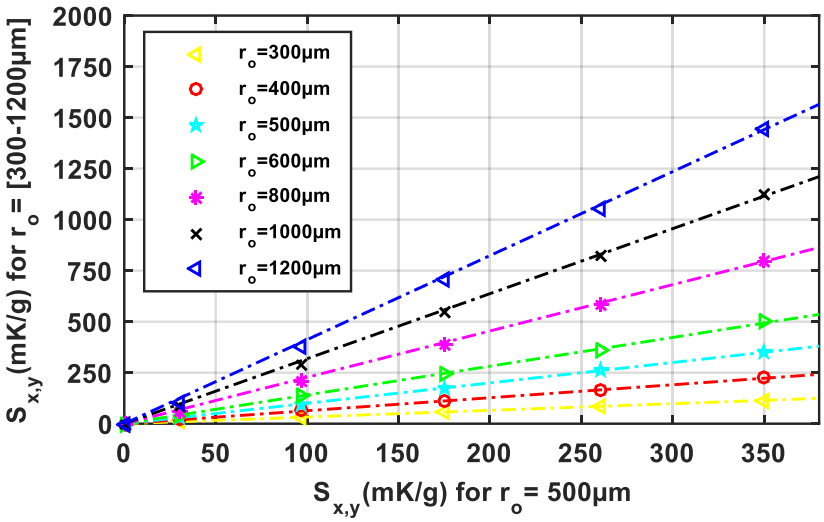

(a)

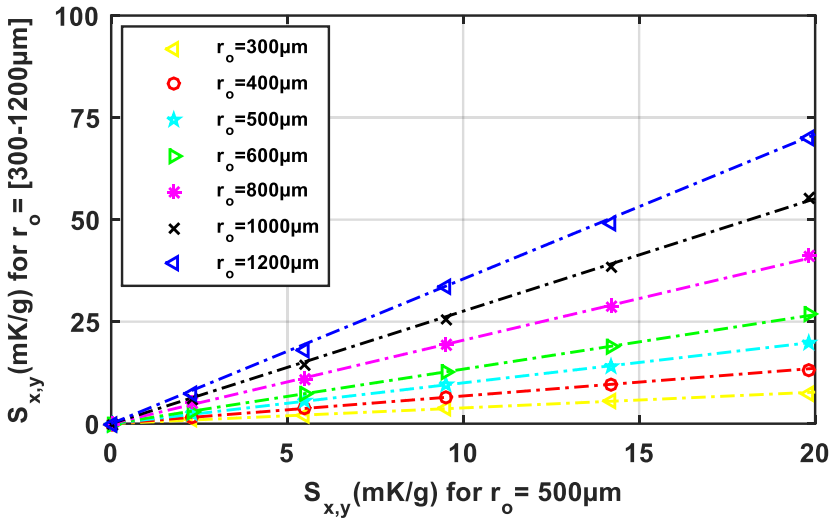

(b)

Figure 4.10. *(a) In-plane and (b) out-of-plane sensitivities for r_0=[300µm-1200µm] vs sensitivity for r_0=500µm.*

These graphs confirm the linear relationship between sensitivity and bottom cavity half-width. Therefore, in-plane and out-of-plane sensitivities can be estimated by a correction factor for each bottom cavity half-width. These factors are obtained by extracting the slope of each linear line, which are then plotted in Figure 4.11 for (a) in-plane and (b) out-of-plane accelerations.

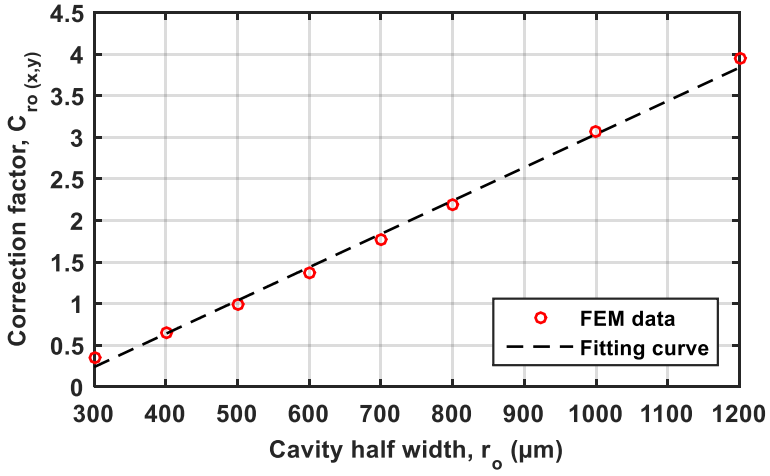

(a)

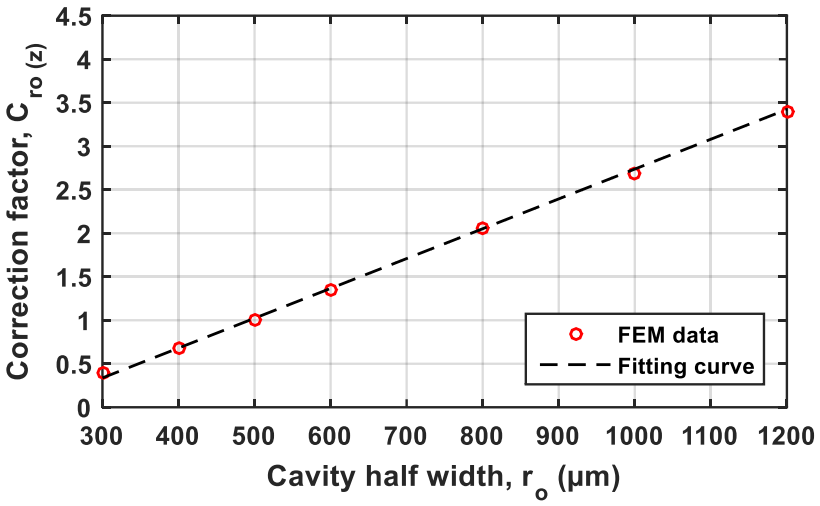

(b)

Figure 4.11. *Correction factor of (a) in-plane and (b) out-of-plane sensitivities vs. bottom cavity half-width.*

From the above, correction factors for in-plane and out-of-plane sensitivities can be determined:

$$C_{ro(x,y)} = 4 \times 10^{-3} (r_o - 240) \quad (35)$$

$$C_{ro(z)} = 3.4 \times 10^{-3} (r_o - 201) \quad (36)$$

4.5 Impact of top cover height

Similarly to previous sections, FEM simulations are performed for various height of the top cavity, h_2, for five pairs of heater temperature and bottom cavity depth ranging from (T_H=400K,

h_1=125µm) up to (T_H=600K, h_1=625µm). In the latter case, temperature profiles along x-axis for different values of h_2 are plotted in Figure 4.12 for (a) in-plane and (b) out-of-plane accelerations.

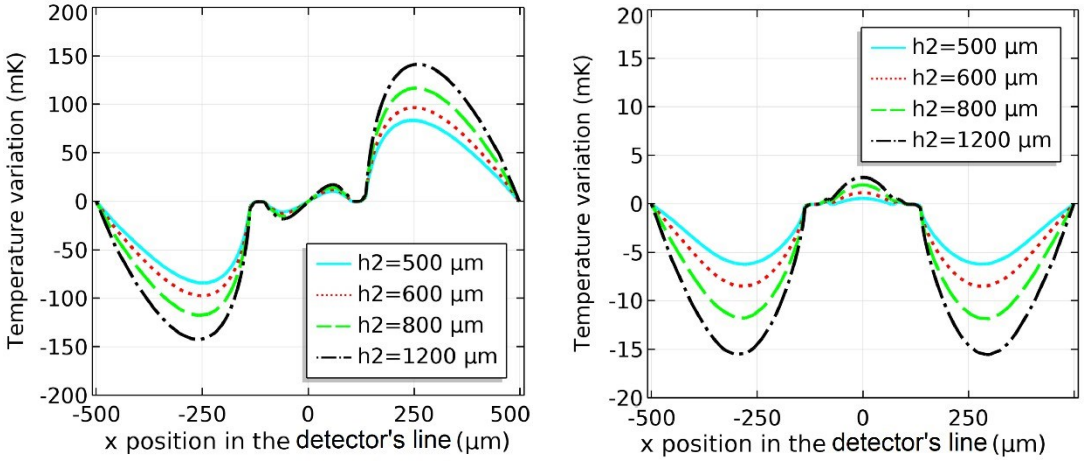

Figure 4.12. *Acceleration-induced temperature variations in the bottom cavity when h_2 equals to 500, 600, 800 and 1200 µm (for T_H = 600 K, h_1 = 625 µm) for (a) 1g in-plane and (b) 1g out-of-plane accelerations.*

For each T_H-h_1 pair, sensitivities for different values of h_2, ranging from 500 µm to 5000 µm, are plotted against sensitivity obtained at nominal h_2=3000µm, in Figure 4.13 for (a) in-plane and (b) out-of-plane accelerations. As expected, linear relationships are obtained and slope can be extracted to obtain correction factors for both in-plane and out-of-plane sensitivities that are reported in Figure 4.14 (a) and (b), respectively.

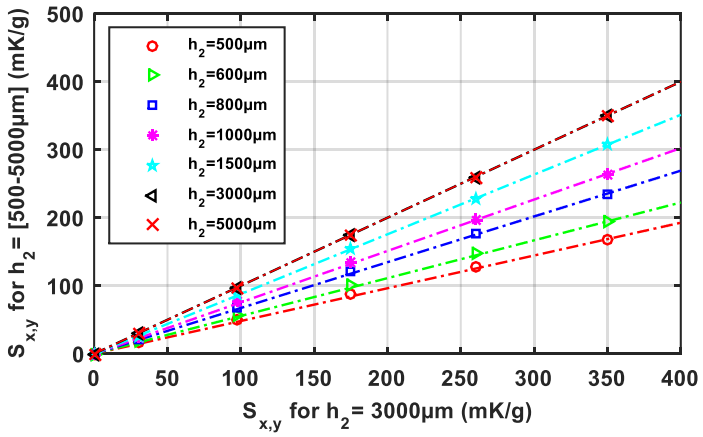

(a)

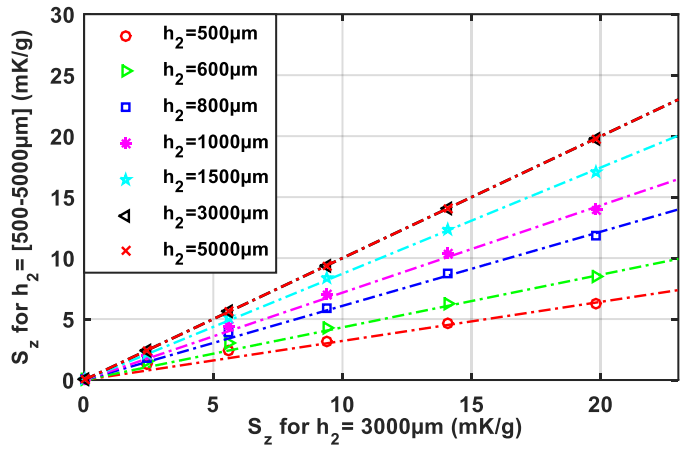

(b)

Figure 4.13. *(a) In-plane and (b) out-of-plane sensitivity readings for h_2 = [500 µm-5000 µm] vs sensitivity readings for h_2 = 3000 µm.*

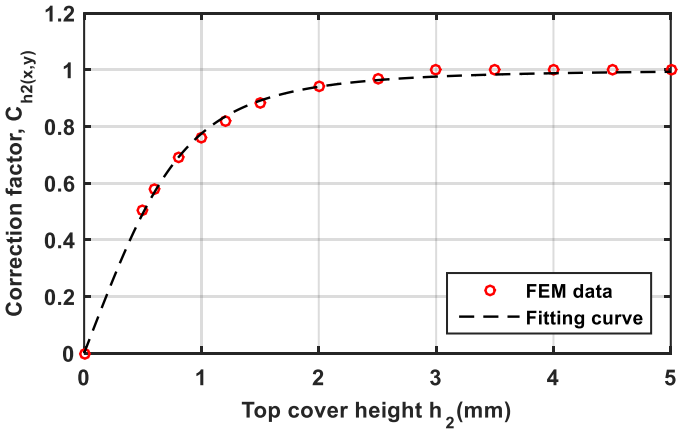

(a)

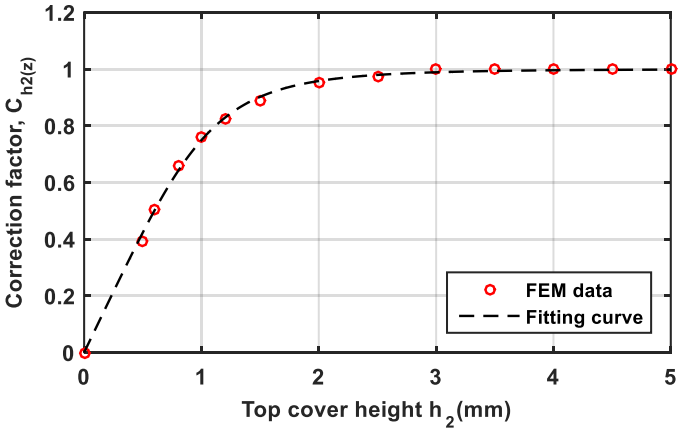

(b)

Figure 4.14. *Correction factors of (a) in-plane and (b) out-of-plane sensitivities vs. top cover height h_2.*

For smaller top cover heights, isotherms are limited and confined. Therefore, accelerations induce small temperature variations thus low sensitivities. For increasing heights, air convection increases along with acceleration-induced temperature variations. Finally, for large top cover heights, hot bubble and convection phenomenon are no longer able to affect temperature close to the top cover and saturation occurs. Observed correction factors can be modeled using the same fitting equation as that of (28). Correction factors for both in-plane and out-of-plane sensitivities with respect to the top cover height h_2 are then given by:

$$C_{h2(x,y)} = \frac{h_2}{\sqrt[2.38]{h_2^{2.38} + 929^{2.38}}} \tag{37}$$

$$C_{h2(z)} = \frac{h_2}{\sqrt[3.4]{h_2^{3.4} + 1163^{3.4}}} \tag{38}$$

4.6 Impact of top cover width

Distance d_2 from the bottom cavity edge to the lateral boundary of the top cavity is the last parameter affecting sensitivity. To include its impact on sensitivity, it is varied in a wide range from 50µm up to 7mm. This leads the total top cavity width, w=2.(d_2+r_0), to range from 1.1mm up to 15mm considering a nominal bottom cavity half-width r_o of 500 µm.

For each value of d_2, both T_H and h_1 are also modified to get five different pairs as in the previous section. For (T_H, h_1)=(600K,1.25r_o), temperature profiles along the x-axis for different values of d_2, are reported in Figure 4.15 for (a) in-plane and (b) out-of-plane accelerations.

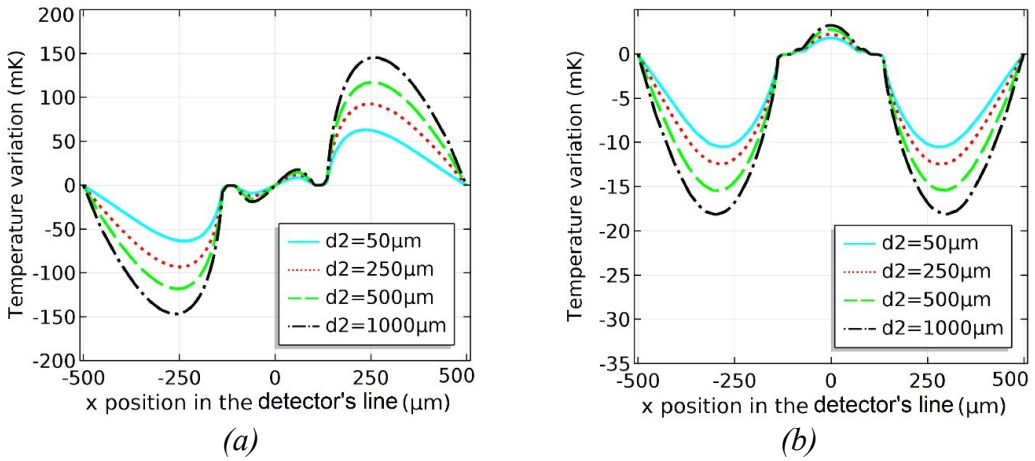

Figure 4.15. *Acceleration-induced temperature variations, in the bottom cavity, for d_2 equals to 50, 250, 500 and 1000 µm, T_H = 600 K, and h_1 = 625 µm along (a) 1g in-plane, and (b) 1g out-of-plane accelerations.*

For each T_H-h_1 pair, sensitivities for different values of d_2, ranging from 50µm up to 7mm, are plotted against sensitivity obtained at nominal d_2=3mm, in Figure 4.16 for (a) in-plane and (b) out-of-plane accelerations. Quasi-linear relationships are obtained and slope can be extracted to obtain correction factors for both in-plane and out-of-plane sensitivities that are reported in Figure 4.17 (a) and (b), respectively.

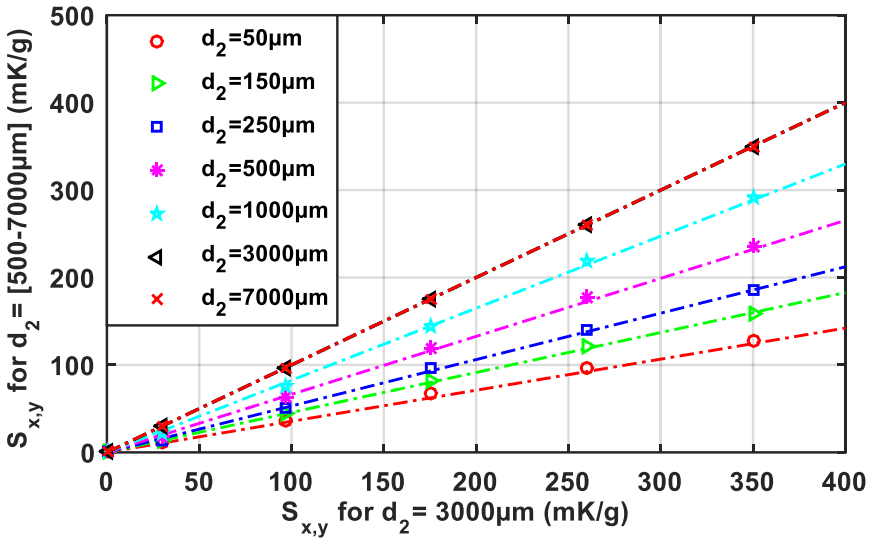

(a)

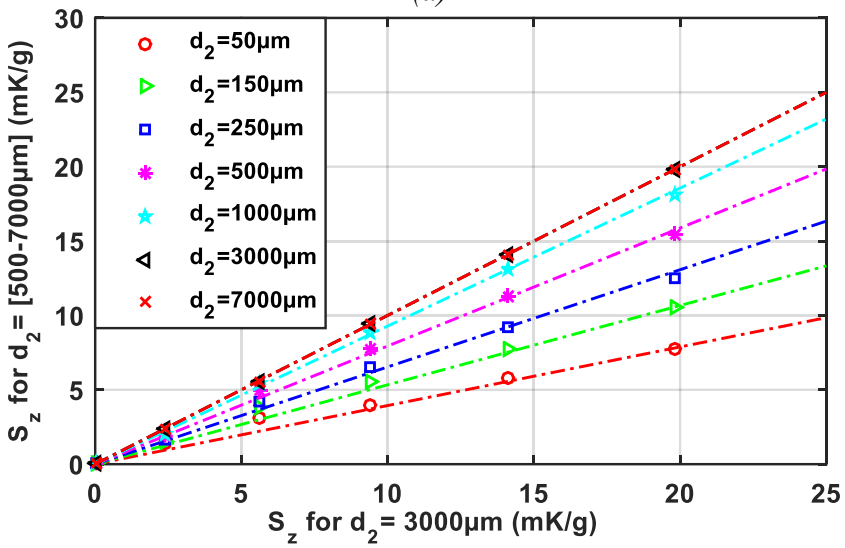

(b)

Figure 4.16. *(a) In-plane and (b) out-of-plane sensitivity readings for d_2 = [50 µm-3000 µm] vs sensitivity readings for d_2 = 3000 µm.*

It appears that both in-plane and out-of-plane sensitivities remain almost constant for distance d_2 higher than 3000 µm. These results are in accordance with those observed for the impact of h_1 and h_2 since the hot bubble shape is affected by the distance to fixed-temperature

boundaries in all directions. However, when the top cover width is high enough, it becomes no longer a limiting factor for the hot bubble size and convection phenomena.

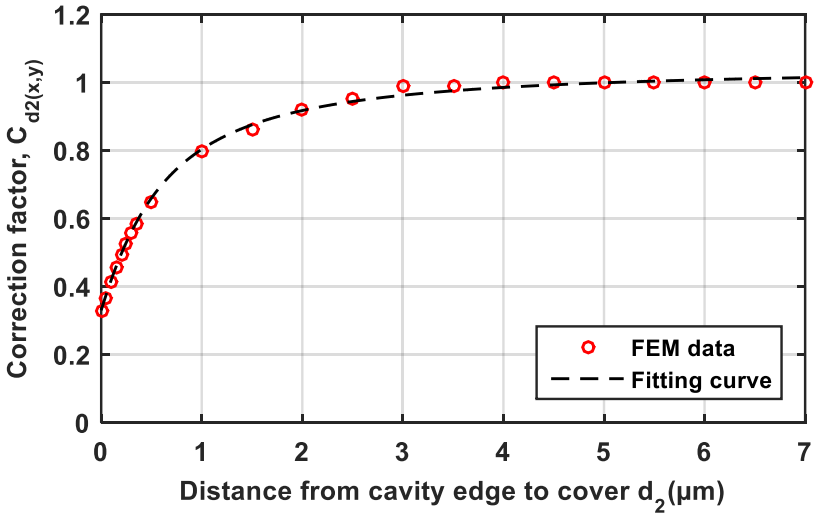

(a)

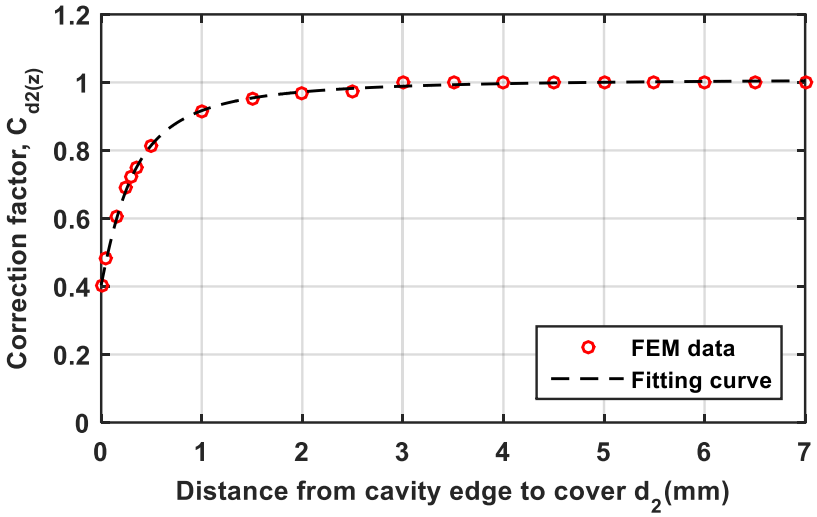

(b)

Figure 4.17. *Correction factors of (a) in-plane and (b) out-of-plane sensitivities vs. distance from bottom cavity edge to top cover edge d_2.*

From Figure 4.17, it appears that, in this case, correction factors are not equal to zero for d_2=0 and therefore, a different expression is proposed to model the attenuation as:

$$C_{d2} = \frac{a\ d_2}{\sqrt[n]{d_2^n + b^n}} + c \tag{39}$$

The dashed curves of Figure 4.17 are obtained by fitting (39) and the so-obtained models for correction factors of sensitivity, with respect to distance d_2, are given by:

$$C_{d2(x,y)} = \frac{0.72\ d_2}{\sqrt[1.2]{d_2^{1.2} + 756^{1.2}}} + 0.33 \tag{40}$$

$$C_{d2(z)} = \frac{0.6\ d_2}{\sqrt[1.5]{d_2^{1.5} + 412^{1.5}}} + 0.41 \tag{41}$$

4.7 Complete model for sensitivity

Expressions of sensitivity are obtained by multiplying the sensitivity as a function of heater temperature T_H (Section 4.2) by correction factors determined in section 4.3 to 4.6 to represent the impact of main geometrical parameters of the microsensor under investigation (i.e., h_1, h_2, r_o and d_2). The so-obtained in-plane and out-of-plane sensitivity expressions are given in (42) and (43) respectively. Obtained sensitivities are in mK/g if temperatures are in K and dimensions (i.e., h_1, h_2, r_o and d_2) are in µm.

Validity of these expressions is limited to half-width cavities r_o higher than 300 µm. For lower r_o values, sensitivities would be very low, especially for out-of-plane accelerations. Moreover, optimal location of detectors in the cavity would not be possible due to technological constraints.

$$S_{(x,y)} = 104 \times 10^{-6}\ (T_H - T_o)^{1.66} \frac{h_1}{\sqrt[5]{h_1^5 + (0.43\ r_o)^5}}\ \frac{h_2}{\sqrt[2.38]{h_2^{2.38} + 929^{2.38}}} \tag{42}$$

$$(r_o - 240)\left(\frac{0.72\ d_2}{\sqrt[1.2]{d_2^{1.2} + 756^{1.2}}} + 0.33\right)$$

$$S_{(z)} = 2.45 \times 10^{-6}\ (T_H - T_o)^{1.8}\ \frac{h_1}{\sqrt[4]{h_1^4 + (0.24\ r_o)^4}}\ \frac{h_2}{\sqrt[3.4]{h_2^{3.4} + 1163^{3.4}}} \tag{43}$$

$$(r_o - 201)\left(\frac{0.6\ d_2}{\sqrt[1.5]{d_2^{1.5} + 412^{1.5}}} + 0.41\right)$$

4.8 Validation of the proposed compact model

Validation of the proposed compact model is necessary to evaluate the impact, on model accuracy, of fitting operations used to parametrize correction factors. For that purpose, we first define a design space for the micro sensor taking into account technological and economical constraints. The design or parametric space is defined as:

- T_H = [350K - 700K],
- h_1 = [100µm - 400µm],
- h_2 = [500µm - 5mm],
- r_o = [400µm - 800µm],
- d_2 = [100µm - 5mm].

To explore this design space, we generate a set of thirty sensors by setting randomly and independently each design parameter. A large range of sensitivity, sensor footprint and power consumption is then covered. Each generated sensor is then simulated using our parametrized FEM model and sensitivities are extracted and compared with compact-model results. These comparisons are presented in Figure 4.18 for (a) in-plane and (b) out-of-plane sensitivities. Discrepancy to the slope equal to 1 never exceeds 9% and it is worth noting that process variations would have a larger impact on sensitivity, thus validating the use of the proposed model for initial design.

To further demonstrate accuracy of the proposed compact model over a large design domain, acceleration-induced temperature variations along the x-axis are plotted in Figure 4.19 for three selected sensors with low, medium or high sensitivity (namely *Sensor 1*, *Sensor 2* and *Sensor 3*). Respective design parameters are listed in Table 4.2. together with optimal position of detectors as a function of bottom cavity half-width r_0, given by (33) and (34). These values are also accurate with respect to FEM simulations reported in Figure 4.19.

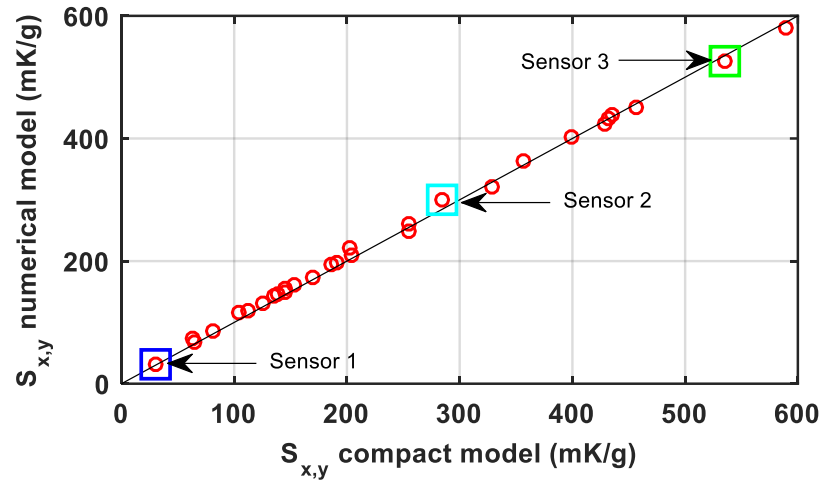

(a)

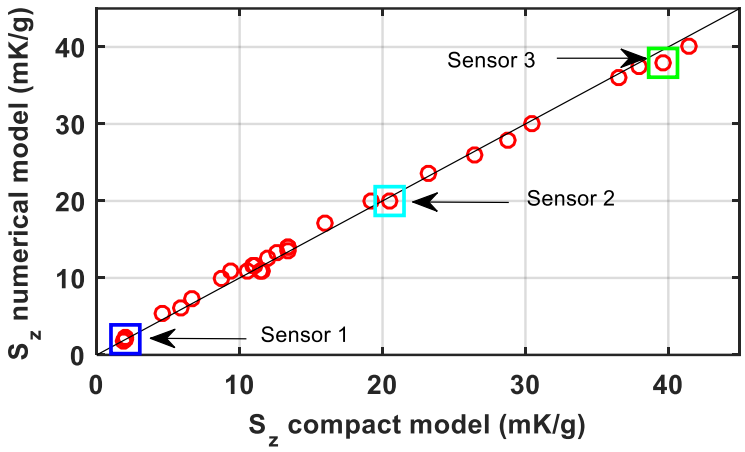

(b)

Figure 4.18. *Sensitivities extracted from FEM simulations as a function of those calculated with the compact model for 30 randomly generated sensors with different design (h_1, h_2, r_o, d_2) and operation (T_H) parameters for (a) in-plane, and (b) out-of-plane accelerations.*

Table 4.2. *Parameter values of Sensor1, Sensor2 and Sensor3 used for validation.*

	T_H	h_1	h_2,	r_o	d_2	$r_{d(x,y)}$	$r_{d(z)}$)
Sensor 1	410	325	1700	430	550	242	250
Sensor 2	608	290	3600	518	870	264	289
Sensor 3	700	300	1000	700	1000	310	369

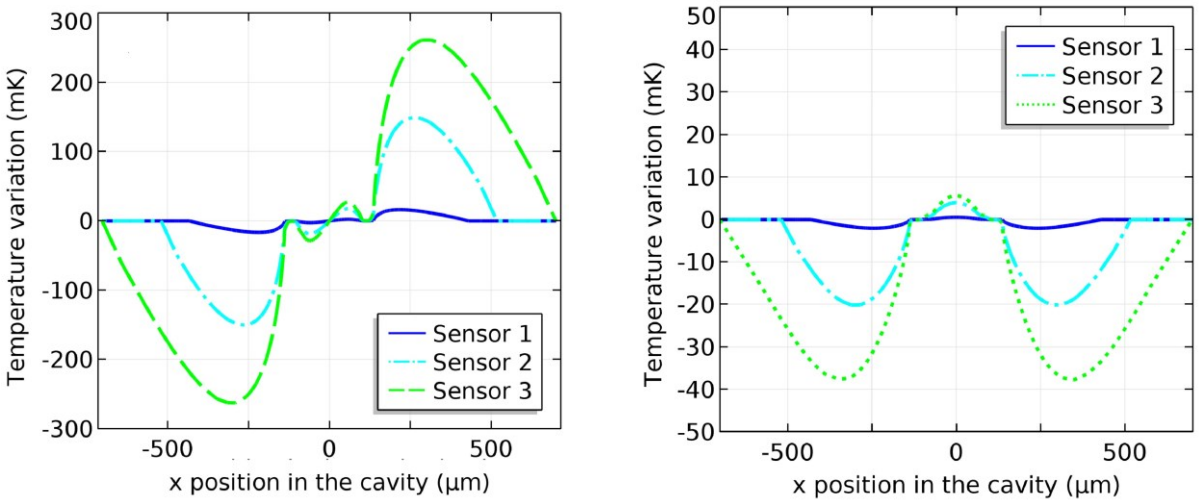

Figure 4.19. *Corresponding acceleration-induced temperature variations, in the bottom cavity of three specific sensors for (a) 1g in-plane and (b) 1g out-of-plane accelerations.*

Conclusion

In this chapter, analytical expressions have been established to predict in-plane and out-of-plane sensitivities of a newly proposed 3-axis micromachined convective accelerometer. Compact model construction relies on the use of FEM-based numerical simulations to extract the dependance of sensitivities on main design parameters. Another important parameter, the heater's temperature, is also considered. This semi-empirical modeling approach is justified by the difficulty in using physical-based analytical models due to the complex geometry of convective accelerometers with several important design parameters and a fundamental three-dimensional behavior. As a result, five parameters are included in the proposed compact model, which include both bottom and top cavity heights and widths in addition to the heating temperature. The proposed compact model is then validated with respect to FEM-based numerical simulations of a random set of thirty sensors with a large range of sensitivities. Thanks to this model, a lot of time and effort, usually put into the development and the simulation of Finite-Element Models to predict in-plane and out-of-plane sensitivities of a convective accelerometer, can be saved to start with an initial device corresponding to specific sensitivity requirements.

The so-obtained design flow consists, first, in defining sensor dimensions to reach the required specification in terms of sensitivity using the developed analytical models. A minimum

set of 3D FEM simulations are then required to successively verify sensitivity, dynamic range, linearity and bandwidth of the sensor.

REFERENCES

Chaehoi A., Conception et Modélisation de MEMS monolithique CMOS en technologie FSBM: Application aux accéléromètres, Thèse de doctorat, Université Montpellier II-Sciences et Techniques du Languedoc, 2005.

Lin L., Jones J., « A liquid-filled buoyancy-driven convective micromachined accelerometer », Journal of microelectromechanical systems, vol. 14, n° 5, 2005, p. 1061-1069.

Mukherjee R., Basu J., Mandal P., Guha PK., « A review of micromachined thermal accelerometers », *Journal of Micromechanics and Microengineering*, vol. 27, n° 12, 2017, p. 123002.

Rekik A., Méthodes alternatives pour le test et la calibration de MEMS: application à un accéléromètre convectif, Thèse de doctorat, Montpellier 2, 2011.

Mezghani B., Brahim A, Tounsi F., Masmoudi M., Rekik AA., Nouet P., « From 2D to 3D FEM simulations of a CMOS MEMS convective accelerometer », *IEEE International Conference on Microelectronics ICM Proceeding,* 2011.

Baglio S., Castorina S., Fortuna L., Savalli N., « Modeling and design of novel photo-thermo-mechanical microactuators », *Sensors and Actuators A: Physical*, vol. 101, n° 1-2, 2002, p. 185-193.

Luo X., Yang Y., Zheng F., Li Z., Guo Z., « An optimized micromachined convective accelerometer with no proof mass *», Journal of Micromechanics and Microengineering*, vol.11, n° 5, 2001 p.504.

Garraud A., Combette P., Gosalbes J., Charlot B., Giani A., « First high-g measurement by thermal accelerometers *», IEEE Solid-State Sensors, Actuators and Microsystems Conference (TRANSDUCERS)*, 2011.

Courteaud J., Crespy N., Combette P., Sorli B., Giani A., « Studies and optimization of the frequency response of a micromachined thermal accelerometer *», Sensors and Actuators A: Physical*, vol, 147, n° 1, 2008, p.75-82.

General conclusion and perspectives

The evolution of the MEMS field over the past two decades, coupled with an increasing demand for inertial sensors, has increased the attention paid to convective sensors. Unlike conventional accelerometers (i.e., capacitive, piezoresistive, piezoelectric), the absence of a proof mass in convective accelerometers simplifies manufacturing, increases shock robustness and CMOS compatibility. As this integration reduces manufacturing costs, at least for large volume production, and increases manufacturing yield and repeatability, it is interesting to develop an efficient 3-axis convective accelerometer compatible with a CMOS process thanks to a post-process, FSBM in our case.

The purpose of this thesis is to improve the very low sensitivity of convective accelerometers while increasing, at the same time, their energy-efficiency. For that, a couple of solutions were studied. Only one of them was compatible with the targeted manufacturing process: a standard CMOS die post-processed by FSBM. We then propose design modifications to improve sensitivity in all three axis with an improved energy-efficiency.

Major contributions of this research work are:

- A mechanical solution has been proposed to improve out-of-plane sensitivity of a three-axis convective accelerometer by assuring a vertical displacement of the heater plate when submitted to z-axis accelerations. This solution has been presented and analyzed using Fine Element Analyses. Important improvements in terms of out-of-plane sensitivity were found, but technological limitations within CMOS 0.35µm technology and FSBM post-process prevented the implementation of the solution.
- A novel 3-axis accelerometer, compliant with FSBM post-process and a 0.35µm CMOS technology, have been proposed. Main improvements, with respect to the reference device consist on a large range of possible sensitivities by adjusting the power dissipation and increasing the maximum sensitivities around 4 times and 3 times for in-plane and out-of-plane accelerations respectively.
- An optimized heater shape has been proposed to increase sensitivity and to decrease power consumption; thus, improving overall energy efficiency of the device. Layout of the device, including the electronics and conditioning circuit, has been detailed and a prototype has been fabricated, using a 0.35µm CMOS technology followed by FSBM post-process.

- Analytical expressions have been established to predict in-plane and out-of-plane sensitivities of the proposed 3-axis micromachined convective accelerometer. To overcome time-consuming simulations of 3D FEM models due to the complex geometry of convective accelerometers, we have proposed a compact model that will allow fast device design corresponding to specific sensitivity and power requirements.

In the close future, it would be interesting to characterize the fabricated sensor and to use experimental results to validate both numerical and analytical models presented in this thesis. Another interesting idea is to extend the application of the mixed modeling approach from convective accelerometer to other types of sensors in order to extract an expression of sensitivity as a function of different geometrical parameters.

Résumé

1. Introduction

Dans un accéléromètre convectif, la masse sismique généralement utilisée est remplacée par un volume de gaz chauffé. La structure de cet accéléromètre est généralement composée d'une cavité, d'un élément chauffant suspendu dans la cavité et de détecteurs placés symétriquement par rapport à l'élément chauffant. Une fois la résistance chauffante alimentée, un gradient de température symétrique est généré en créant une distribution de température assimilable à une bulle thermique, comme présentée dans la Figure 1. Lorsqu'une accélération est appliquée dans le plan, le gradient de température devient asymétrique. La bulle thermique se déplace ainsi dans le sens de l'accélération grâce aux forces naturelles de convection. Les détecteurs mesurent une variation de résistance induite par une variation de température proportionnelle à l'accélération appliquée.

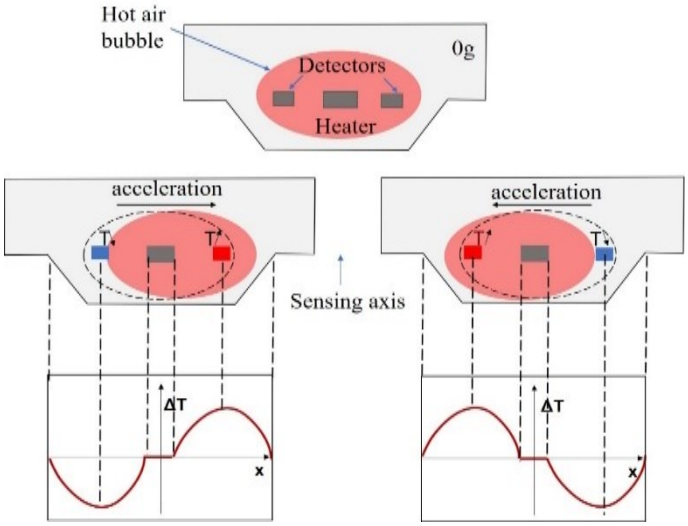

Figure 1. *Représentation du principe de fonctionnement de l'accéléromètre convectif suite à une accélération latérale.*

L'utilisation de la technologie CMOS pour la fabrication des accéléromètres convectifs a l'avantage de réduire leur coût de fabrication, leur taille et leur niveau du bruit du fait de la proximité de l'étage d'amplification. Par contre, cette technologie impose plusieurs contraintes qui peuvent limiter leurs performances. Parmi ces limitations, on peut citer le processus de fabrication et notamment, les propriétés des matériaux, les épaisseurs des couches minces, les largeurs et les espacements minimaux imposés par la technologie. De même, la taille de la cavité, qui affecte fortement la sensibilité de l'accéléromètre, est limitée par l'épaisseur du substrat et la vitesse de gravure du silicium. Cependant, s'il est aisé de faire un accéléromètre convectifs 2 axes en technologie CMOS, le défi le plus important reste l'intégration d'un

troisième axe mesurant l'accélération hors plan. Ceci nécessite a priori une structure tridimensionnelle, peu compatible avec la planéité de la technologie. Un accéléromètre triaxial avec une structure bidimensionnelle a ainsi été proposé par le LIRMM dans une thèse précédente, mais les sensibilités, surtout hors-plan, étaient très faibles (Nguyen 2013).

L'objectif de cette thèse est donc l'amélioration des performances de cet accéléromètre convectif triaxial, et tout particulièrement de sa sensibilité hors-plan. Pour cela, deux solutions sont proposées et étudiées à l'aide d'une modélisation par éléments finis (FEM). La solution la plus adéquate est ensuite optimisée. Finalement, une expression analytique de la sensibilité dans les trois axes, en fonction des paramètres clés de l'accéléromètre est développée et validée.

2. Solutions proposées pour l'amélioration des performances

2.1. Solution mécanique pour l'amélioration de la sensibilité

Cette solution repose sur l'augmentation de la variation de température grâce à une solution mécanique permettant de déplacer l'élément chauffant verticalement sous l'effet d'accélérations hors plan. Cette solution peut être implémentée à l'aide de bras de suspension flexibles connectant l'élément chauffant avec le substrat comme présenté dans Figure 2. En appliquant une accélération verticale, l'élément chauffant et la bulle thermique s'éloignent des détecteurs latéraux immobiles dans la direction opposée à l'accélération, ce qui induit une augmentation de la variation de température.

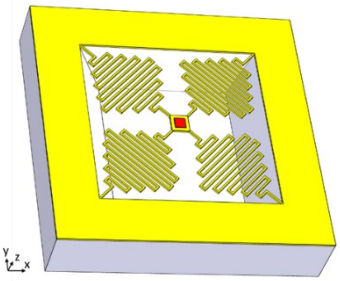

Figure 2. *Design proposé de l'accéléromètre convectif triaxial avec des bras flexibles.*

Différents designs sont simulés afin de déterminer l'emplacement optimal des détecteurs :

- Design1 : Composé de l'élément chauffant avec des bras d'attachement rigides.
- Design2 : Composé de l'élément chauffant avec des bras d'attachement flexibles.
- Design3 : Composé de l'élément chauffant avec une masse sismique au-dessus, et des bras d'attachement flexibles.

Les résultats de simulations montrent que les sensibilités du Design1 et Design2 sont comparables pour des détecteurs placés à mi-distance entre l'élément chauffant et le bord du

substrat. Par contre, une augmentation importante de la sensibilité du Design2 est observée près de l'élément chauffant. En effet, à une distance de 10µm de l'élément chauffant, la sensibilité du Design2 est 5 fois plus importante que celle du Design1. La sensibilité diminue en s'éloignant de l'élément chauffant, comme le montre la Figure 3(a).

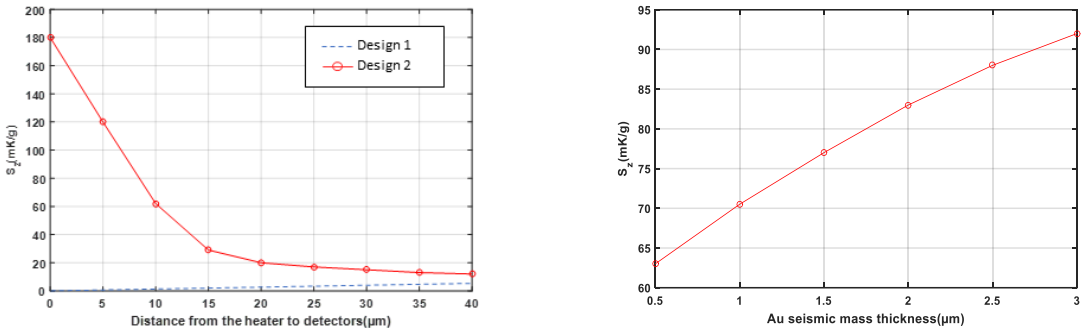

(a) *(b)*

Figure 3. *Valeurs de s*ensibilité *hors-plan simulées en fonction de (a) la distance entre le détecteur et l'élément chauffant pour Design1 et Design2 et (b) l'épaisseur de la masse pour Design3 (pour une distance de 10 µm)*

L'ajout d'une masse sismique en or au-dessus de l'élément chauffant augmente la sensibilité hors plan comme le montre la Figure 3(b) qui présente la sensibilité à 10 µm en fonction de l'épaisseur de la masse sismique ajoutée. Cependant, l'ajout de cette masse sismique nécessiterait des étapes de fabrication supplémentaires qui ne sont pas proposées par le fondeur. De plus, lors de l'étude de cette solution mécanique en technologie CMOS, il est apparu que les règles de design de la technologie utilisée imposent une distance minimale entre l'élément chauffant et les détecteurs de 40 µm. A cette distance, un tel accéléromètre a malheureusement une sensibilité hors-plan pratiquement similaire à celle d'un accéléromètre triaxial classique. Ainsi, cette solution a été abandonnée et nous avons donc cherché à optimiser le design de l'accéléromètre convectif existant (*Nguyen, Mailly et al. 2015)*.

2.2. Amélioration de l'efficacité d'un accéléromètre existant

Un modèle FEM 3D est développé en remédiant à quelques simplifications généralement utilisées dans les modélisations de l'accéléromètre convectif, notamment la considération de l'élément chauffant comme un plateau en SiO_2 ayant une temperature fixe. Une comparaison entre les résultats de simulations et les résultats expérimentaux, en termes de sensibilités, montre une marge d'erreur relative maximale de 17%. Cette marge est considérée acceptable et valide le modèle numérique développé.

Ce modèle est utilisé afin d'optimiser le design de l'accéléromètre convectif triaxial existant en modifiant la taille et la forme de l'élément chauffant. Pour comparer les performances des différentes formes et tailles des éléments chauffants, l'efficacité est définie comme le rapport entre la sensibilité et la puissance consommée. Quartes formes d'éléments chauffants, présentées dans la Figure 4, sont initialement proposées :

- Square60 et Square100 : orienté à 45°, avec une forme carrée de 60µm et 100µm de côté, respectivement.
- Quadruple : basé sur le même plateau que le Square100, les 4 micro-résistances sont distribuées sur les coins.
- Wings : le plateau est remplacé par un cadre de 150µm de côté, avec des extensions (wings) embarquant les quatre micro-résistances.

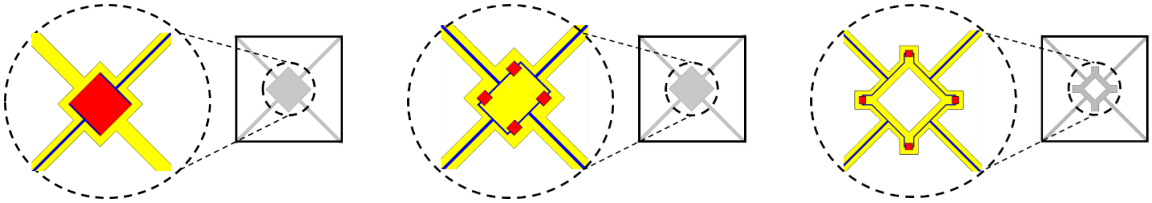

(a) *(b)* *(c)*

Figure 4. *Détails des éléments chauffants proposés (a) Square60 and Square100, (b) Quadruple, et (c) Wings.*

Les résultats de simulations, présentés dans la Figure 5, ont montré la supériorité de la sensibilité et l'efficacité du design Wings dans les trois directions, principalement parce qu'il permet de dissiper plus de puissance pour une température maximale donnée (700K dans le cas présent). Ce design sera donc étudié afin de concevoir un accéléromètre convectif triaxial.

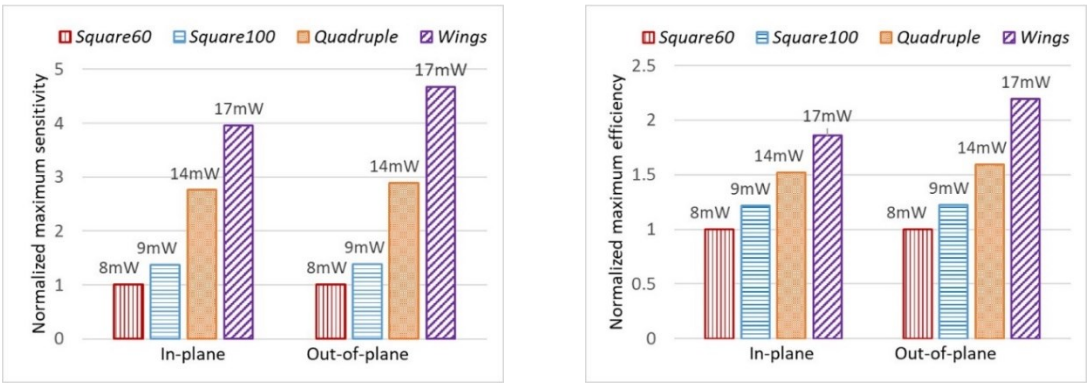

(a) *(b)*

Figure 5. *Comparaison entre les quatre designs proposés de l'élément chauffant pour des accélérations dans-le-plan et hors-plan en termes de (a) sensibilité maximale et (b) efficacité maximale. Les données sont normalisées à 1 pour Square60.*

3. Développement d'un nouvel accéléromètre convectif triaxial CMOS avec une efficacité améliorée

3.1. Optimization de l'élément chauffant

Les Figures 6(a) et (b) montrent une vue générale et une vue détaillée de l'élément chauffant et ses bras de suspension. L'optimisation de l'élément chauffant est faite en optimisant les deux paramètres clés a et d. Initialement, les paramètres b, c et d sont fixés arbitrairement. Tous les autres paramètres sont fixés aux valeurs minimales permises par la technologie de fabrication (Tableau 1).

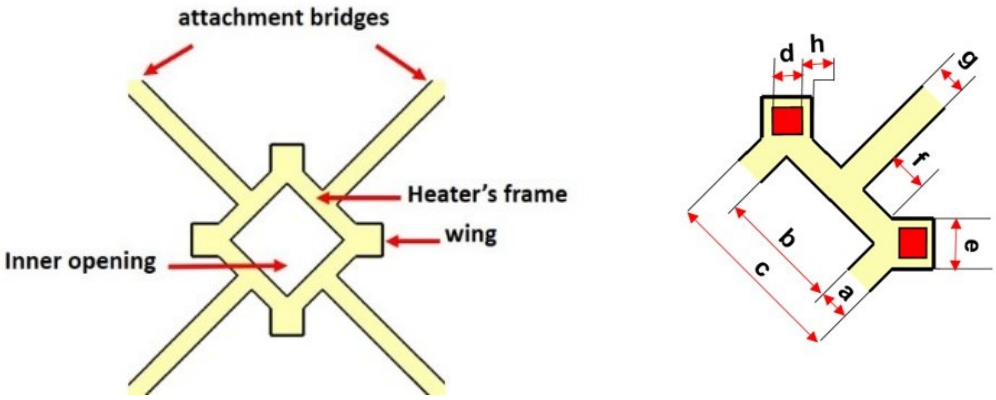

(a) *(b)*

Figure 6. *Vue (a) générale et (b) détaillée de l'élément chauffant proposé et ses quatre bras de suspension.*

Tableau 1. *Paramètres géométriques clés de l'élément chauffant et ses valeurs nominales.*

Symbole	Description	Valeur (µm)
a	Largeur du cadre de l'élément chauffant connectant les quatre résistances	25
b	Longueur de l'ouverture interne.	100
c	Longueur du cadre de l'élément chauffant	150
d	Longueur de la résistance chauffante	15
e	Longueur du wing	41
f	Distance entre le wing et son bras de fixation.	35
g	Largeur du pont de fixation	25
h	Largeur de l'encapsulation en SiO_2 autour de la résistance chauffante	13

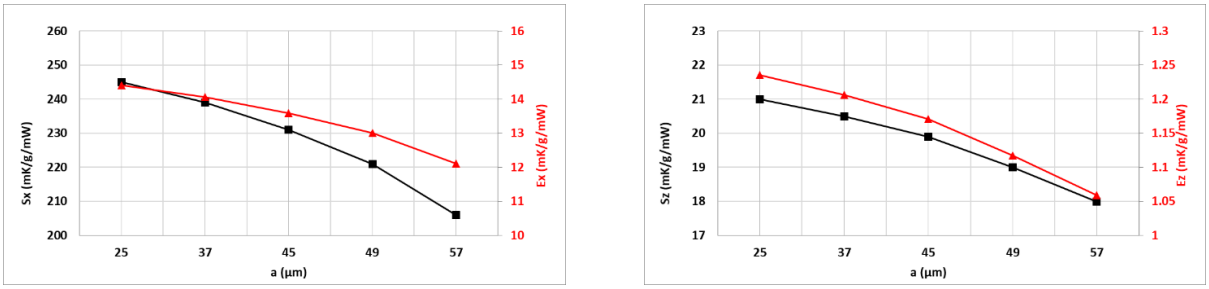

(a) *(b)*

Figure 7. *Sensibilités (a) dans le plan et (b) hors plan et efficacités correspondantes pour différentes valeurs de 'a' et une puissance de chauffage de 17 mW.*

Dans une première étape, le paramètre *a* est optimisé. Pour cela, les sensibilités et efficacités, dans le plan et hors plan, sont tracées en fonction des différentes valeurs de *a* dans les Figure7 (a) et (b), respectivement. Ces figures montrent que le rendement du capteur diminue en fonction de la largeur du cadre a. Pour cela, les paramètres *a*, *d*, *e*, *f*, *g* et *h* sont maintenus à leurs valeurs minimales mentionnées dans le Tableau 1.

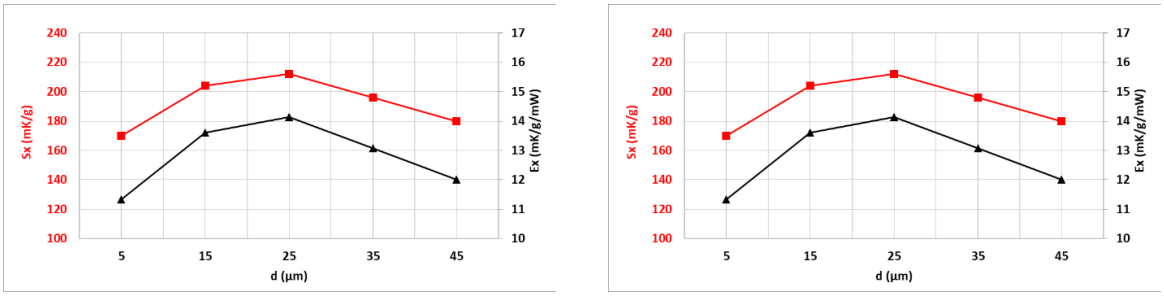

(a) *(b)*

Figure 8. *Sensibilités (a) dans le plan et (b) hors plan et efficacités correspondantes pour différentes valeurs de 'd' et une puissance de chauffage de 15 mW.*

Dans une deuxième étape, le paramètre *d* est étudié. Les mêmes résultats de simulation en fonction du paramètre *d* sont présentés dans les Figure 8(a) et (b). Ces figures montrent que la valeur optimale pour *d* est de 25µm environ. Pour *d*=5µm, les micro-résistances sont assez petites et génèrent des isothermes de diamètre réduit conduisant à de faibles valeurs de sensibilité et d'efficacité. Pour *d*=45µm, c'est la température maximale atteinte qui est réduite à cause de la grande taille des résistances, ce qui conduit à de faibles sensibilité et efficacité.

3.2. Détecteurs de température pour optimiser l'efficacité

Selon les simulations, les positions optimales pour les détecteurs sont situées à 260µm du centre de la cavité (pour une accélération dans le plan) et 280µm (hors-plan). En se basant sur

ces résultats, quatre designs de bras détecteurs, présentés dans la Figure 9, sont proposés. Les sensibilités obtenues par simulations pour chaque design sont présentées dans le Tableau 2.

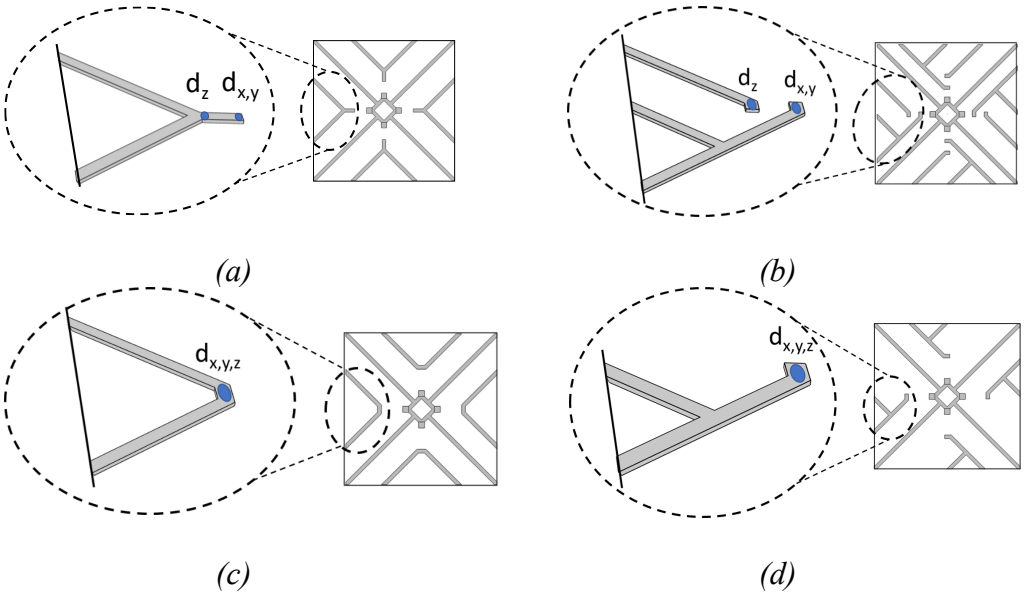

Figure 9. (a) *Design1, (b) Design2, (c) Design3 et (d) Design4 des bras détecteurs proposés.*

Tableau 2. *Sensibilités dans le plan et hors-plan issues des simulations des différents designs des ponts détecteurs avec une puissance de chauffage de 15 mW.*

	$S_{x,y}$ (mK/g)	S_z (mK/g)
Design1	169	12
Design2	146	10
Design3	167	12.5
Design4	178	13.5

Les résultats des simulations montrent que le Design 4 délivre les meilleures sensibilités puisqu'il possède le volume minimal de matière et minimise ainsi la conduction thermique. Ce design de détecteur est donc choisi et une vue 3D de l'accéléromètre convectif à 3 axes proposé, avec l'élément chauffant et bras détecteurs optimisés, est présentée dans la Figure 10.

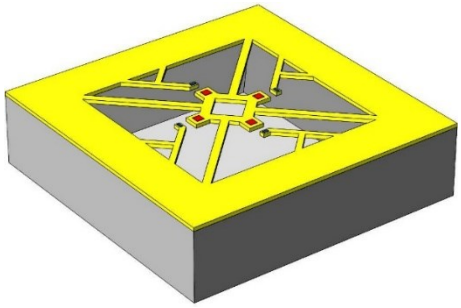

Figure 10. *Vue 3D de l'accéléromètre convectif triaxial optimisé.*

3.3. Evaluations des résultats

En comparant les performances de l'accéléromètre convectif développé avec l'accéléromètre de la littérature (Mailly, Nguyen et al. 2014), plusieurs améliorations sont notées :

- En termes de puissance maximale, l'accéléromètre optimisé permet de doubler la puissance du chauffage pour atteindre la température maximale autorisée (700K). Cette température est ainsi obtenue avec une puissance de 19mW pour le design optimisé, contre seulement 9mW pour le design initial. Cette augmentation de puissance maximale est un avantage car elle a un impact direct sur la sensibilité.

- En termes de sensibilité, des augmentations de 31% et 71% sont observées pour les sensibilités dans le plan et hors-plan, respectivement, dans une plage de puissance de chauffage comprise entre 7mW et 9mW. Puisque la plage de puissance de fonctionnement augmente pour l'accéléromètre optimisé, les sensibilités maximales peuvent être multipliées d'un facteur quatre dans le plan, et de plus de cinq hors-plan.

- En termes d'efficacité, les efficacités maximales dans le plan et hors-plan du design optimisé sont de l'ordre de 2 et 2,5 fois plus grandes que celles du design initial.

3.4. Implémentation CMOS

L'accéléromètre convectif triaxial proposé est destiné à exploiter la technologie CMOS. Afin d'atteindre la température souhaitée, quatre résistances de chauffage en *PolyH* de 1kΩ sont montées en parallèle. D'après les simulations, la puissance nécessaire pour atteindre une température de chauffage de 700K est alors de 19 mW, ce qui correspond à une tension de 2,18V et un courant total de 8,72mA (soit 2,18mA pour chaque résistance). De plus, quatre résistances de 400Ω en *Poly1* sont montées en série afin de mesurer la température de chauffage moyenne. Les résistances de détection sont embarquées à l'extrémité des bras détecteurs. Chaque bras accueille ainsi 3 résistances : deux résistances de 2,5kΩ pour les mesures de température différentielle dues aux accélérations dans le plan (axe x et y), et une résistance de 1,25kΩ pour la mesure de la variation de la température de mode commun induite par les accélérations hors-plan (axe z). Les 4 résistances de l'axe z sont connectées en série par paires sur les axes x et y afin d'être insensibles aux accélérations dans le plan.

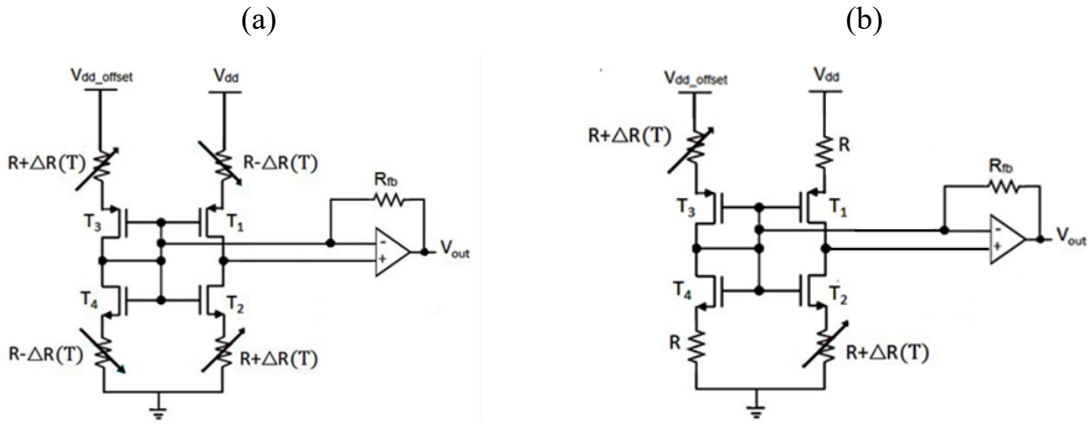

Figure 11. *Circuit de conditionnement pour la détection des accélérations (a)dans le plan et (b) hors-plan.*

Pour le conditionnement, un pont actif complet (Boujamaa, Dumas et al. 2009), un amplificateur opérationnel et une résistance de contre-réaction, sont utilisés pour chacun des axes x et y. Par contre, un demi pont actif est utilisé pour l'axe z vu que toutes les résistances de détection varient avec le même signe. Les architectures des circuits de conditionnement utilisés pour l'axe x (et y) et l'axe z sont ainsi présentées dans les Figure 11(a) et (b) respectivement. Les Figures 12(a) et (b) montrent le prototype fabriqué avant et après la réalisation du processus de gravure.

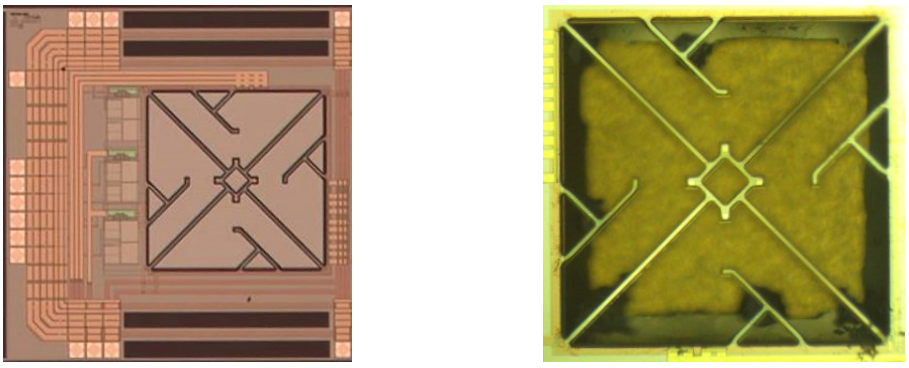

(a) *(b)*

Figure 12. *Image de l'accéléromètre 3D (a) avant et (b) après la gravure FSBM.*

4. Modélisation analytique/numérique d'accéléromètre convectif triaxial CMOS

Un modèle compact analytique/numérique, qui décrit la sensibilité du capteur en fonction des principaux paramètres, est établi. Ces paramètres sont la température de chauffe T_H, la hauteur de la cavité h_1, la hauteur du capot h_2, la demi largeur de la cavité r_o et la demi largeur

du capot d_2. Une coupe transversale de l'accéléromètre, avec les principaux paramètres géométriques est présentée dans la Figure 13. Les valeurs nominales de ces paramètres sont listées dans le Tableau 3. Ces valeurs sont celles conduisant à une sensibilité maximale pour une valeur nominale de r_o de 500µm.

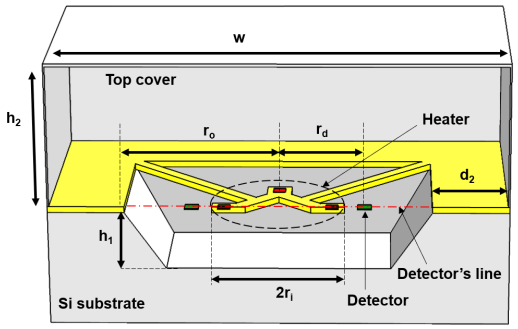

Figure 13. *Vue en coupe transversale de l'accéléromètre convectif étudié avec les principaux paramètres géométriques.*

Tableau 3. *Liste des paramètres de l'accéléromètre et de leurs valeurs nominales*

Symbol	Description	Valeur
r_i	Demi largeur de l'élément chauffant	135 µm
r_o	Demi largeur de la cavité	500 µm
$r_{d(x,y)}$	Position optimale des détecteurs dans le plan	260 µm
$r_{d(z)}$	Position optimale des détecteurs hors-plan	280 µm
h_1	Hauteur de la cavité	700 µm
h_2	Hauteur du capot	3 mm
d_2	Distance entre le bord de la cavité et l'extrémité du capot	3 mm
w	Largeur du capot = 2 (r_o + d_2)	7 mm

4.1. Effet de la température de chauffe

Afin de déduire l'expression de la sensibilité en fonction de la température de chauffe, cette dernière est modifiée entre 300K et 700K en gardant tous les autres paramètres géométriques à leurs valeurs nominales. Les Figures 14(a) et (b) présentent, respectivement, les sensibilités dans le plan et hors plan en fonction de la différence de température entre l'élément chauffant et le substrat.

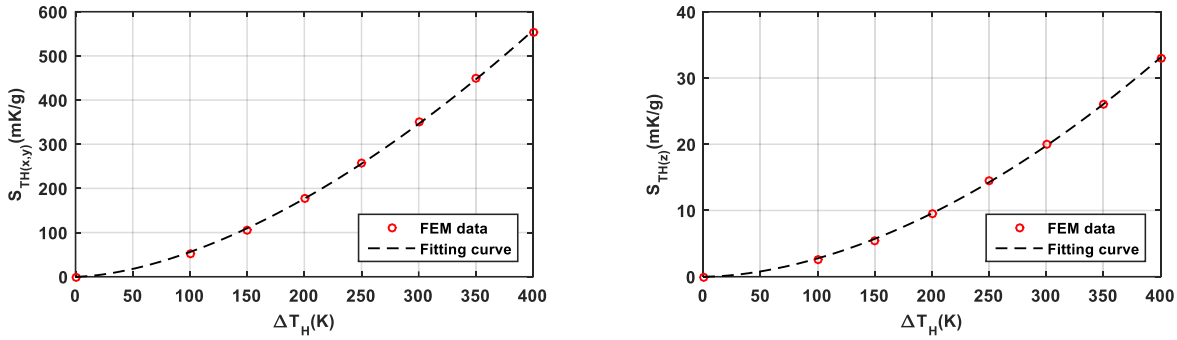

(a) *(b)*

Figure 14. *Sensibilités (a) dans le plan et (b) hors-plan en fonction de la différence de température entre l'élément chauffant et le substrat.*

Ces figures montrent une croissance exponentielle de la sensibilité. Un fitting des deux courbes est réalisé afin de déduire les expressions des sensibilités dans le plan et hors plan en fonction de la température de chauffe :

$$S_{T_H(x,y)} = 0.026\,(T_H - T_o)^{1.66} \quad (1) \qquad S_{T_H(z)} = 0.72 \times 10^{-3}\,(T_H - T_o)^{1.8} \quad (2)$$

4.2. Effet de la hauteur de la cavité

Pour chaque valeur de h_1, de 50 à 700µm (par pas de 50µm), les sensibilités sont estimées par simulation sur une plage de température de chauffe de 350 à 700 K. A partir de ces résultats, on déduit des facteurs de correction des sensibilités relatifs à h_1. Ces facteurs sont tracés en fonction de h_1 dans les Figures 15(a) et (b) pour des accélérations dans le plan et hors plan, respectivement.

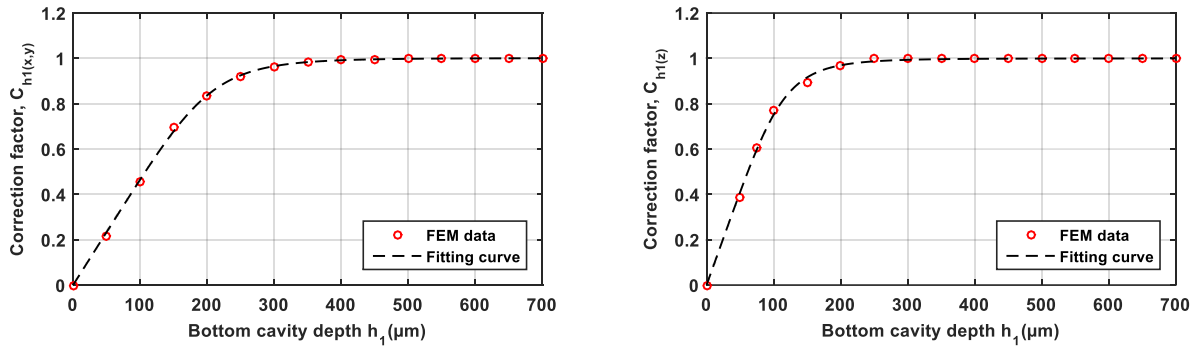

(a) *(b)*

Figure 15. *Facteurs de correction des sensibilités (a) dans le plan et (b) hors plan en fonction de la profondeur de la cavité h_1*

Un fitting des deux courbes permet d'obtenir les équations des facteurs de corrections relatives à h_1 :

$$C_{h1(x,y)} = \frac{h_1}{\sqrt[5]{h_1^5 + (0.43\, r_o)^5}} \quad (3) \qquad C_{h1(z)} = \frac{h_1}{\sqrt[4]{h_1^4 + (0.24\, r_o)^4}} \quad (4)$$

4.3. Largueur de la cavité

Pour la largeur de la cavité, les simulations sont faites, pour chaque valeur de r_o entre 400 et 1200µm, et pour différentes paires de paramètres (T_H, h_1) comme suit : (400K, 0.25 r_o), (450K, 0.5 r_o), (500K, 0.75 r_o), (550K, r_o), (600K, 1.25 r_o) où h_1 est exprimé en fonction de r_o. A partir des résultats de simulation, les facteurs de correction des sensibilités relatifs à r_o sont déduits et tracés dans les Figures 16(a) et (b) pour les accélérations dans le plan et hors plan, respectivement.

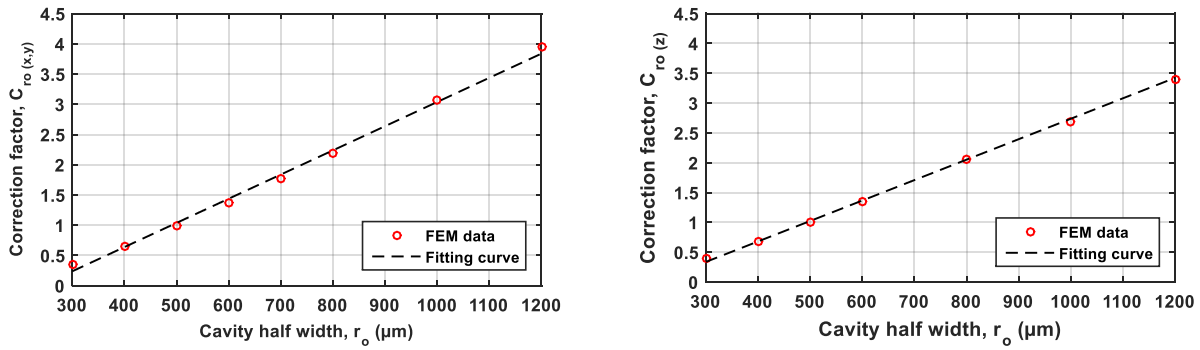

(a) *(b)*

Figure 16. *Facteurs de correction des sensibilités (a) dans le plan et (b) hors-plan en fonction de la demi-largeur de la cavité r_o.*

Un fitting de ces deux courbes permet d'extraire les facteurs de correction ci-dessous :

$$C_{ro(x,y)} = 4 \times 10^{-3}\,(r_o - 240) \quad (5) \qquad C_{ro(z)} = 3.4 \times 10^{-3}\,(r_o - 201) \quad (6)$$

4.4. Effet de la hauteur du capot

Les simulations sont effectuées sur différentes valeurs de h_2 allant de 0 à 5mm pour cinq paires de paramètres (T_H, h_1). Les facteurs de correction relatifs à h_2 sont extraits des résultats de simulation et tracés dans les Figures 17(a) et (b) pour une accélération dans le plan et hors plan, respectivement.

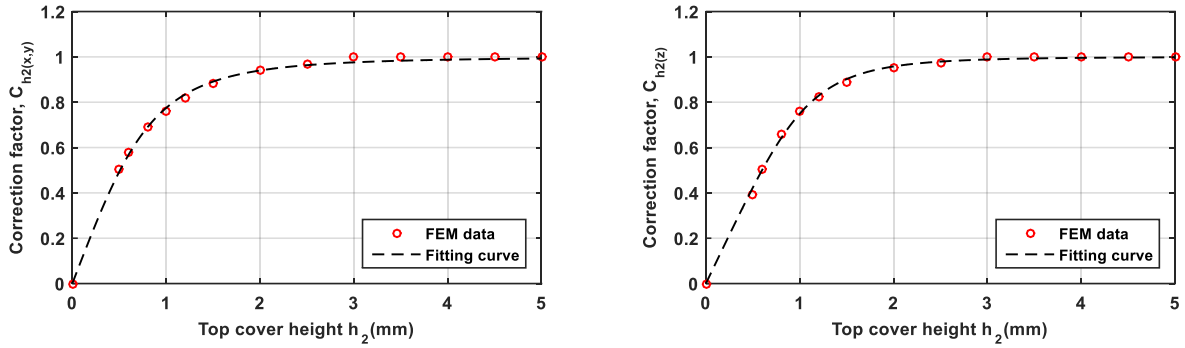

Figure 17. *Facteurs de correction des sensibilités (a) dans le plan et (b) hors-plan vs la hauteur du capot h_2.*

A partir de ces courbes, les facteurs des correction relatifs à h_2 ci-dessous sont extraits :

$$C_{h2(x,y)} = \frac{h_2}{\sqrt[2.38]{h_2^{2.38} + 929^{2.38}}} \quad (7) \qquad C_{h2(z)} = \frac{h_2}{\sqrt[3.4]{h_2^{3.4} + 1163^{3.4}}} \quad (8)$$

4.5. Effet de la largeur du capot

Le dernier paramètre à étudier est d_2, la distance entre le bord de la cavité et le côté du capot. Pour cela, cinq paires de paramètres (T_H, h_1) sont simulés pour chaque valeur de d_2, allant de 0 à 7mm. Les facteurs de correction relatifs à d_2 sont ensuite déduits et tracés respectivement dans les Figures 18(a) et(b) pour une accélération dans le plan et hors plan.

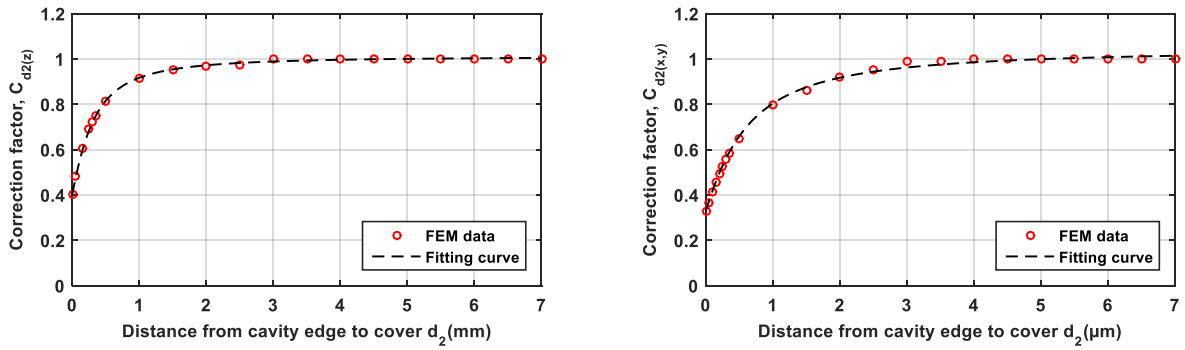

Figure 18. *Facteurs de correction des sensibilités (a) dans le plan et (b) hors plan en fonction de la distance entre le bord de la cavité et le bord du capot d_2.*

Les équations suivantes, obtenues par fitting des données des Figures 18(a) et(b), modélisent les facteurs de corrections relatifs à d_2 :

$$C_{d2(x,y)} = \frac{0.72\, d_2}{\sqrt[1.2]{d_2^{1.2} + 756^{1.2}}} + 0.33 \quad (9) \qquad C_{d2(z)} = \frac{0.6\, d_2}{\sqrt[1.5]{d_2^{1.5} + 412^{1.5}}} + 0.41 \quad (10)$$

4.6. Modèle complet de la sensibilité

En multipliant l'expression de la sensibilité en fonction de T_H par les facteurs de correction relatifs aux différents paramètres, des modèles compacts des sensibilités dans le plan et hors plan, valides pour des valeurs de r_o supérieures à 300µm, sont obtenues :

$$S_{(x,y)} = 104 \times 10^{-6}\,(T_H - T_o)^{1.66}\, \frac{h_1}{\sqrt[5]{h_1^5 + (0.43\, r_o)^5}}\, \frac{h_2}{\sqrt[2.38]{h_2^{2.38} + 929^{2.38}}} \quad (11)$$
$$(r_o - 240)\left(\frac{0.72\, d_2}{\sqrt[1.2]{d_2^{1.2} + 756^{1.2}}} + 0.33\right)$$

$$S_{(z)} = 2.45 \times 10^{-6}\,(T_H - T_o)^{1.8}\, \frac{h_1}{\sqrt[4]{h_1^4 + (0.24\, r_o)^4}}\, \frac{h_2}{\sqrt[3.4]{h_2^{3.4} + 1163^{3.4}}} \quad (12)$$
$$(r_o - 201)\left(\frac{0.6\, d_2}{\sqrt[1.5]{d_2^{1.5} + 412^{1.5}}} + 0.41\right)$$

4.7. Validation du modèle compact proposé

Pour valider le modèle proposé, un ensemble de 30 capteurs est généré avec des combinaisons aléatoires des paramètres clés dans un espace de conception défini par les contraintes technologiques et économiques. Les valeurs des sensibilités issues des simulations FEM et des modèles compacts analytiques/numériques sont comparées dans les Figures 19(a) et (b) pour une accélération dans le plan et hors plan respectivement.

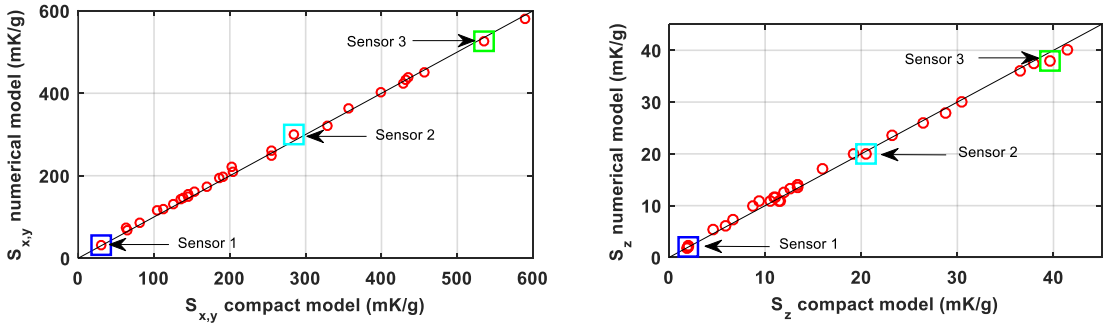

(a) *(b)*

Figure 19. *Sensibilités extraites des simulations numériques en fonction des sensibilités calculées avec le modèle compact pour des capteurs avec différentes valeurs de h_1, h_2, r_o, d_2, T_H pour des accélérations (a) dans le plan et (b) hors plan.*

Conclusion

Ce travail de thèse a principalement porté sur l'amélioration de la sensibilité d'un accéléromètre convectif CMOS en modifiant et optimisant les éléments suspendus du capteur afin de réduire les pertes thermiques par conduction. La comparaison entre l'accéléromètre de la littérature (Mailly, Nguyen et al. 2014) et celui proposé montre une augmentation de la sensibilité maximale d'un facteur 4 dans le plan et 5 hors-plan. L'accéléromètre proposé a été fabriqué. Une étude, basée sur une modélisation FEM, a également permis de développer des expressions analytiques de la sensibilité en fonction des paramètre clés de l'accéléromètre. Ceci a pour but de réduire le temps et la complexité des simulations pour prédire les performances de ce type d'accéléromètre.

REFERENCES

Boujamaa EM., Dumas N., Latorre L., Mailly F., Nouet P., « An innovative, offset immune, conditioning and read-out circuitry for resistive MEMS sensors », *Joint IEEE North-East Workshop on Circuits and Systems and TAISA Conference*, 2009.

Mailly F., Nguyen H.B., Latorre L., Nouet P., « CMOS implementation of a 3-axis thermal convective accelerometer», IEEE Sensors, 2014, p. 1471-1474.

Nguyen HB., Conception et réalisation d'un accéléromètre convectif 3-axes en technologie CMOS, Thèse de doctorat, Montpellier 2, 2013.

Nguyen HB., Mailly F., Latorre L., Nouet P., « A new monolithic 3-axis thermal convective accelerometer: principle, design, fabrication and characterization », *Microsystem Technologies*, vol. 21, n° 9, 2015, p. 1867-1877.

List of publications

JOURNALS

- Abdellatif S., Mezghani B., Mailly F., and Nouet P., « Analytical-Numerical Analysis for Compact Sensitivity Models of a CMOS MEMS Triaxial Convective Accelerometer », *IEEE Sensors Journal*, vol. 22, n°2, Jan. 2022, pp. 1199-1208, doi: 10.1109/JSEN.2021.3132425. **(Q1 & IF= 3.076).**
- Abdellatif S., Mezghani B., Mailly F., and Nouet P., « Enhanced 3-axis Sensitivity of a CMOS MEMS Convective Accelerometer Using a New Power Efficient Heater Structure », *Microsystem Technologies Journal*, Jan. 2022, doi: 10.1007/s00542-022-05254-3. **(Q2 & IF= 1.737).**

CONFERENCES

- Abdellatif S., Mezghani B., Mailly F., and Nouet P., « New High Efficiency Heater Design for a 3-axis CMOS MEMS Convective Accelerometer », *22nd IEEE DTIP 2020,* June 2020, Virtual, Paris, France
- Abdellatif S., Mezghani B., Mailly F., and Nouet P., « Optimal Detector Position and Structure for a New 3-axis CMOS Thermal Microaccelerometer », *17th IEEE SSD 2020,* Jul 2020, Virtual, Monastir, Tunisia.
- Abdellatif S., Mezghani B., Mailly F., and Nouet P., « Mechanical Solution for Out-of-Plane Sensitivity Enhancement of CMOS MEMS Convective Accelerometers », *24th IEEE ICECS 2018,* Dec 2018, Bordeaux, France.

Development and performance optimization of a 3-axis CMOS micromachined convective accelerometer

Abstract: This thesis deals with performance enhancement of triaxial convective microaccelerometer in terms of sensitivity, especially the out-of-plane one, and efficiency, (i.e., ratio of sensitivity to power). For this purpose, two solutions are investigated through numerical analysis using a validated FEM model. The solution which fully meets 0.35µm CMOS technology and FSBM post-process restrictions is chosen to design and fabricate a novel 3-axis convective accelerometer. Numerical simulations are used to demonstrate the superiority of the new accelerometer's performance compared to a State-of-the-Art sensor. Maximum in-plane and out-of-plane sensitivities are, respectively, 246 mK/g and 19 mK/g. Further, compact analytical models are established to predict in-plane and out-of-plane sensitivity levels of the newly developed microaccelerometer.

Keywords: Convective accelerometer, numerical analysis, MEMS, CMOS, compact analytical model

Développement et optimization des performances d'un accéléromètre convective triaxial CMOS micro-usiné

Résumé : Cette thèse porte sur l'amélioration des performances d'un microaccéléromètre convectif triaxial en termes de sensibilité, en particulier hors-plan, et d'efficacité, (i.e., rapport entre la sensibilité et l'énergie). Dans ce but, deux solutions sont étudiées par analyse numérique en utilisant un modèle FEM validé. La solution qui répond aux restrictions de la technologie CMOS 0,35µm et le post-traitement FSBM est choisie pour concevoir et fabriquer un nouvel accéléromètre convectif à 3 axes. Des simulations numériques sont utilisées pour démontrer la supériorité des performances du nouvel accéléromètre par rapport à un capteur de l'Etat de l'Art. Les sensibilités dans le plan et hors-plan maximales sont, respectivement, 246mK/g et 19mK/g. De plus, des modèles compacts analytiques sont établis pour prédire les niveaux de sensibilité dans le plan et hors-plan de microaccéléromètre nouvellement développé.

Mots clés : Accéléromètre convectif, analyse numérique, MEMS, CMOS, modèle analytique compact.